Development and characterisation of a carbon fibre reinforced MAX phase composite material

by
Jan Heimriks Nel

Thesis presented in partial fulfilment of the requirements for the degree of Master of Engineering (Mechanical) in the Faculty of Engineering at Stellenbosch University

Supervisor: Prof. D.C. Blaine
Co-supervisor: Prof. I. Sigalas

December 2017

Declaration

By submitting this thesis electronically, I declare that the entirety of the work contained therein is my own, original work, that I am the sole author thereof (save to the extent explicitly otherwise stated), that reproduction and publication thereof by Stellenbosch University will not infringe any third party rights and that I have not previously in its entirety or in part submitted it for obtaining any qualification.

Date: December 2017

Abstract

A carbon fibre reinforced MAX phase ceramic matrix composite (CMC) was produced in prepreg form and sintered using spark plasma sintering (SPS). MAX phase ceramics is a group of ternary ceramics exhibiting a combination of advantageous properties of both metals and ceramics.

The CMC prepreg was designed with a carbon fibre weave acting as reinforcement and a MAX phase (Ti_2AlC) acting as the matrix. Polymethyl methacrylate (PMMA) was used to coat the fibres and Ti_2AlC powder combination to achieve a flexible and robust prepreg.

Ti_2AlC powder was prepared by attrition milling in a liquid medium. The particle size distribution was measured using dynamic light scattering (DLS) and scanning electron microscopy (SEM). The mean particle size was reduced from 16 μm to 275 nm, allowing infiltration of the powder into a fibre weave. The effect of the attrition milling on the elemental composition of the powder was evaluated using energy dispersive spectroscopy (EDS) and powder X-ray diffraction (PXRD).

Electrophoretic deposition (EPD), vacuum infiltration, and pressure infiltration were evaluated for ceramic infiltration into a carbon fibre weave. The ceramic infiltration was investigated by examining polished cross-sections using optical microscopy.

Prepreg layers were combined and thermal debinding was performed at 400 °C to remove the PMMA coating. The CMC was sintered using SPS at 20 MPa and 1400 °C to create a 30 mm CMC disc. The sintered CMC had a density of 2.04 g/cm^3 and open porosity of 16 %. The microstructure of the CMC was evaluated using optical microscopy, SEM, and X-ray computed tomography (CT). The discs were fractured using the ball on three balls (B3B) test method to determine the strength and mechanical response. EDS and SEM analysis was employed to evaluate diffusion between carbon fibres and Ti_2AlC matrix. Aluminium diffused from the matrix into the fibres, resulting in the formation of Al_4C_3 in the carbon fibre and TiC in the matrix surrounding the fibre.

Uittreksel

'n Koolstof-versterkte MAX-fase keramieksamestelling was in 'prepreg' vorm gelewer en gesinter deur gebruik te maak van vonk plamsa-sintering (VPS). MAX-fase keramieke is n drieledige groep keramieke wat n kombinasie van bevorderlike eienskappe van beide metale en keramieke bevat.

Die keramieksamestelling is ontwerp met n koolstofveselweefstof wat as n versterker en n MAX-fase (Ti2AlC) wat as n matriks optree. 'n Bindstof (PMMA) was gebruik om die vesels en Ti2AlC-poeier kombinasie te bedek om n buigsame en sterk 'prepreg' te lewer.

Ti2AlC-poeier is deur middel van afslytingsmaling in n vloeibare medium voorberei. Die partikelgrootte is deur dinamiese straalstrooiing en skanderings-elektron-mikroskopie (SEM) gemeet. Die mediaan partikelgrootte is van 16 μmm na 275 nm verminder wat toelaat dat die poeier die weefstof infiltreer. Die uitwerking van die afslytingsmaling op die poeier se elementale samestelling is deur middel van energie-verstrooings-spektroskopie (EVS) en poeier X-straaldiffraksie bepaal.

Elektroforetiese neerslagvorming , vakuuminfiltrasie en drukinfiltrasie is gevalueer vir keramiek-infiltrasie in n koolstofweefstof. Die keramiekinfiltrasie is ook ondersoek deur n gepoleerde deursnit deur middel van optiese mikroskopie waar te neem.

'Prepreg'-lae is gekombineer en termiese ontbinding het teen 400 °C plaasgevind om die PMMA deklaag te verwyder. Die keramiek-samestelling is deur middel van VPS teen 20 MPa en 1400 °C gesinter om 30 mm keramiek-samestallingskywe te vorm. Die gesinterde keramiek-samestelling het n digtheid van 2.04 g/cm^3 en n oopporeusheid van 16 % gehad. Die mikrostruktuur van die keramiek-samestelling is deur optiese mikroskopie, SEM en X-straal-saamgestelde tomografie. Die skywe is deur middel van die bal op drie balle (B3B) toetsmetode gebreek om die sterkte en die meganiese vermo daarvan te toets. EVS en SEM-analise is ingespan om die diffusie tussen die koolstofvesels en die Ti_2AlC-matriks te evalueer. Aluminium het vanaf die matriks na die vesels gediffundeer en gelei tot die vorming van Al_4C_3 in die koolstofvesels en TiC in die matriks rondom die vesels.

Acknowledgements

I would like to thank a special group of people for their contribution towards the completion of this project:

My mother for carrying me all these years and for being the strongest woman I know.

My father for being my hero, an exceptional role model, and friend.

Arleen, Marina, Inge, and Paige for your unconditional love and support. With you, I will always have a home.

Professor Debby Blaine for her valuable insights and guidance.

Professor Iakovos Sigalas for directing the project.

Patrick Rockebrand, Phylis Makurunje, and Sharona Melchior for their help at Wits University.

The DST-NRF Centre of Excellence in Strong Materials (CoE-SM) for project funding.
The support of the DST-NRF Centre of Excellence in Strong Materials (CoE-SM) towards this research is hereby acknowledged. Opinions expressed and conclusions arrived at, are those of the author and are not necessarily to be attributed to the CoE-SM.

Contents

List of Figures

List of Tables

1 Introduction

The subject of this study is the development and characterisation of a carbon fibre-reinforced MAX phase composite. The section introduces the topic by describing the background to the project as well as the motivations for undertaking it. The objectives of the project are then outlined as well as the scope and limitations.

1.1 Background and Motivation

The availability of suitable materials becomes critical for high temperature applications, where materials need to retain their shape and strength at elevated temperatures (Leslie et al., 2015). Discovered in the 1960s, the group of ternary ceramics and nitrides, now referred to as the MAX phases, remained mostly unexplored until Barsoum and El-Raghy (1996) synthesised relatively phase-pure Ti_3SiC_2. The various properties of the MAX phases led to it being considered as a unique engineering material. Although MAX phases are ductile for ceramics, they are still brittle when compared to metals. Reinforcing a MAX phase to produce a ceramic matrix composite (CMC) could lead to a damage tolerant material.

CMCs are popular materials for use in structural aerospace applications as well as advanced friction systems (Krenkel and Berndt, 2005). Recent research efforts have been aimed at developing more efficient methods of fabricating these composites. Mature processing routes for CMCs include chemical vapour infiltration (CVI) and polymer impregnation/pyrolysis (PIP) (Naslain, 2004). These methods require long processing times and therefore remain inefficient. CMCs are popular materials for use in high temperature applications, where advanced metals are rendered useless (Leslie et al., 2015), (Volkmann et al., 2014), (Naslain, 2004). The most researched being carbon fibre reinforced SiC composites.

The aim of the project proposed herein is the development and subsequent characterisation of a CMC, consisting of a MAX phase matrix and a suitable reinforcement structure. The MAX phases are no ordinary ceramics. Metals are generally good electrical and thermal conductors, machinable, thermal shock resistant, and damage tolerant, whereas ceramics have high elastic moduli, high temperature strength, oxidation, and corrosion resistance. These MAX phases combine the properties of metals and ceramics.

The MAX phase that will be used for the composite is Ti_2AlC. It has been selected for this project due to the relative ease of fabrication. It has been fabricated and tested previously, on its own, and will be discussed in the literature study.

Previous work include the investigation of a Ti_2AlC/c-BN composite (Rampai et al., 2013). This focussed on using the Ti_2AlC as a binder phase for the abrasive cubic boron nitride (c-BN) for use in grinding and cutting tools. The proposed project differs in various aspects as fibre reinforced composite will be developed, instead of a particle reinforced composite. The particle reinforced composite is aimed at use in grinding and cutting tools while the proposed fibre reinforced composite is aimed at structural use in high temperature applications.

1.2 Objectives

The aim of this project is to develop a CMC prepreg, consisting of a MAX phase matrix and a suitable reinforcement, that can be handled, shaped, and sintered to deliver a sufficiently dense matrix. Prepreg is a term used to describe a pre-impregnated fibre composite. Generally this is a fibre preform impregnated with a resin that cures upon heating. In this project, prepreg refers to a carbon fibre preform infiltrated with MAX phase powder particles. This brings its own set of challenges and uncertainties to the project. One such uncertainty is whether a sufficient amount of powder can be infiltrated into the carbon fibre preform to result in a dense matrix when sintered. Therefore, the following are the objectives for the project. Firstly, design a CMC prepreg consisting of a powder MAX phase matrix and a suitable fibre reinforcement structure. Secondly, produce the CMC prepreg by infiltrating the MAX phase powder into the fibre reinforcement structure. Thirdly, use spark plasma sintering (SPS) to consolidate the CMC prepreg. Finally, evaluate the material and mechanical properties of the sintered CMC.

1.3 Scope and Limitations

This work is limited to the design, fabrication and characterisation of a novel CMC with a MAX phase material as matrix. The characterisation work is limited to the evaluation of the microstructure, elemental composition, and mechanical behaviour. This work does not include investigations into the refractory properties of the CMC. Evaluation of statistically significant strength properties is not included due to the expense associated with acquiring the MAX phase material. Mechanical tests are performed only to compare the strength and mechanical behaviour of the CMC to that of the monolithic MAX phase. Furthermore, the study is limited to the evaluation of a prepreg CMC design using SPS to consolidate individual laminates into a coherent CMC material.

2 Literature Study

A literature study was conducted throughout the duration of the project. The relevant concepts pertaining to the properties of MAX phases in general, ceramic matrix composites (CMCs), and a general overview of spark plasma sintering (SPS) are documented in this section.

2.1 MAX Phases

After the synthesis of phase-pure Ti_3SiC_2, Barsoum and El-Raghy (1996) discovered that the material has high electrical and thermal conductivity, is resistant to thermal shock and oxidation, and is readily machinable. The material appears to exhibit a remarkable combination of metallic and ceramic properties. They later discovered that Ti_3SiC_2 is part of a larger group of materials, within the layered ternary ceramics group, with the same fundamental structure that gives them similar properties. This led to the term 'MAX' phase being coined by Barsoum and El-Raghy (2001). More than 60 MAX phases, with the common structure $M_{n+1}AX_n$, have been discovered. M represents an early transition metal, A represents a group-A element, mostly IIIA and IVA, and X is either C or N (Barsoum and Radovic, 2011). For n = 1 (M_2AX), n = 2 (M_3AX_2), and n = 3 (M_4AX_3) the phases are referred to as the 211, 312, and 413 phases, respectively. The crystal structures for n = 1,2, and 3 are shown in Figure 1. Ti_3SiC_2 is by far the most researched MAX phase (Radovic et al., 2003), (Zhen et al., 2005a), (Radovic et al., 2001), (Wan et al., 2008), (Zhen et al., 2005b), (Radovic et al., 2002), (Barsoum and El-Raghy, 1996), (Farber et al., 1999), (Kooi et al., 2003), (Tang et al., 2002), (Panigrahi et al., 2009), (Li, 2003), (Zhang et al., 2002), (Sun et al., 2002), (Zhang et al., 2001), (Gauthier et al., 2006), (Hashimoto et al., 2002), (Zhang et al., 2003), (Morgiel et al., 1996), (Sato et al., 2014).

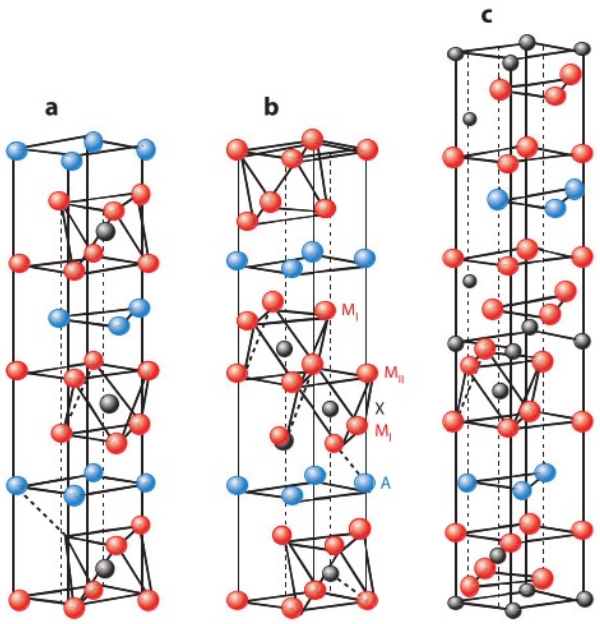

Figure 1: MAX phase structure for (a) n=1, (b) n=2, and (c) n=3 respectively (Barsoum and Radovic, 2011).

2.1.1 Synthesis of the MAX Phases

There are numerous ways of synthesising bulk MAX phases from elemental powders. These methods include SPS (Sun et al., 2010), hot pressing (HP)(Zhu et al., 2008), and thermal explosion (Khoptiar and Gotman, 2002). High energy milling is used to make the synthesis more effective (Zhu et al., 2008). The rest of this section focuses on the synthesis of the Ti_2AlC MAX phase, as it is the MAX phase that has been chosen for this study.

Sun et al. (2010) synthesised fully dense and nearly single-phase Ti_2AlC using an off-stoichiometric molar powder mixture of (2)Ti:(1.05)Al:(0.95)C. The off-stoichiometric composition delivered optimal results most likely due to the volatilisation of Al at the high temperatures. The mixed powder was sintered into a 50 mm diameter disk, at 1250 ℃ for 20 min, using SPS.

Wang et al. (2007) synthesised bulk Ti_2AlC, containing small amounts of Ti_3AlC_2, using HP at 1400 ℃ and 30 MPa for 1 hour. TiC, Al, T, and activated carbon powder was used for the synthesis. The resulting material had a density of 4.1 g/cm^3, fracture toughness of 7 MPa.m$^{1/2}$, and flexural strength of 385 MPa at room temperature.

Zhu et al. (2008) mechanically alloyed Ti, Al, and C powder by using high energy milling. This resulted in the formation of $TiAl_3$ and TiC. HP was used at 1200 °C and 15 MPa for 1 hour to form pure bulk Ti_2AlC. The MAX phase could be synthesised at lower temperature and pressure, when compared to the results of Wang et al. (2007), due to the high energy milling process.

2.1.2 Elastic Properties

MAX phases in general have high elastic constants, represented by Young's modulus (E) and bulk modulus (K). Experimentally obtained values of E range from 178 GPa for Zr_2SnC (El-Raghy et al., 2000) to 347 GPa for Ti_3GeC_2 (Radovic et al., 2006), while values of K range from 139 GPa for Cr_2AlC (Lofland et al., 2004) to 261 GPa for Ta_4AlC_3 (Manoun et al., 2006). This coupled with their relatively low densities mean that most have high specific stiffness values. To put this into perspective, the specific stiffness of Ti_3SiC_2 is roughly three times that of Ti. Poisson's ratios, at approximately 0.2, do not vary much among MAX phases (Barsoum and Radovic, 2011).

Determining E using the slope of the stress-strain curve results in an underestimation due to the nonlinear elastic behaviour of the MAX phases. The effect is that elastic constants are determined using acoustic methods and this in turn means that determination of elastic constants at elevated temperatures remains difficult. Radovic et al. (2006) investigated the effects of temperature on the elastic properties of certain MAX phases by using resonant ultrasound spectroscopy at low strains to determine the elastic constants. The results indicated that the elastic properties are not a strong function of temperature. At 1000°C Ti_3SiC_2, Ti_3AlC_2, and Ti_2AlC retained more than 85% of their room temperature elastic stiffness values (Radovic et al., 2006).

In contrast to most elastically stiff materials, the MAX phases exhibit nonlinear, hysteretic, elastic behaviour during cyclic loading (Barsoum et al., 2003). This behaviour can be largely explained by the formation, growth, and annihilation of incipient kink bands (IKBs) (Barsoum and Radovic, 2011). IKBs are KBs that are not yet plastically deformed and that shrink upon removal of the applied load. Barsoum et al. (2003) reported that polycrystalline Ti_3SiC_2 can be cyclically loaded at room temperature to stresses as large as 1 GPa and fully recover upon removal of the load. During this cyclic loading 25 % of the mechanical energy is dissipated by the material, thereby causing the hysteretic behaviour. This behaviour is a function of grain size. Smaller grains result in a stiffer solid, while larger grains lead to more energy being dissipated (Barsoum et al., 2003). Figure 2 shows the nonlinear, hysteretic, elastic behaviour for Ti_3SiC_2 cyclically loaded in

compression.

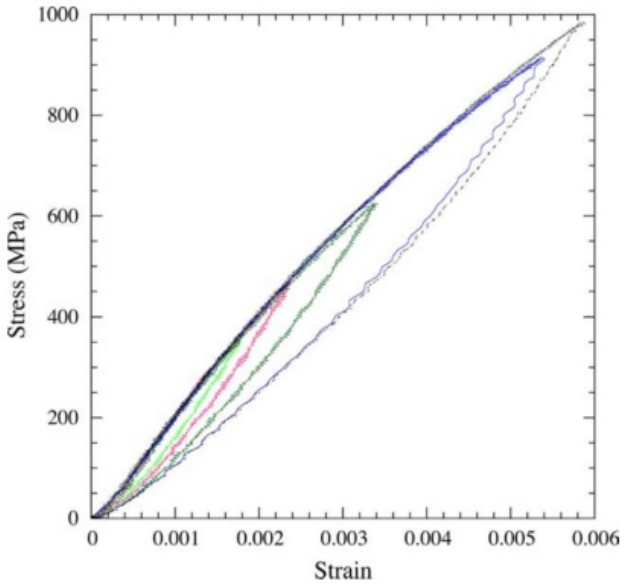

Figure 2: Loading-unloading stress-strain curve for Ti_3SiC_2 displaying the non-linear hysteretic elastic behaviour in MAX phases (Zhen et al., 2005b).

2.1.3 Mechanical Properties and Deformation

MAX phases deform by basal plane dislocations alone (Kooi et al., 2003), which by itself cannot yield more than the five slip systems required for ductility. Therefore the MAX phases cannot be characterised as strictly ductile or brittle, such as typical ceramics with zero independent slip systems. Barsoum and Radovic (2011) characterise their behaviour as pseudoductile when having highly oriented microstructures or being subjected to high temperatures. Otherwise their behaviour is of a brittle nature. These basal plane dislocations are mobile and multiply due to deformation (Farber et al., 1999). The effect is the formation of KBs within individual grains under applied loads. In addition to KB formation, the MAX phases have several energy absorbing mechanisms that act during deformation. Such as microcracking, delamination, crack deflection, grain push-out, grain pull-out, and buckling of individual grains (El-Raghy et al., 1997). Figure 3 shows the formation of KBs as well as delamination in a Ti_3SiC_2 sample.

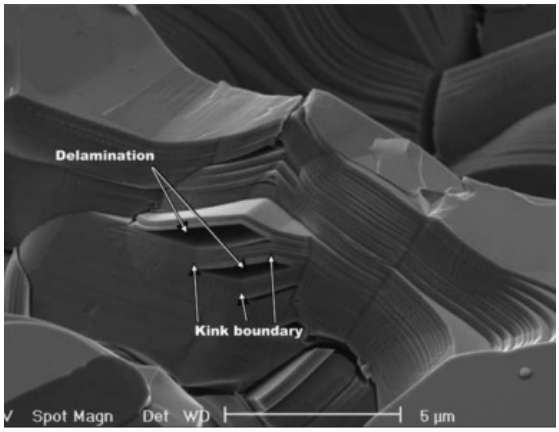

Figure 3: KB formation and delamination on the fracture surface of a porous Ti_3SiC_2 sample (Sun et al., 2005).

The strength of the MAX phases is a function of grain size. Smaller grains result in stronger solids in all cases (El-raghy et al., 1999). The MAX phases are weakest in tension and strongest in compression. They are approximately twice as strong in compression as in flexure (Barsoum and Radovic, 2011). Due to the dependence on grain size, it is difficult to pinpoint the critical stress boundaries for the MAX phases. Contrary to the critical stresses, fracture toughness increases with grain size (El-raghy et al., 1999).

All MAX phases undergo a brittle-to-plastic transition (BPT) at varying temperatures (Barsoum and Radovic, 2011). The transition temperature for Ti_3SiC_2 and Ti_3AlC_2 is in the 1100°C range. The fracture toughness remains nearly constant for temperatures up to the transition temperature, beyond this temperature the fracture toughness declines rapidly (Wan et al., 2008).

The creep behaviour of Ti_3SiC_2 is characterised by three stages. A short primary stage wherein the strain rate decreases rapidly, a secondary quasi-steady state, and a tertiary state (Zhen et al., 2005a). The strain rate is dictated by the competing rates of internal stress accumulation and relaxation (Radovic et al., 2001). The internal stresses can be better dissipated by delamination and the formation of KBs at lower strain rates and/or higher temperatures (Radovic et al., 2003). The dominant creep mechanism during primary and secondary stage is believed to be dislocation creep. Tertiary stage creep is initiated by the change of dominant mechanism from dislocation creep to the formation of cavities and microcracks (Zhen et al., 2005a).

The effect of thermal shock is dependant on grain size, as with other properties of the MAX phases , and unlike other ceramics, the MAX phases do not shatter

when quenched from high temperatures (El-Raghy et al., 1999). Fine-grained Ti_3SiC_2 shows a decrease in flexural strength when quenched from above 600°C, while coarse-grained Ti_3SiC_2 shows a slight increase in strength when quenched from 1400°C (Barsoum and Radovic, 2011).

2.1.4 Damage Tolerance

MAX phases, with Vickers hardness values in the range of 2-8 GPa (204-816 HV), are softer than most structural ceramics and harder than most metals (Barsoum and Radovic, 2011). The hardness value increases with a decreasing load until the load is no longer sufficient to leave any trace of indentations (El-Raghy et al., 1997). At this load the hardness is no longer measurable. These observations were only understood when work on nanoindentations made the reversible nature of the IKBs clear (Barsoum, 2004). In typical ceramics, Vickers indentations result in crack formation and propagation at the indentation corners. MAX phases contain the extent of damage by means of plastic deformation in the form of delaminations, kinking of grains, grain pushouts, and grain pullouts (El-Raghy et al., 1997). The result is that the MAX phases are extremely damage tolerant. Figure 4 shows a Ti_2AlC block with multiple dents on the surface. These dents were caused by hitting the block with a steel hammer, demonstrating the damage tolerance of the MAX phases.

Figure 4: Surface of a Ti_2AlC block hit with a steel hammer multiple times, demonstrating the damage tolerant behaviour typical of MAX phase materials (Barsoum and Radovic, 2011).

2.2 Ceramic Matrix Composites

Fibre reinforced ceramic composites, herein referred to as CMCs, are applicable in a wide range of applications due to their increased fracture toughness compared to their monolithic counterparts. The fracture toughness property of CMCs stems from the ability of the fibre/matrix interface to arrest and deflect cracks formed

in the brittle matrix, thereby preventing abrupt failure of the composite (Naslain, 2004). CMCs can be used in space applications, advanced friction systems (Krenkel and Berndt, 2005), gas turbines, heat exchangers, and future nuclear reactors (Naslain, 2004). The most studied CMCs are combinations of C and SiC, namely C/SiC (fibre reinforcement/matrix), SiC/SiC, and C/C-SiC (Dong et al., 2012). Chemical vapour infiltration (CVI), polymer impregnation and pyrolysis (PIP), and liquid silicon infiltration (LSI) are among the more traditional methods of fabricating CMCs (Müller et al., 2004).

The properties of CMCs are highly dependant on matrix composition and the fibre/matrix interface. CMCs can be tailored for specific applications by modifying the matrix and/or the fibre/matrix interface (Dong et al., 2012).

2.2.1 Interphase

As mentioned the fibre/matrix interface is the key to ensuring improved fracture toughness of the CMCs. Therefore, the design of the interface is of critical importance in avoiding overly strong, or weak, bonding between fibres and matrix (Dong et al., 2012). In order to prevent crack propagation from the fibre to the matrix, or vice versa, often a suitable interphase between fibre and matrix is employed. Interphases can be formed in situ, as a result of interaction between matrix and fibre during fabrication, or it can be deposited on fibres before composite fabrication (Naslain, 1998). Interphases consisting of materials with layered structures prove to be the most promising for use in CMCs (Naslain, 1998), notably layered structure pyrocarbon and hexagonal boron nitride (h-BN) (Dong et al., 2012).

The perfect interphase should satisfy four basic functions (Naslain, 1998). Firstly, it should serve as a mechanical fuse to protect the fibres by deflecting cracks formed in the matrix by having a sufficiently weak fibre/matrix interface. Secondly, it should allow some degree of load transfer between fibre and matrix by having a sufficiently strong fibre/matrix interface. The requirements of the first two functions are contradictory, which is why the design of the fibre/matrix interface should be carefully considered to find a suitable compromise. The third function of the interphase is to act as a diffusion barrier to prevent diffusion of matrix constituents into fibres. The requirement for this function is that the interphase should be thermodynamically compatible with fibre and matrix. The fourth and final function of the interphase is to relax residual stresses caused by high temperatures during fabrication and use.

The different interphases used in CMCs can be divided into four types (Naslain, 1998). A type 1 interphase leads to a simple weak interface between fibre and

matrix. These are typically anisotropic pyrocarbon deposited by CVI. Type 2 interphases have a layered crystal structure parallel to the fibre surface. Turbostratic pyrocarbon and h-BN are commonly used as type 2 interphase. Type 3 interphases consist of multiple layers of dissimilar material. The interphase can be tailored in terms of the type, sequence, and thickness of individual layers. Additionally, the functions of individual layers can be decoupled. Thereby ensuring that the interphase fulfils all required functions while not being limited by a single material. Finally, type 4 interphase consists of a layer of porous material with the pores serving as a deflection network for cracks.

2.2.2 Processing Methods Overview

Despite the significant porosity present in CMCs made via the CVI route, these CMCs are a commercial success. This is because they can perform critical engineering tasks that other conventional materials cannot (Lange et al., 1991). The success of these materials show that CMCs do not have to be fully dense. Although this is true, a large portion of processing research in the field of CMCs is aimed at increasing the density of the matrix to produce a composite with higher strength and reliability.

The main processing techniques to create the interphase and the matrix of the CMCs can be divided into three main groups as follows:

1. a gas phase route (chemical vapour infiltration (CVI))
2. a liquid phase route which employs polymer impregnation/pyrolysis (PIP), reactive melt infiltration (RMI), or both
3. a powder processing route.

Gas phase route
Chemical vapour deposition (CVD) is the deposition of a solid onto a substrate by a chemical reaction involving a gaseous precursor. The substrate is heated to a moderate temperature, below the melting temperature of the deposit, to activate the chemical reaction (Naslain, 1992). CVI is an adaptation of the CVD technique wherein the solid is not only deposited on the external surface of the substrate but also within the pores of the substrate. This is achieved by using the same precursor and apparatus while adjusting the deposition parameters to favour infiltration (Naslain, 1992). CVI normally occurs in the temperature range 900-1100 °C and at low pressures.

CVI has the advantage that, due to its deposition parameters, problems usually associated with high-temperature and high-pressure processing are avoided. Using

this method, complex-shaped products can be fabricated as near-net-shaped parts. When performed isothermally the surface pores have the tendency to close up first. This problem can be solved by applying an inverse temperature gradient to the preform, by applying a pressure gradient to the preform, or by employing periodic surface machining and multiple impregnation cycles (Naslain, 2004). Using CVI can take weeks of infiltration time which is why it is regarded as a very expensive method (Besmann et al., 1995). There are numerous variations on CVI that aim to reduce the disadvantages of the processing route. All of the variations result in significant porosity, usually 10-15%, which causes the CMC to have a low thermal conductivity and reduced mechanical strength (Naslain, 2004).

Liquid phase route

The liquid phase route can include PIP, RMI, or a combination of the two. PIP involves the impregnation of a liquid precursor into a preform. The precursor used depends on the ceramic required for the CMC. The precursor is then cured and subsequently pyrolysed at a temperature between 1000 and 1200 °C. The pyrolysis leads to a pure ceramic or a combination of ceramics, depending on the atmosphere. Significant shrinkage occurs during pyrolysis and the gaseous species formed create porosity in the composite (Naslain, 2004). Therefore several PIP cycles are required to achieve a dense composite.

RMI involves the infiltration of a liquid, usually silicon with a melting point of about 1400 °C, into a porous C/C composite. The porous composite can be prepared by CVI or PIP. The liquid is infiltrated into the pore network by capillary forces. The resulting reaction for liquid silicon is given by (Naslain, 2004):

$$\mathrm{C(s)} + \mathrm{Si(l)} \longrightarrow \mathrm{SiC(s)} \tag{1}$$

In addition to high processing temperatures, liquid silicon is corrosive with respect to typical interphases such as h-BN and also to the fibres. CMCs created by infiltration of silicon can contain pure silicon, limiting its refractory properties (Naslain, 2004). RMI results in a CMC with almost no open porosity and is a fast densification technique when ignoring the preparation time of the porous composite used for the infiltration (Naslain, 2004).

Powder processing route

Similar to the liquid phase route, when employing a powder processing route to create a CMC, the matrix precursor is a stable liquid suspension of ceramic powder with a high solids-loading. This is referred to as a slurry. Binders are normally used in the slurry to temporarily bind the particles to the fibres. The reinforcement, either a fibre tow or a fibre preform, is impregnated with the slurry. The impregnated reinforcement can then be shaped and stacked according to preference and sintered at high pressure and temperature (Lange et al., 1991). The

pressure and temperature required during sintering depends on the matrix material. The sintering process can cause damage to the fibre reinforcement, due to high processing parameters, leading to a weak composite. This problem can be addressed to some extent by using sintering additives and nanosized powder (Naslain, 2004). A composite made successfully with this method has very low residual porosity and high mechanical and thermal properties (Naslain, 2004).

2.2.3 Composites by Powder Processing Route

The methods used for fabricating CMCs are identified and broadly summarised in section 2.2.2. This section goes into more detail regarding the powder processing route as this is more applicable to the current study. Not mentioned in section 2.2.2 is the dry powder processing route. Using a liquid carrier for infiltrating a fibre preform with powder particles has numerous advantages over using a dry powder method. Therefore this section will focus on the former.

For successful infiltration the liquid carrier should adhere to the following:

- the liquid should enable spreading of the fibre weave,
- it should be possible to achieve a kinetically stable suspension/slurry,
- it should be possible to adjust the apparent viscosity of the slurry to enable fibre bundle infiltration,
- the liquid carrier should not contaminate the powder and should be eliminated completely without the need of excessive temperatures (Even et al., 2008).

If this is not the case, the powder particles have to be smaller than inter-fibre distances dictated by the fibre architecture. Tang et al. (1997) studied the impact of powder particle size on infiltration and proposed a model relating fibre volume fractions and powder particle size. Tang et al. (1997) proposed the model as a square geometrical model by using an idealised fibre/matrix structure with no fibre agglomeration and no matrix-rich areas. The fibre volume fraction is expressed as:

$$F = \frac{3d^2}{3d^2 + 2D^2} \tag{2}$$

and from this the slurry concentration can be expressed in terms of fibre volume fraction F, matrix density ρ, fibre diameter d, and particle diameter D as:

$$C = \frac{\pi\rho(1-F)}{2F((D/d)+1)^2 + \pi} \tag{3}$$

Even et al. (2008) employed a slurry infiltration process to create a carbon fibre reinforced titanium matrix composite. They achieved a fibre volume fraction of 12 vol % when using particles with average sizes of 25 μm and 10 μm diameter carbon fibres. Reduction of the particle sizes to 1-3 μm resulted in a fibre volume fraction of 35 vol %. Their results are not in accordance with the model proposed by Tang et al. (1997).

The process of sintering can be greatly affected in the presence of a second non-densifying phase or inclusion. In the case of many CMCs, the second phase will be the fibre reinforcement. De Jonghe et al. (1986) showed that volume fractions of 3 % SiC inclusions in a ZnO powder compact would significantly limit the densification of the compact and for volume fractions above 25 % SiC inclusions, practically no change in density of the compact is observed during pressureless sintering. They found that the densification rate decreases with an increase in inclusion volume fraction. De Jonghe et al. (1986) postulated that this is caused by a hydrostatic stress, generated by the inclusions, that opposes the compressive sintering stress. Lange et al. (1991) concluded that the mean hydrostatic stress does not have a significant effect on the densification of composite materials. This is because an inclusion network constrains composite shrinkage while not preventing powder shrinkage within the network. In other words, the volume of shrinking voids is conserved by opening voids in other regions.

The worst case scenario for composite densification is for a touching inclusion network. In this case the driving force for sintering, under pressureless conditions, is not sufficient to further consolidate the network (Lange et al., 1991).

2.2.4 Electrophoretic Deposition and its Application to Ceramic Matrix Composites

Electrophoretic deposition (EPD) can also be used in the fabrication of CMCs on its own or in combination with the methods briefly discussed in section 2.2.2. EPD is not discussed with the other methods as it is still considered a novel method in the fabrication of CMCs. The concepts on suspension stability discussed herein is also applicable to the method discussed in section 2.2.3.

EPD is a colloidal process wherein a DC electric field is applied to deposit suspended charged powder particles onto an oppositely charged conductive substrate. EPD should not be confused with electrolytic deposition as the two processes are fundamentally different. Therefore this review will focus only on EPD. EPD can be either anodic, where negatively charged particles are deposited onto the anode (positive electrode), or cathodic, where positively charged particles are deposited

onto the cathode (Besra and Liu, 2007). The process of EPD has numerous benefits including short deposition times, little substrate shape limitations, and it requires only simple apparatus. The main disadvantage of EPD, with respect to other colloidal processes, is that the use of water as a liquid medium will lead to the formation of hydrogen and oxygen at the electrodes on application of the voltage (Besra and Liu, 2007). This can negatively influence the quality of the deposition and should be avoided where possible. Therefore, this discussion is focused around solvent-based EPD.

The characteristics of EPD are influenced by numerous parameters that can be divided into two main groups: suspension parameters and process parameters. The different influential parameters will be discussed later on in this section. The first to correlate deposition yield with suspension and process parameters was Hamaker (1940). The Hamaker law can be expressed as follows:

$$w = \int_{t_1}^{t_2} \mu \, E \, A \, C \, dt \tag{4}$$

where w is the deposition yield, μ is the electrophoretic mobility of the dispersed particles, E is the electric field strength, A is the surface area of the deposition electrode, and C is the mass concentration of the dispersed particles.

The behaviour of the particles within a suspension/slurry is governed by interparticle forces. The main of these interparticle forces are: van der Waals attractive forces, electrostatic (double layer) repulsive forces, and steric repulsive forces (Besra and Liu, 2007). Ensuring that repulsive forces are larger than van der Waals forces is essential for a stable suspension. This is an important factor for most colloidal processes as these processes would not be effective for an agglomerated, unstable, and non-homogeneous system (Besra and Liu, 2007).

The properties of a suspension can be adjusted by manipulating interparticle forces and have a considerable effect on the quality and success of EPD. In classical Derjaguin-Landau-Verwey-Overbeek (DLVO) theory, steric forces were not considered. DLVO theory focusses only on van der Waals and electrostatic forces and interactions. Stabilisation of a suspension can be accomplished by manipulating the strengths of either of the interparticle repulsive forces. These methods are aptly named electrostatic and steric stabilisation and are schematically shown in Figure 5. Electrostatic stabilisation is achieved by increasing the electrostatic charge on the particles while steric stabilisation is achieved by the adsorption of hydrophilic macromolecules onto the surface of powder particles (Besra and Liu, 2007).

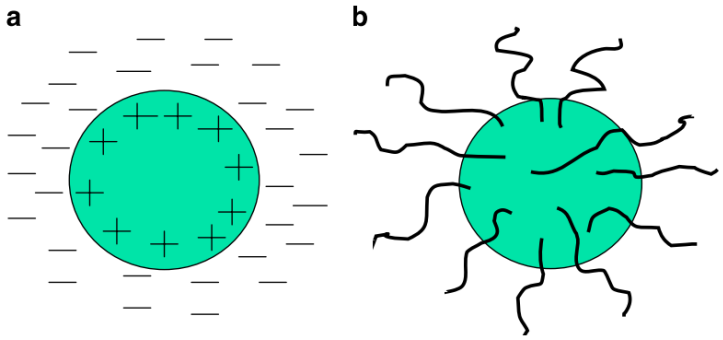

Figure 5: Schematic describing (a) electrostatic stabilisation and (b) steric stabilisation (Besra and Liu, 2007).

Parameters related to the suspension that influence the EPD process are: i. particle size, ii. the dielectric constant of the liquid, iii. the conductivity of the suspension, iv. the viscosity of the suspension, v. the ζ-potential, and vi. the stability of the suspension. The influence of these parameters are briefly explained.

i. Particle size
Smaller particles, around 1 μm, easily remain well-dispersed and stable in suspension due to Brownian motion. Larger particles tend to settle due to gravity, which can result in a vertical variation in the thickness of the deposition if the mobility of the particles is not sufficiently high (Besra and Liu, 2007). Additionally, Sato et al. (2001) showed that smaller particle sizes decrease crack formation in sintered films deposited by EPD.

ii. Dielectric constant of the liquid
Besra and Liu (2007) stated that a low dielectric constant, favouring low ionic concentration, is needed for successful EPD. Powers (1975) achieved successful EPD with liquids having relative dielectric constants between 12 and 25.

iii. Conductivity of the suspension
Ferrari and Moreno (1996) showed that EPD is only feasible for a narrow band of conductivity (150-170 μS/cm), which is expected to be unique for each system. Conductivity above the band of suitable conductivity restricts particle motion, while a low conductivity can results in an unstable system. The conductivity of a suspension increases with temperature and polyelectrolyte concentration (Ferrari and Moreno, 1996).

iv. Viscosity of the suspension
Normally in EPD, the solids loading is too low to make a significant difference in suspension viscosity. Therefore the viscosity of the suspension cannot be used as

assessment criteria for dispersion state. A low viscosity is desired for EPD (Besra and Liu, 2007).

v. ζ-potential
The ζ-potential determines electrostatic interactions, velocity, and direction of particle motion (Zarbov et al., 2004). Deposition rate and ζ-potential are directly related. The ζ-potential of particles in suspension can be used as a measure of stability when electrostatic stabilisation is used. The rule of thumb ζ-potential value is higher than 30 mV absolute for a stable system. The ζ-potential can be manipulated by the addition of charging agents such as acids, bases, and specifically adsorbed ions or polyelectrolytes (Zarbov et al., 2004).

vi. Stability of the suspension
Suspension stability is characterised by sedimentation rate and the ability to avoid particle agglomeration. Counterintuitively, a suspension can be too stable for EPD. This occurs when repulsive interactions between particles cannot be overcome by the electric field (Besra and Liu, 2007).

Parameters related to the process that influence the EPD process are: vii. deposition time, viii. applied voltage, ix. solids loading of the suspension, and x. the conductivity of the substrate. The influence of these parameters are briefly explained.

vii. Deposition time
It has been shown that the deposition rate during EPD, with a fixed electric field, decreases with deposition time (Basu et al., 2001). For some systems the deposition is linear during the initial stage of deposition, after which the deposition rate decreases and eventually plateaus (Wang et al., 2004). This is expected due to the thin layer of insulating ceramic forming on the deposition electrode.

viii. Applied voltage
Lower applied voltages are favoured for deposition quality while higher voltages result in higher deposition rates. Basu et al. (2001) showed that a lower applied field, in the range of 25-100 V/cm, results in the formation of a more uniform film during EPD of zirconia.

ix. Solids loading of the suspension
A higher solids loading leads to a higher deposition rate as expected. In EPD with multiple particle species in suspension, the solids loading changes the relative deposition rate of each different particle. At higher solids loading the deposition rate for different particle species is similar or equal, while lower solids loading increases the dependence of the deposition rate on the electrophoretic mobility of each respective particle (Vandeperre et al., 1997).

x. Conductivity of substrate
It has been established that low conductivity of deposition substrates leads to slow and low quality deposition (Peng and Liu, 2001).

2.3 Spark Plasma Sintering

Sintering is a process employed to create solid objects from particles in contact. It has been used for as long as 26,000 years for making ceramic objects. Before the theory of sintering emerged, an empirical trial and error methodology was used for the fabrication of sintered products. These empirical developments supported one another. The sintering of tungsten for lamp filaments arose due to developments made in sintering platinum. This in turn required developments in the field of sintered cemented carbide for the fabrication of dies to draw tungsten lamp filaments. The cemented carbide dies required artificial diamond composites for finishing operations. The fabrication of artificial diamonds requires high pressure structures relying on developments in the field of sintered carbide. Finally, the machinery used in these applications required low friction porous bearings (German, 2013).

Pressure can be applied to a powder compact to increase the driving force for densification while having no effect on grain growth. This can, however, be used as an effective tool when grain growth is not desirable, as the increase in driving force allows for the reduction in sintering temperature and sintering time to limit grain growth (Kang, 2005).

The application of pressure can be unidirectional or isostatic. These distinct processes are termed hot pressing (HP) and hot isostatic pressing (HIP), respectively. The HP configuration consists of a heated die, usually graphite, being pressurised by a hydraulic ram. In HIP the powder compact is encapsulated in a flexible container and placed in a pressurised chamber. Another method that makes use of unidirectional pressure is spark plasma sintering (SPS). SPS, sometimes called pulse discharge sintering (PDS) or field activated sintering techniques (FAST), is actually a misnomer as there is no spark or plasma present during the process (Andersson and Hulbert, 2009). Regardless, the process will be referred to as SPS as this is the acronym commonly used in the field. A pulsed direct current and a mechanical load are applied simultaneously to the compact in a controlled atmosphere. The process is regulated by controlling the current, load, and the cooling of the die enclosing the powder. The powder compact and the die are both heated by Joule heating caused by the direct current. The die then serves as a local furnace while the powder is heated internally. Figure 6 shows the configuration of the process. SPS uses pressure to aid the sintering procedure, as mentioned before.

SPS can achieve very high heating rates and therefore the process temperature and time is lower than for HP or HIP. Figure 6 shows a schematic representation of the SPS process.

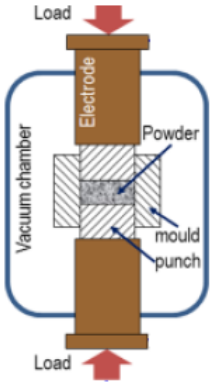

Figure 6: Configuration of the SPS process (Sun et al., 2010).

To illustrate the effect of an externally applied unidirectional pressure, the effective pressure for initial stage sintering, P_i, and for final stage sintering, P_f, is expressed in equation 5 and equation 6, respectively. The effective pressure for initial stage sintering is expressed as (Coble, 1970):

$$P_i \approx \frac{4a^2}{\pi\, x^2}\, P_{applied} + \frac{\gamma_s}{r} \tag{5}$$

where a is the particle radius, x the neck radius, and r is the radius of curvature. The specific surface energy, γ_s, is the driving force for densification where no external pressure is applied. The effective pressure for final stage sintering is expressed as (Coble, 1970):

$$P_f \approx \frac{P_{applied}}{\rho} + \frac{2\gamma_s}{r} \tag{6}$$

where ρ is the relative density of the compact. The two terms in the equations express the contribution of an externally applied pressure, $P_{applied}$, and the specific surface energy, γ_s, respectively. Equation 5 and equation 6 show that the contribution of the externally applied pressure is the dominating driving force for densification in the initial stage of sintering and a large part of the final stage of sintering. At the very end of densification, the driving force is dominated by the specific surface energy term as the relative density approaches 1. Additionally, during the initial application of pressure, brittle particles are fractured and particle rearrangement take place by slippage and restacking. This aids densification along with viscous flow of particles (Atkinson and Davies, 2000).

3 Composite Design

The importance of a properly designed ceramic matrix composite (CMC) cannot be overstated. There are various factors to consider during the design of a CMC, depending mainly on the intended use. For example, CMCs that operate in an oxidising environment, at elevated temperatures, with cyclic stress loading, are designed with the emphasis on refractory properties, oxidation resistance, and fatigue resistance. This design focuses on a novel MAX phase composite. For the specific MAX phase CMC design in this project, the MAX phase (Ti_2AlC) is set as the matrix phase with carbon fibre as the reinforcing phase. An interphase material, between matrix and reinforcing phases, is also considered. Throughout this section, the implications of design decisions will be discussed as well as the suitable uses and environments for the CMC.

3.1 Reinforcing Phase Design

The use of monolithic ceramics instead of CMCs may seem tempting at first glance. After all, monolithic ceramics can have higher stiffness and ultimate strengths than CMCs (Hyde, 1990). However, such an approach can be hazardous. The designer should be aware of the variability in monolithic ceramics as well as their susceptibility to processing flaws and in-service damage. Large safety factors will have to be included in the design of components due to small critical flaw sizes and the difficulty in performing non-destructive tests for ceramic materials (Hyde, 1990).

Various types of reinforcing materials are regularly used in CMCs. They can be categorised into two main groups, which can be further broken down (Callister and Rethwisch, 2011):

- Particle reinforcement
  - Large-particle
  - Dispersion strengthened
- Fibre reinforcement
  - Continuous fibres
  - Discontinuous fibres
    - Aligned
    - Randomly oriented

In large-particle reinforced composites, the particles restrain movement of the matrix phase around the particles. The load is shared by the matrix and reinforcing phase. Dispersion strengthened composites are obtained by the uniform dispersion of fine particles (10-100 nm) made of a hard inert material. Much like precipitation hardening, the matrix bears the majority of the load while the dispersed particles disrupt dislocations (Callister and Rethwisch, 2011).

A critical fibre length is needed for the strengthening and stiffening of the composite. This critical length depends on the fibre diameter, fibre strength, and the bond strength between fibre and matrix. The effects of the fibre reinforcement improves as the fibre length increases. Fibres are generally classified as continuous when the fibre length is more than 15 times that of the critical fibre length (Callister and Rethwisch, 2011). Continuous fibres are aligned, leading to orthotropic material properties.

The composite designed herein will make use of continuous fibre reinforcement as the focus is on obtaining a composite with high strength and fracture toughness. Unidirectional fibre composites are strong in the fibre direction, however, the strength decreases as the angle between stress and fibre direction increases. A multiaxial stress state is far more likely in a real world situation than the uniaxial loading that would favour the use of a unidirectionally reinforced component. A prime example of the multiaxial stresses routinely experienced by CMCs is the stress experienced during a thermal shock (Danzer et al., 2007). Therefore a $0°/90°$ woven fibre architecture has been chosen for the proposed composite as this is a suited and readily available configuration. Table 1 compares the Young's modulus and flexural strength of a MAX phase, monolithic SiC, and a SiC CMC to illustrate the effect of continuous fibre reinforcement on the strength and stiffness of the CMC. The mechanical properties of the CMC is dependant on the volume fractions of the constituents as the rule of mixtures dictates the properties in a composite. It is important to note that the values shown for the carbon fibres are for a tensile load and not flexural, as the fibres on their own can only support a tensile load. As a composite is loaded in flexure, a fraction of fibres is loaded in tension and a fraction is loaded in compression within the matrix. That is the reason why the presence of the carbon fibres within the CMC reduces the overall stiffness and strength of the monolithic ceramic even with the high stiffness and strength of the fibres in tension. The presence of the fibres does, however, increase the damage tolerant of the CMC compared to the monolithic ceramic.

Table 1: Comparison of mechanical properties of the Ti_2AlC MAX phase, a monolithic SiC ceramic, and a carbon fibre reinforced SiC CMC.

	ρ [g/cm^3]	E [GPa]	σ [MPa]	References
Ti2AlC	4.1	277	275	(Barsoum and Radovic, 2011)
SiC (monolithic)	3.16	415	359	(Munro, 1997)
C fibre (PAN)	1.76	231 (tensile)	3750 (tensile)	(MInus and Kumar, 2005)
CMC (C/SiC)	1.95	55	130	(Krenkel and Berndt, 2005)

It is beneficial to have knowledge of the basic stress-strain behaviour of CMCs for design purposes as this gives insight into the achievable life cycle and reliability of components. Generally, fibre reinforcement have higher stiffness and strength than the matrix and lower ultimate strains when a ductile material, such as a metal or a polymer, is used (Callister and Rethwisch, 2011). In the case of CMCs, where the matrix is a brittle ceramic, this is not always the case. Where brittle ceramics are used as matrix, the matrix can have higher stiffness and lower ultimate strains than the fibre reinforcement. The stress-strain behaviour of continuous fibre reinforced CMCs can be divided into three main regions as shown in Figure 7. The first is the linear elastic region. Cyclic loading in this stress region causes minimal damage due to fatigue (Hyde, 1990). The beginning of the second region usually corresponds with the ultimate strain of the matrix material. Therefore, this region marks the onset of microcracking in the matrix material 90° to the applied stress. Cyclic loading in this stress region causes significant fatigue and is therefore a measure of the damage tolerance of the composite (Hyde, 1990). At this point, the fibres are still able to deform elastically. The stiffness is lowered, shown by a lowered slope in Figure 7, due to the microcracking in the matrix. The third and final region begins at the CMC's ultimate strength, corresponding with the ultimate strain of the fibres (Callister and Rethwisch, 2011). Fibre pullout is initiated in this region and eventually leads to failure (Hyde, 1990). The failure is, however, not abrupt. After fibre failure, parts of the matrix is still intact. This is made possible by the fibre reinforcements that arrest and deflect cracks formed in the matrix.

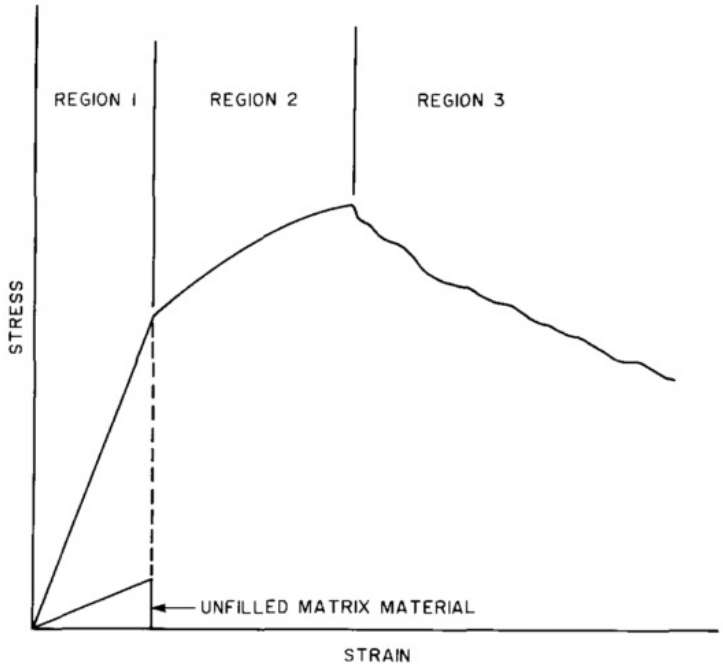

Figure 7: Stress-strain behaviour of CMCs (Hyde, 1990)

SiC and carbon are popular materials for use in continuous fibre reinforcement in CMCs. Carbon fibres are generally cheap and readily available in a wide variety. They have the highest specific stiffness and strength of all reinforcing fibres (Callister and Rethwisch, 2011). They do have their flaws, chief of which is susceptibility to oxidation from temperatures as low as 450 °C in oxidising atmosphere (Naslain, 2004). Additionally, carbon fibres have low coefficient of thermal expansion (CTE) in the longitudinal direction (1.6×10^{-6} K^{-1} to 2.1×10^{-6} K^{-1}), compared to the radial direction (5×10^{-6} K^{-1} to 10×10^{-6} K^{-1}) (Pradere and Sauder, 2008). This further exasperates the oxidation problem as this anisotropic CTE leads to microcracking in the matrix. This in turn exposes the fibres and leads to oxygen diffusion in oxidising atmospheres (Lamouroux and Camus, 1994). SiC fibres have good oxidation resistance when compared to carbon fibres. However, most SiC-based fibres are very expensive and contain impurities (Naslain, 2004).

Carbon fibres were chosen as reinforcement for the composite designed herein due to their stiffness, strength, availability, and cost effectiveness. The problem of microcracking due to anisotropic CTE of the fibres is not foreseen to be a major problem as the MAX phases are not as brittle as typical ceramics. This can limit the extent of oxidation if the fibres can be protected from the atmosphere by the

matrix material. For this composite to be suitable for use in oxidising atmospheres at elevated temperatures, little or no residual porosity must be present to limit oxygen exposure of the fibres.

3.2 Interphase Design

The functions and types of interphases are discussed in section 2.2.1. Material with a layered crystal structure or layered microstructure is best suited for use as an interphase. Deposition of the layered structure parallel to the fibre surface, with a strong bond between fibre and interphase and a weak bond between interphase and matrix results in an optimal interphase (Naslain, 1998). The strong bond between the fibre and the interphase is to achieve proper load transfer. If the bond is not sufficiently strong, fibre/matrix debonding at the fibre surface will lead to loss of load transfer and the fibres will be exposed to the atmosphere (Naslain, 2004). A strong bond between the fibre and the interphase leads to crack deflection and debonding in the interphase, thereby retaining load transfer and not directly exposing the fibres to the atmosphere. The resulting composite is tough, strong, fatigue resistant, and resistant to oxidising environments.

Pyrocarbon and h-BN are popular materials for use as interphase in CMCs due to their layered structure (Naslain, 2004). Due to the susceptibility of carbon to oxidation, h-BN will be used as interphase to attempt to mitigate the effect of oxidation on material performance. Additionally, a pyrocarbon interphase may lead to the formation of TiC crystallites due to the interaction between matrix and interphase during sintering (Even et al., 2008). These crystallites may induce notch effects on fibres. The matrix material is discussed in section 3.3. The inert h-BN interphase should improve oxidation resistance of the proposed CMC.

The different types of interphases are discussed in section 2.2.1. The use of a type 3 interphase, or multilayer interphase, will not be considered for the proposed CMC due to financial considerations. Multilayer interphases require multiple precursors and a specialised chemical vapour infiltration (CVI) process that will be too expensive in terms of time and financial resources. The most common, type 2 interphase, will be used in the proposed CMC, consisting of a layered crystal structure deposited parallel to the fibres. Most likely the interphase will resemble a combination of type 2 and type 4 interphase due to incomplete coverage of fibres with h-BN particles. The discontinuous particle coating will act as a deflection network for cracks while having layered crystal structure parallel to the fibre surface.

CVI, an expensive method briefly discussed in section 2.2.2, is the most commonly

used method for creating h-BN interphases (Naslain, 1998). This method will be avoided for the proposed CMC due to economic considerations. Another technique used is carbothermal synthesis (Das et al., 2009). This method involves dip coating fibres with a precursor, usually boric acid, followed by nitridation in an ammonia atmosphere. The coating thickness and structure can be controlled by adjusting nitridation time and temperature. Unfortunately, it is difficult to obtain a pure h-BN coating using this method. Amporphous-BN and small amounts of cubic-BN are almost always formed (Chen et al., 2003).

Electrophoretic deposition (EPD), discussed in section 2.2.4, is a process used for depositing charged particles in suspension onto substrates and fibres by applying an electric field. EPD is a novel and inexpensive method to coat fibres for use in CMCs and will therefore be used in this study. Aqueous EPD will be avoided due to the electrolysis of water at low voltages. A binder will be used to bind particles and fibres for the handling and analysis of the fibre preforms. A discontinuous powder coating will serve as a deflection network for cracks along the fibre. The deposited particles will lead to both interfaces, matrix/interphase and interphase/fibre, being weak. The discontinuous nature of the coating will ensure that proper load transfer is still possible.

3.3 Matrix Design

The matrix phase makes up the bulk of the CMC. In short, its functions are to protect fibres from damage from the environment and to transfer load to the fibres.

As this project aims to create a CMC with a MAX phase as matrix material, the matrix material will be chosen from the more than 60 discovered MAX phases. The choice was limited to MAX phases that are frequently researched, readily available, and affordable. Ti_3SiC_2 is by far the most researched MAX phase with more than 845 papers being published on Ti_3SiC_2 between 2001 and 2010 (Barsoum and Radovic, 2011). Ti_2AlC is suitable for use in temperatures above 100°C, has high specific stiffness, and oxidation resistance. Furthermore, it is readily available and affordable in comparison to other MAX phase materials.

CVI is an expensive method, as mentioned before, that results in significant porosity in the matrix. This porosity limits the thermal conductivity and mechanical properties of the composite (Naslain, 2004). Therefore CVI will not be considered for the matrix processing of the composite designed herein. Liquid phase processing is also not an option as MAX phases do not melt; they decompose at high temperatures.

Powder processing methods that can be used for creating the matrix are vacuum infiltration, EPD, and pressure infiltration. A binder will be used to bind the prepreg for handling and analysis.

De Jonghe et al. (1986) showed that the densification rate during sintering decreases as the volume fraction of inclusions increase. The oriented inclusions, continuous fibres in this case, inhibit densification during sintering. Using powder processing route, pressure-assisted methods are generally required to achieve satisfactory densification. This means that consolidation of the green composite will have to by hot-pressing (HP) or spark plasma sintering (SPS). The sintering pressure should be limited to avoid extensive damage to the fibres.

3.4 Conceptual Design

The proposed CMC prepreg is designed with:

- Ti_2AlC as the matrix phase,
- h-BN powder as the interphase, and
- carbon fibre weave as the reinforcing phase.

Polymethyl methacrylate (PMMA) is used as binder to coat the prepreg sheet in order to handle and cut the prepreg. Figure 8a is a schematic illustration of the cross-section of the CMC prepreg. The warp and weft of the fibre weave can be seen along with a MAX phase powder matrix region and the PMMA binder surrounding the prepreg sheet. Figure 8b is a schematic representation of a cross-section of a portion of a carbon fibre bundle showing, the powder matrix between fibres, the interphase around individual fibres, and the carbon fibres.

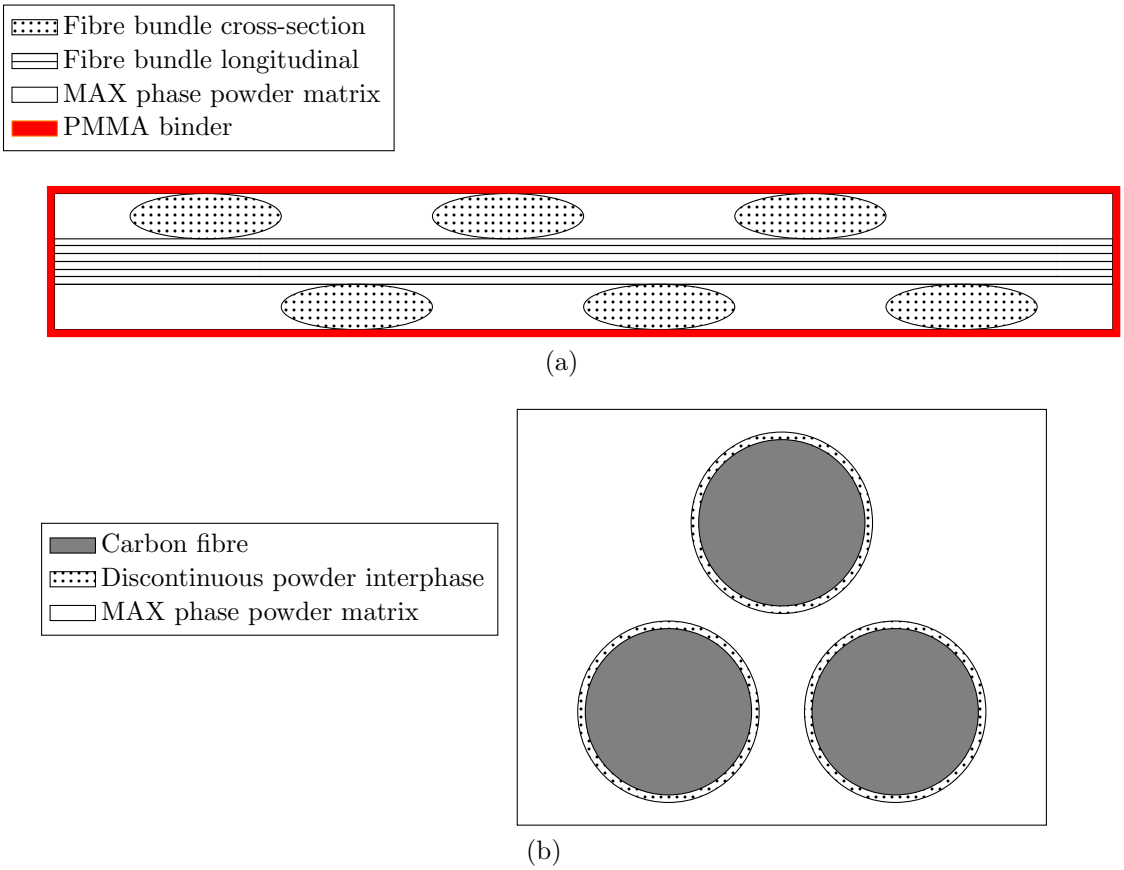

Figure 8: Schematic illustration of the conceptual design of the CMC prepreg with (a) showing a cross-sectional view of the prepreg and (b) showing a cross-sectional view of a portion within the fibre bundle in more detail.

4 Processing and Characterisation Methods

This section starts with a general overview of the raw materials and processing steps employed in the production of the MAX phase ceramic matrix composite (CMC). Thereafter, the methods used to characterise the product at different points during the process are presented.

4.1 Raw Materials

The raw materials selected for the production of the CMC are briefly discussed herein. The raw materials consist of Ti_2AlC powder (matrix phase), continuous carbon fibre weave (reinforcing phase), h-BN powder (interphase), polymethyl methacrylate (PMMA) (binder), and two different dispersants used in the processing of the CMC. The different components of the CMC are discussed in section 3.4 and illustrated in Figure 8. The technical data sheets for the raw materials are given in Appendix A.

Ti_2AlC powder
Ti_2AlC powder (supplier: Carbon-Ukraine Ltd.) was evaluated as matrix material. The as-received powder specification indicated particle size $\leq$ 40 μm with 80-95 % Ti_2AlC content (Carbon-Ukraine, 2015).

Carbon fibres
Polyacrylonitrile based plain weave carbon fibres (supplier: AMT Composites) with a thousand fibres in each warp and weft fibre bundle were used for the reinforcing phase of the CMC. The carbon fibre weave specification indicated a dry weight of 93 $\pm$ 4 g/m^2. Each fibre bundle is approximately 1.5 mm wide with individual fibres having diameters of approximately 7 μm. The fibre bundles have a yarn number of 67 tex, meaning that each 1000 m of warp and weft weighs 67 g (Engineered Cramer Composites, 2015). Using this information, the density of the carbon fibres was calculated as 1.74 g/cm^3.

h-BN powder
h-BN powder (supplier: Sigma-Aldrich co.) was evaluated as potential interphase for the proposed CMC in this study. The as-received powder specification indicated particle sizes around 1 μm and a purity of 98 % (Sigma-Aldrich, 2015).

PMMA
PMMA (supplier: Alfa Aesar) is used as a binder to allow green samples to be cut and handled. PMMA can be completely eliminated by heating to 400 °C, as is shown by the thermogravimetric analysis of the polymer in Figure 9 (Even

et al., 2008). Note that the PMMA had completely decomposed by 5 hours, which relates to 350 °C.

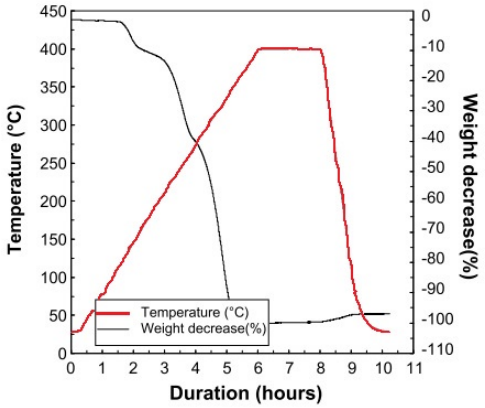

Figure 9: Thermogravimetric analysis of PMMA (Even et al., 2008).

Dispersant
Dolapix CE 64 (supplier: Zschimmer & Schwarz) is a carbonic acid based polyelectrolyte dispersant which has been used to disperse sub-micron particles including alumina and zirconia (Rao et al., 2007). The stabilisation mechanism used by Dolapix CE64 is a combination of electrostatic and steric stabilisation and is therefore termed electrosteric stabilisation (Zschimmer & Schwarz, 2016). Dolapix CE 64 was used as a dispersant during infiltration experiments.

Lubrizol 2155 is a succinimide dispersant frequently used in solvent and oil-based colourant systems (Lubrizol Advanced Materials Inc, 2015). Lubrizol 2155 was used as a dispersant during infiltration experiments.

4.2 Production Overview

The production of the CMC is discussed herein. The processes and experimental methodology used are described with respect to the production of the CMC only. Characterisation of the CMC is addressed in section 4.3. The processing can be divided into three processing phases, see Figure 10, each with their own distinct product.

In Phase 1, the MAX phase powder is milled in order to reduce the particle size of the as-received powder. Further details are presented in section 4.2.1. In Phase 2, the milled MAX phase powder is infiltrated into the carbon fibre weave mat in order to produce a CMC prepreg. Various infiltration methods were evaluated, as

discussed in section 4.2.2. In Phase 3, the prereg layers were sintered using spark plasma sintering (SPS). Thermal debinding of the prepreg followed by sintering is discussed in section 4.2.3.

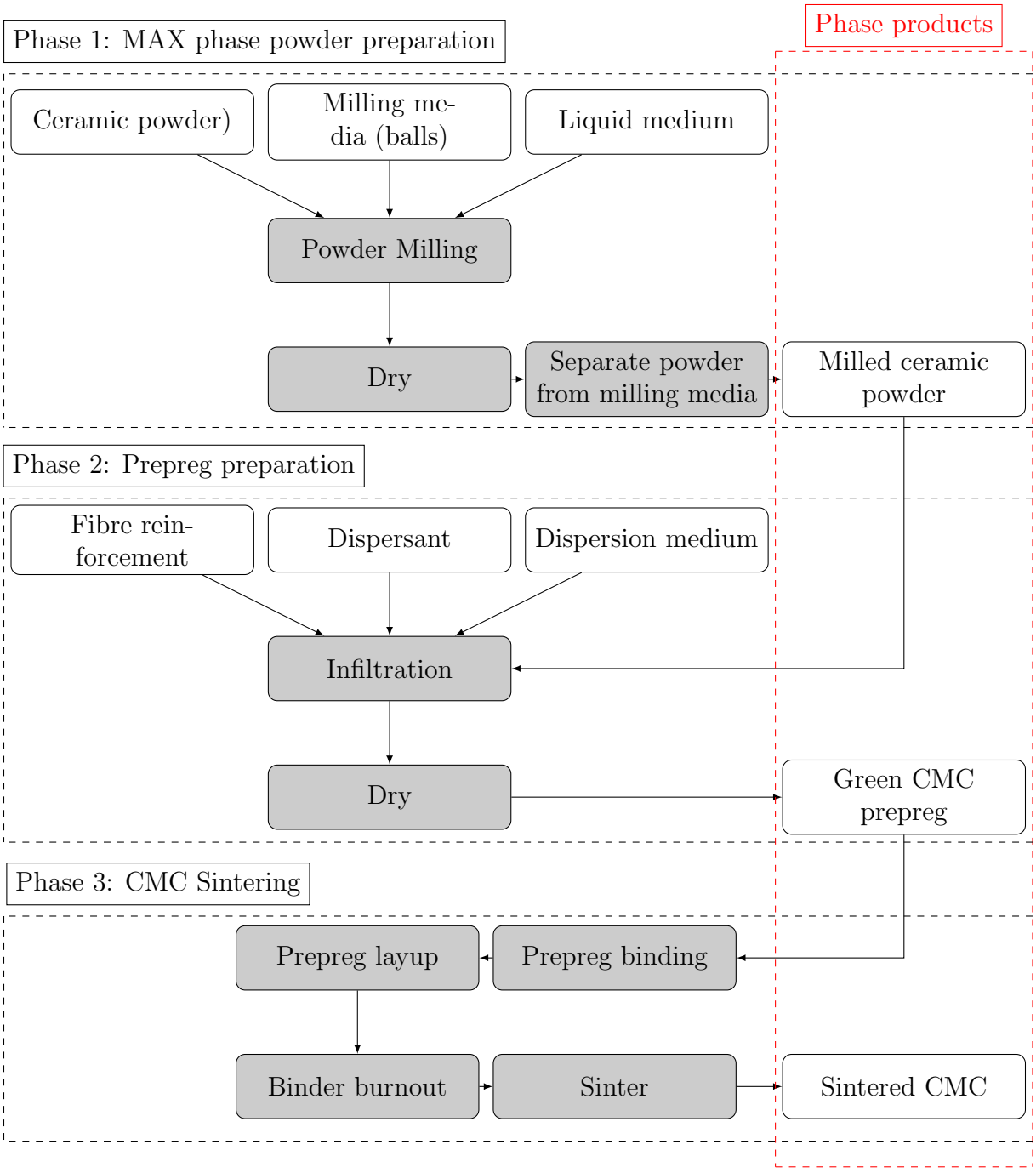

Figure 10: Schematic overview of the processing of the CMC.

4.2.1 Phase 1: MAX Phase Powder Preparation

Powder processing methods require the infiltration of powder particles within individual fibre bundles. Naturally, reducing the particle size improves the effectiveness of the infiltration process, allowing the powder particles to move between the carbon fibres.

The milling of Ti_2AlC powder was performed in a Szegvari vertical attritor mill (model: 01-HD, type: B, 1/4 HP) as shown in Figure 11a. The mill consists of a stationary 0.58 l zirconia milling chamber with a 4-pin stainless steel stirrer mechanism. The cylindrical pins are arranged 90°to each other. The milling chamber was filled with spherical alumina beads, see Figure 11b, with an average diameter of 1 mm. The Ti_2AlC powder, see Figure 11c, was introduced into the chamber in the form of a slurry with hexane as dispersing media. Samples were periodically extracted with a syringe for particle size analysis, as discussed in more detail in section 4.3.

(a)

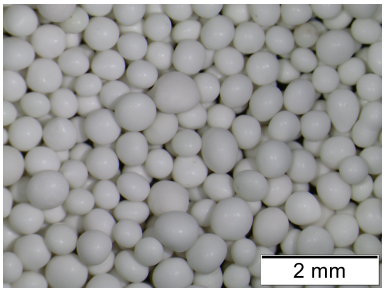

(b)

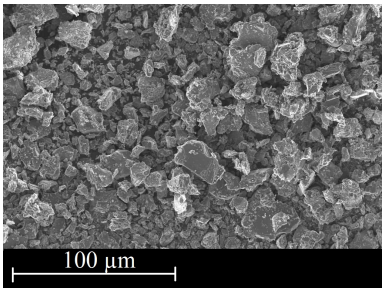

(c)

Figure 11: Attritor mill setup; (a) vertical attritor mill, (b) milling beads used for milling of Ti_2AlC, and (c) a SEM micrograph of the as-received Ti_2AlC powder.

Alumina beads were cleaned in the attritor mill by milling for 2 hours in hexane. A small amount of Ti_2AlC powder was included as abrasive material in order to

help clean the milling media. With larger alumina beads, sand would be used for this purpose and filtered out later. In this case the sand would be difficult to remove from the milling media as the particle diameters and densities may be quite similar. The milling was conducted at a speed of 300 rpm.

The MAX phase powder was milled using a (powder):(milling media):(liquid medium) mass ratio of 1:10:4. The powder was milled using the attritor mill at 600 rpm for 6 hours, with the alumina beads as milling media and hexane as the liquid medium. The milling operation was stopped at 1 hour, 2 hours, 4 hours, and 6 hours to extract samples for analysis. The characterisation of the samples are discussed in section 4.3. Hexane evaporates during milling, therefore additional hexane was added halfway through the milling operation to restore the mixture to its original state.

The milling operation was stopped after 6 hours and the contents of the milling chamber were dried in air. The milled powder was then separated from the milling beads using a 250 μm sieve along with an automatic sieve (model: Retsch As 200) for 20 minutes.

4.2.2 Phase 2: Prepreg Preparation

The three methods chosen for evaluation were electrophoretic deposition (EPD), vacuum infiltration, and pressure infiltration. A dispersant was used in all three cases to achieve a kinetically stable suspension. In the case of EPD, a more in-depth experimental trial was conducted to establish the amount of dispersant additive that would maximise yield. Green CMC samples consisting of fibre reinforcement and ceramic powder were made using each infiltration method. The method resulting in the best infiltration was selected to be used in the third phase of the project. The method used to assess the infiltration process is discussed in section 4.3.

EPD

EPD is used to deposit the h-BN powder as an interphase material and the Ti_2AlC powder as the matrix. The EPD apparatus consists of a Genesys^{TM} TDK-Lambda power supply (model: GEN600: 1.3, 0-600 Volts DC and 0-1.3 Amps DC range, 72 mV and 0.26 mA accuracy) which was connected to a sample clamp, housing the deposition electrode, and a square stainless steel electrode. The sample clamp is made of vesconite and a copper insert is used to ensure an electrical connection between the power source and the deposition electrode. A schematic of the EPD configuration is shown in Figure 13. Vesconite is used for the sample clamp due to its chemical resistance and good electrical insulating properties. The sample clamp, shown in Figure 12b, used for the trials exposes only a 15 mm diameter

area of the sample to the particle suspension. The electrodes were housed in a pyrex container, as shown in Figure 12, with the square stainless steel electrode acting as the anode and the clamped sample acting as the cathode. The square anode, pyrex housing, and sample clamp were sonicated in acetone before each experimental run in order to make sure they were clean.

It is critical that the particles are well dispersed in the suspension for effective EPD. Tests were conducted to find a suitable liquid medium for use in the EPD process. Three different dispersion mediums were evaluated for the EPD of both h-BN and Ti_2AlC, namely, distilled water, isopropyl alcohol, and acetone. Two different types of dispersant were evaluated, Dolapix CE64 and Lubrizol 2155. The dispersants were only evaluated in acetone as distilled water and isopropyl alcohol showed zero deposition yield of h-BN using EPD. With the addition of a dispersant, acetone succeeded in delivering an EPD coating when paired with h-BN or Ti_2AlC. Experiments were performed to establish the dispersant addition level resulting in maximum h-BN and Ti_2AlC deposition yield.

(a) (b)

Figure 12: EPD setup with: (a) EPD cell with the clamped foil sample acting as the cathode, (b) sample clamp showing clamped foil sample along with the copper insert.

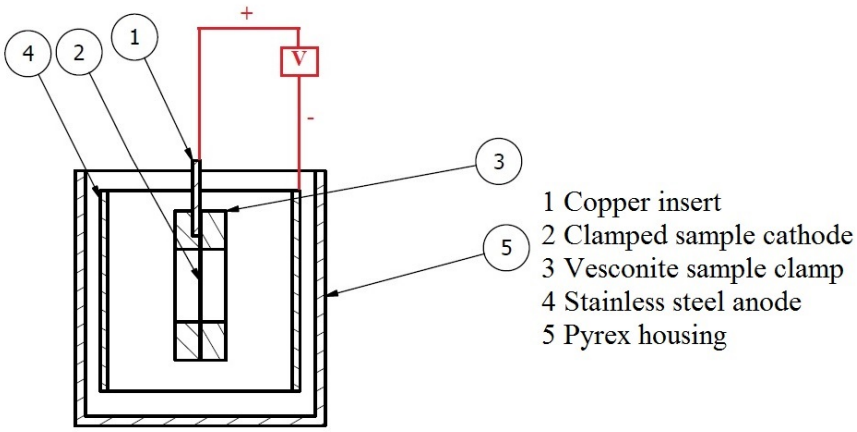

Figure 13: Labelled schematic of the EPD configuration showing a cross-sectional view.

Aluminium foil samples were used to evaluate the effect of the two different dispersants, in various concentrations. The two additives evaluated are Dolapix CE 64 and Lubrizol 2155. Aluminium foil samples, with dimensions of 20 mm × 30 mm, were polished with cotton wool and sonicated for 1 minute. Longer sonication times led to perforated samples caused by cavitation. A 5 g/l solution of each additive was prepared in distilled water for the h-BN dispersion and a 10 g/l solution for the Ti_2AlC dispersion. The diluted additive was added to a 1 g/l dispersion of h-BN and a 1 g/l dispersion of Ti_2AlC in pure acetone. The dispersions were sonicated for 10 minutes to break up agglomerates. The dispersions were introduced into the Pyrex housing and left for 2 minutes before applying a voltage to the electrodes.

EPD was performed at 20 V for 10 minutes for each sample. The samples were weighed before and after deposition using an analytical scale (model: Kern ABT 120-5DM) with a resolution of 0.00001 g to determine the deposition yield. After deposition, the samples were left to dry in air, removed from the clamp, and weighed. The resulting optimum in terms of deposition yield and uniformity of the coating is subsequently implemented for the coating of carbon fibres.

Plain weave carbon fibre samples, with dimensions 20 mm × 25 mm, were cleaned in an ultrasonic bath for 5 minutes in acetone while clamped and then rinsed with acetone. For interphase processing, h-BN powder was introduced into acetone at a concentration of 1 g/l, along with the optimum dispersant additive. Similarly, for matrix processing, Ti_2AlC powder was then introduced into acetone at a concentration of 2 g/l, along with the optimum dispersant additive. The dispersion

was then sonicated for 10 minutes in an ultrasonic bath to break up any agglomerated particles and 100 ml of the dispersion was introduced into the EPD cell and left for 1 minute before applying the voltage to the electrodes. Each trial was conducted at a fixed voltage and deposition time. The cathode was removed from the housing, once the deposition time was reached, and left to dry in air. Fibre samples were weighed after cleaning and again after EPD to determine the deposition yield.

Slurry and Sample Preparation for Vacuum Infiltration and Pressure Infiltration

A 30 vol % Ti_2AlC slurry was prepared for infiltration of the carbon weave in distilled water with the addition of 0.4 wt% Dolapix CE64 of the solids in the slurry. The slurry (100 ml) was stirred in a magnetic stirrer for 2 hours before infiltration. The same process was used for the preparation of a 5 vol % h-BN slurry. Additionally, a series of infiltration experiments were performed using 2.5 vol % and 5 vol % Ti_2AlC slurries in acetone with no dispersant. At solids loadings higher than 5 vol %, the slurries became too unstable. These slurries were sonicated for 10 minutes before each infiltration cycle.

A 30 mm diameter carbon fibre weave sample was cut and placed in a rigid plastic 30 mm diameter cold mounting cup. The slurry was poured over the disc, filling the cup to a height of approximately 1 mm. The carbon fibre weave layer is approximately 0.15 mm thick, therefore the slurry fully covers the sample. These samples were used for vacuum infiltration and pressure infiltration.

Vacuum Infiltration

Vacuum infiltration is used to infiltrate the h-BN powder as an interphase material and the Ti_2AlC powder as the matrix. Vacuum impregnation equipment, for typical cold mounting of epoxy resin metallurgy samples (model: Buehler Cast N' Vac system), was used for the vacuum infiltration. After the carbon fibre weave sample and slurry have been prepared in the cold mounting cup as discussed, a vacuum was applied to aid capillary forces in infiltrating the fibre bundles. Vacuum was applied for 10 minutes. The vacuum pump was switched off and the pressure was allowed to normalise. After infiltration, the samples were left to dry in air. Fibre samples were weighed before and after infiltration to determine the yield. The infiltration cycles were performed multiple times.

Pressure Infiltration

Pressure infiltration is used to infiltrate the h-BN powder as an interphase material and the Ti_2AlC powder as the matrix. The cold mounting cup with slurry and carbon fibre sample was placed in a 12 ton hydraulic press (model: Carver Model C). Pressure infiltration was conducted by inserting a 30 mm epoxy plug into the cup and applying a 6 MPa load for 10 minutes. Figure 14 shows a schematic

representation of the pressure infiltration process. After infiltration, the samples were left to dry in air. This infiltration process was repeated twice with all samples. Fibre samples were weighed before and after infiltration to determine the yield.

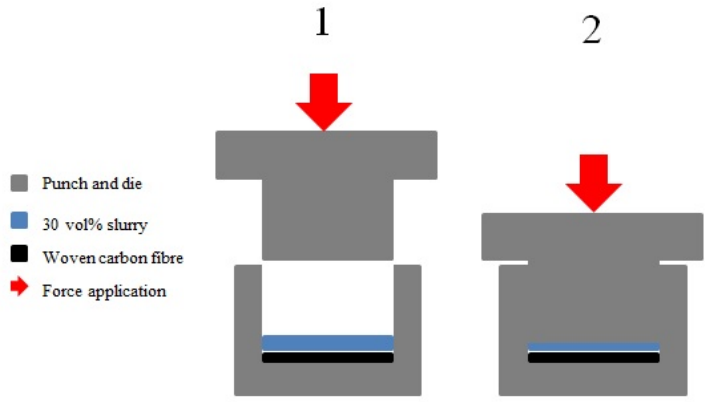

Figure 14: Schematic representation of pressure infiltration.

4.2.3 Phase 3: CMC Consolidation by SPS

Prepreg CMC samples were made using the chosen infiltration method. After drying, the so-called green CMC prepreg samples were bound. This allows the prepreg to be handled easily while remaining flexible. Samples are then sintered after cutting, stacking, and binder burnout. The consolidated samples were then characterised as discussed in section 4.3.

In order to assemble the CMC prepreg in layers to create the CMC component, the prepreg layers were coated with a PMMA solution. The PMMA solution was prepared by dissolving PMMA in acetone using a magnetic stirrer in a 2 vol% solution. The samples were dipped in the solution and left to dry in air. This ensured that the samples could be handled while remaining flexible as a prepreg should be. The CMC component was assembled by placing prepreg layers in a 0°-90° stack by hand, 8 layers high.

Debinding

Debinding was performed to remove all the PMMA, used as a binder, before composite consolidation. The debinding treatment could not be performed in the SPS furnace as the rapid expansion of gasses in the enclosed die, due to the rapid heating rates of the furnace, would have caused an explosion. The 30 mm samples were placed in an alumina boat inside a tube furnace. Debinding was

performed at 400 °C for 60 minutes in an argon atmosphere with a heating rate of 5 °C/min. According to the TGA analysis performed by (Even et al., 2008), shown in Figure 9, this temperature profile is sufficient to remove all PMMA.

Sintering
The discs were sintered in an SPS furnace (model: FCT systeme GmbH HPD5), the concept of which is explained in section 2.3. SPS was chosen due to its high heating and cooling rates as well as short hold times. Additionally, SPS delivers highly densified near net-shape parts. An advanced method was necessary due to the complexity of the constrained sintering of continuous fibre reinforced composites. The outside surfaces of the samples were coated with h-BN powder in an aqueous suspension by using a brush. The samples were then dried leaving only the h-BN powder behind to ensure that the samples can be removed from the die after the application of heat and pressure. The 30 mm samples were placed inside a graphite die. Sintering was performed using a mechanical pressure of 20 MPa and a temperature of 1400 °C for 7 minutes. Additionally, the heating and cooling rates used were 200 °C/min and sintering was performed under vacuum (5×10^{-2} mbar).

The temperature measured in the SPS furnace is the temperature of the graphite die during sintering. This is measured using a thermocouple that only registers temperatures above 400 °C. This means that the temperature profile during the first and last few minutes are not described. Temperatures below 400 °C are of no interest in this case.

4.3 Characterisation Techniques

This section describes the analytical techniques used to characterise the products of the three processing phases as discussed in section 4.2. The theories behind the techniques are briefly explained, where relevant, as well as the facilities used and the sample preparations.

4.3.1 Particle Size Analysis

Two distinct methods were used to determine the particle size distribution of the as-received and milled Ti_2AlC powder as well as the h-BN powder. The particle size distribution of the powder is important for evaluating the milling process as well as assessing the chance of success of the process used to infiltrate the powder into a fibrous weave. Additionally, the size distribution will have a significant

effect on the sintering behaviour of the green composite and on the properties of the consolidated composite.

Different particle size analysis techniques are used for different particle size ranges. Laser diffraction is suited to powders when the majority of the particles are larger than 1 μm. For smaller particles, dynamic light scattering (DLS) is a more appropriate technique.

A Malvern Mastersizer 2000 was used for laser diffraction analysis to determine the particle size distribution of the as-received Ti_2AlC powder. The powders were suspended in distilled water and sonicated for 10 minutes before analysis. A laser beam is passed through particles in suspension and the diffraction patterns are measured. This is then used along with Fraunhofer diffraction theory, which states that particle size is specific to the intensity and angle of the light scattered by individual particles (McCave et al., 1986). Fraunhofer diffraction is an approximation of the Mie scattering theory. The approximation was used due to its insensitivity to the choice of refractive index of the particles analysed. This approximation can be valid for larger particle sizes. A refractive index of 1.33 was used for the liquid medium.

Malvern Zetasizer Nano ZS was used for the DLS analysis to determine the particle size distribution of the milled Ti_2AlC powder as well as the h-BN powder. The powders were suspended in distilled water and sonicated for 10 minutes before analysis. Polarised light is passed through particles in suspension and the change of scattering intensity of diffracted light is measured (Urban and Schurtenberger, 1998). This change in intensity is due to the particles undergoing Brownian motion. This is used in an algorithm to determine the particle size distribution.

Both types of analyses, laser diffraction and DLS, were conducted at the School of Chemical and Metallurgical Engineering at the University of the Witwatersrand. A Malvern Mastersizer 2000 was used for the laser diffraction analysis and a Malvern Zetasizer Nano ZS was used for the DLS analysis.

4.3.2 Optical Microscopy

Polished cross-sectional samples were examined to establish the success of the infiltration process used. In order to investigate sample cross-sections, samples were mounted in an epoxy resin (Struers EpoFix) under vacuum to fill all pores. This was done to ensure the integrity of the sample during grinding and polishing. Grinding and polishing was performed using an automated rotary grinding/polishing machine (Buehler). The sample preparation started with a grinding operation, followed by a fine grinding operation, and finally three polishing op-

erations. The grinding operation was performed using SiC paper (320 grit) with water as a lubricant. The fine grinding operation was performed using a Hercules S grinding disc along with a 9 μm diamond paste. The polishing operations were performed using VerdTex polishing cloths with 9 μm, 3 μm, and 1 μm diamond paste. An inverted metallurgical microscope (make: Olympus, model: GX 51) connected to a digital imaging system (make: Olympus, camera: SC30, software: Stream Essentials) was used for the imaging.

4.3.3 Scanning Electron Microscopy

Powder samples, polished surfaces, and fracture surfaces were analysed using scanning electron microscopy (SEM). The powder morphology and size of the powders affect the processes involved in fabricating the composite, while the nature of the fracture surface and polished cross-section give insight into the properties of the composite. Therefore it is important to be able to observe and analyse these characteristics.

Where an optical microscope uses visible light combined with a series of lenses to yield a magnified image, SEM makes use of a high energy electron beam to scan the surface of a sample. SEM images have a large depth of field, which makes it useful for studying powder samples, fibre samples, and fracture surfaces. Optical microscopy is not suitable for these purposes due to a shallow depth of field.

Powder morphology and powder particle size of the Ti_2AlC and h-BN were observed using SEM imaging. A Zeiss Merlin FE-SEM at 5 kV and 250 pA was used for the analysis. Small amounts of the powder were spread over a piece of carbon adhesive tape and stuck onto a 10 mm aluminium stub. The powder was then coated with gold using a sputter coater (model: Edwards S150b). The conductive Ti_2AlC powder was coated with gold to avoid any electron build up at contamination sites caused by the milling process and to minimise interference of the carbon content in the sample with that of the sputter coating.

Polished samples were observed using SEM imaging to view fibre matrix interaction in the CMC. A Zeiss Merlin FE-SEM at 20 kV and 110 nA along with a backscatter electron detector was used for the analysis. The samples were prepared exactly as the polished samples for optical microscopy, as discussed in section 4.3.2, and subsequently coated with gold.

Fracture surfaces were observed using SEM imaging to investigate the behaviour of the CMC. A Zeiss Merlin FE-SEM at 3 kV and 200 pA was used for the analysis. Fragments of the sample after fracturing were prepared in the same way as the powder samples. SEM analysis was conducted at the Central Analytical Facility's

(CAF) Electron Microbeam Unit at Stellenbosch University.

4.3.4 Energy Dispersive Spectroscopy

Elemental analysis was performed on as-received and milled (1, 2, 4, 6 hrs) Ti_2AlC powder as well as the resulting composite material by energy dispersive X-ray spectroscopy (EDS). This was done to establish the extent of contamination caused by the milling operation in the powder and to investigate the interaction between matrix and fibre reinforcement caused by the sintering process. EDS takes place inside a SEM. The same samples and facilities, as discussed in section 4.3.3, were used for the EDS analysis. For the as-received Ti2AlC powder, spot analysis was performed on individual particles; for all milled powder samples a representative area was chosen for spot analysis due to the powder particle size being significantly reduced. Spot analysis was performed at 5 different sites for each sample. For analysis of the CMC, area spot analysis, line analysis and elemental mapping were used to evaluate the distribution of elements in the composite.

EDS relies on the principle that each element has a unique atomic structure and therefore has a unique reaction to X-ray or electron beam excitation. This reaction can then be used to determine the elemental composition of a sample.

4.3.5 X-Ray Computed Tomography

Low resolution X-ray computed tomography (CT) scanning was employed to compare sintered samples and to detect large defects in the samples. High resolution CT scanning was employed to detect smaller defects in the samples as well as the internal structure.

CT relies on dedicated algorithms to reconstruct a three-dimensional (3D) volume using projected images from 360° around the object (du Plessis et al., 2016). The object to be scanned is placed on a stage inside the CT scanner. X-rays are used to image the object while the object is turned on the stage. After scanning, the generated images are combined to create a 3D volume.

Multiple sintered samples were scanned at the same time to evaluate the similarity between them and to identify large defects. Scanning was conducted at 120 kV and 200 μA with a voxel size of 25 μm using a 0.5 mm copper filter. A micro-CT (model: General Electric VTomex L240) was used to take 3,000 images at the (CAF) CT scanner facility at Stellenbosch University (du Plessis et al., 2016).

A single sintered sample was scanned to identify defects in more detail. Scanning was conducted at 120 kV and 90 μA with a voxel size of 10 μm using a 0.5 mm copper filter. A micro-CT (model: General Electric VTomex L240) was used to take 3,200 images at the Central Analytical Facility's (CAF) CT scanner facility at Stellenbosch University (du Plessis et al., 2016).

A 2 mm section of a CMC sample was cut for nano-CT scanning. Nano-CT scanning was conducted to see more detail within the sample when compared to the micro-CT scanning. Scanning was conducted at 70 kV and 220 μA with a voxel size of 2 μm. 2400 images were taken using a nano-CT (model: General Electric Nanotom S) at the Central Analytical Facility's (CAF) CT scanner facility at Stellenbosch University (du Plessis et al., 2016).

4.3.6 X-Ray Powder Diffraction

X-ray powder diffraction (PXRD) was used to analyse the crystal structure of Ti_2AlC during stages of production. This was done to establish the effect of operations on the Ti_2AlC powder, such as milling.

Similar to EDS, XRD relies on the detection of diffracted X-rays. X-rays are generated in an x-ray tube and directed towards the sample. The resulting diffracted x-rays are detected, processed, and counted. Diffraction patterns are then compared to standard reference patterns.

XRD analysis was conducted at the Crystal Characterisation Unit of the Department of Chemistry and Polymer Science at Stellenbosch University. A Bruker D2 Phaser X-ray diffractometer was employed for this purpose. A Cu tube (λ=1.54184 Å) was used as radiation source with X-rays produced at 30 kV and 10 mA. Continuous scans were taken in a 2θ range of 5° to 80° with a scan rate of 1.94 deg/min.

4.3.7 Density Analysis

Density measurements were performed on consolidated CMC specimens as well as Ti_2AlC specimens, using the Archimedes wet/dry method, to determine apparent densities as well as open porosity fractions. The dry mass, m_d, of specimens were recorded. The specimens were then submerged in distilled water and the suspended mass, m_s, was recorded. The specimens were then removed from the distilled water and the wet mass, m_w, was recorded. The sintered densities, ρ_a,

were calculated as:

$$\rho_a = \frac{m_d}{m_w - m_s} \times \rho_{water} \tag{7}$$

The percentage open porosity, ϵ, was calculated as:

$$\epsilon = \frac{m_w - m_d}{m_w - m_s} \times 100 \tag{8}$$

4.3.8 Mechanical Testing

Biaxial bending tests where performed on consolidated CMC and Ti_2AlC samples in order to compare the strength values and characteristics of the sintered discs. The stress distribution in real components is much more likely to be biaxial than uniaxial. Therefore biaxial testing of ceramics is more relevant and favoured for many applications (Borger et al., 2002). Additionally, biaxial strength testing has several advantages compared with uniaxial testing. This includes ease of specimen preparation as well as the fact that the test is independent from edge defects (Rasche et al., 2014). Popular biaxial testing methods are the ring-on-ring test (Fessler and Fricker, 1984), the ball on ring test (Matthewson and Field, 1980), and the ball on ring of balls test (Godfrey and John, 1986). These methods suffer from the disadvantage that stress results are not interpretable when perfectly flat disc specimens are not used (Morrel et al., 1999). Other methods have been devised to be less dependant on the flatness of specimens, none more tolerant to geometrical inaccuracies that the ball on three balls test (B3B) (Borger et al., 2002). Figure 15 shows a schematic illustration of the ball on three balls test configuration.

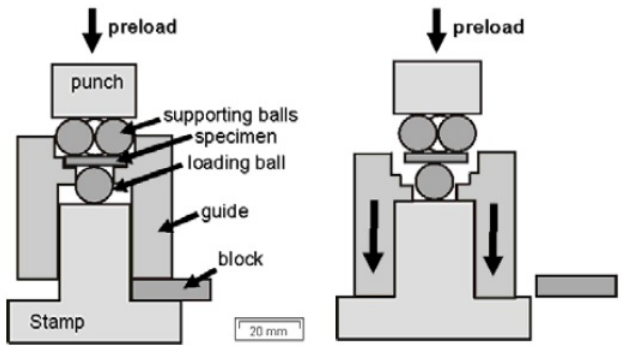

Figure 15: Experimental configuration of the ball on three balls test (Danzer et al., 2007).

The B3B test method involves supporting a sintered disc with three touching balls and loading the opposite face with a fourth centred ball. The strength is the maximum tensile stress in the disc occurring on the disc surface opposite the loading ball. There are various analytical approximations for the stress distribution in centrally loaded biaxial discs, all of which are based on the linear-elastic axisymmetric thin-plate theory (Borger et al., 2002). Additionally, they depend on the contact radius between loading ball and disc. This is not a trivial problem as the contact radius increases non-linearly with an increase in load. Borger et al. (2002) showed that the approximation of Shetty et al. (1980) gives stress results in accordance with their own finite element results for specimen thickness to specimen radius ratios larger than 0.05. The approximation of the contact radius by Shetty et al. (1980) is, however, overestimated several times. The maximum stress in the disc is approximated as (Shetty et al., 1980):

$$\sigma_{max} = \frac{3\ F\ (1+\nu)}{4\ \pi\ t^2} \times \left[1 + 2\ ln\frac{R_a}{b} + \frac{(1-\nu)}{(1+\nu)}\left(1 - \frac{b^2}{2\ R_a^2}\right)\ \frac{R_a^2}{R^2}\right] \tag{9}$$

where

$$b = t/3 \tag{10}$$

and

$$R_a = \frac{2\ \sqrt{3}}{3}\ R_b \tag{11}$$

with F as the applied load at failure [N], ν is the Poisson's ratio of the disc, t is the thickness of the disc [mm], R_a is the support radius [mm], R_b is the ball radius [mm], b is the contact radius [mm], and R is the disc radius. Borger et al. (2002) identified two situations where the model is likely to fail. Firstly, failure may occur due to Hertzian contact stresses if the ball radius is too small and/or the specimen thickness is too large. Secondly, failure may occur due to buckling if the specimen is too thin.

Fracture tests were performed on sintered discs with a nominal diameter of 29.5 mm and thickness between 0.8 and 0.9 mm. The samples were ground by hand to adjust the diameter from the sintered state to fit within the positioning guide. The stainless steel supporting and loading balls (bearing balls) all have a diameter of 22 mm. The balls were centrally positioned by a rotationally symmetric guide. A preload of approximately 10 % of the fracture load was applied and the guide was moved down and out of the way as illustrated in Figure 15. At this point the specimen was pinned between the supporting balls and the loading ball as shown in Figure 16.

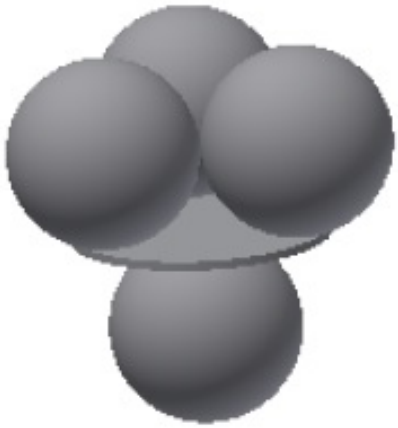

Figure 16: Configuration of the disc specimen, supporting, and loading balls.

The tests were performed at the Centre for Materials Engineering at the University of Cape Town. The testing was conducted at a controlled displacment rate of 0.5 mm/min on a 5 kN electromechanical load frame and controller (model: Instron 3365). The uniaxial load applied to the specimen was measured using a 1 kN load cell with an accuracy of $\pm$ 0.5 %. The crosshead displacement was measured throughout the duration of the test.

4.3.9 Volume Fraction Calculations

The fibre, matrix, and pore volume fractions of green and sintered CMC discs were estimated by using dimensional measurements and the theoretical densities of the constituents. The mass of the fibres in a sample is measured before infiltration. Thereafter, the mass of the matrix is calculated from the difference in mass before and after infiltration. A flat anvil micrometer, with a resolution of 20 μm, was used to measure the thickness of green and sintered samples. Measurements were recorded on five sites, as shown in Figure 17, on each sample and the average was used in volume calculations. The theoretical densities used are 4.11 g/cm^3 for the Ti_2AlC matrix and 1.74 g/cm^3 for the carbon fibres as calculated in section 4.1. The calculations are shown in Appendix C.

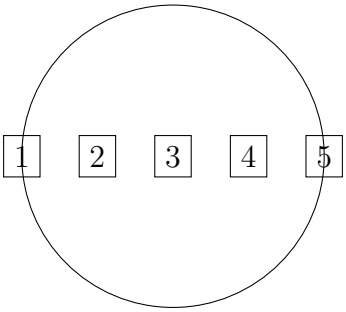

Figure 17: Thickness measurement sites on 30 mm samples.

4.4 Characterisation of the Production Process

4.4.1 Phase 1: Milled Ti_2AlC Powder

The techniques applied for the characterisation of the phase 1 product are outlined in this section. The milled Ti_2AlC powder was characterised using particle size analysis, SEM, EDS, and PXRD.

Particle size analysis, discussed in section 4.3.1, was performed to determine whether the powder could be milled to a size sufficiently small to allow the particles to be infiltrated into fibre bundles. Additionally, the analysis aimed to determine the effect of the milling operation on the particle size distribution and the level of agglomeration. SEM analysis, discussed in section 4.3.3, was performed in order to validate particle size analysis results and to assess the effect of the milling operation on particle morphology. EDS analysis, discussed in section 4.3.4, was performed to determine the extent of the contamination caused by the alumina milling beads. PXRD analysis, discussed in section 4.3.6, was performed to determine the effect of the milling procedure on the structure of the powder.

4.4.2 Phase 2: Infiltrated CMC Prepreg

The techniques applied for the characterisation of the phase 2 product are outlined in this section. The green CMC prepreg was characterised using optical microscopy and volume fraction calculations.

Optical microscopy, discussed in section 4.3.2, was used to evaluate the success of EPD, vacuum infiltration, and pressure infiltration. This was done by viewing polished cross-sections of infiltrated samples under a microscope. Volume fraction calculations, discussed in section 4.3.9, were used to estimate the volume fractions

of the constituents. This was done to compare the volume fractions of the green CMC with that of the sintered CMC.

4.4.3 Phase 3: Sintered CMC Disc

The techniques applied for the characterisation of the phase 3 product are outlined in this section. The sintered CMC was characterised using volume fraction calculations, density analysis, CT scanning, B3B failure testing, nano-CT, SEM, and EDS.

Volume fractions, discussed in section 4.3.2, were calculated for the sintered CMC to determine the effect of the sintering operation on the volume fractions. Density analysis, discussed in section 4.3.7, was performed to determine the apparent density of the CMC as well as the open porosity. CT scanning, discussed in section 4.3.5, was performed to establish similarity between multiple CMC samples to show that the process is repeatable. B3B failure testing, as discussed in section 4.3.8, was performed on CMC discs as well as Ti_2AlC discs in order to compare their strengths and behaviour under stress. Nano-CT follows the same principles as normal CT, or micro-CT, just at a different scale. The Nano-CT was used to scan a small fragment of the CMC in order to see more detail within the CMC sample than the micro-CT could show. SEM analysis, as discussed in section 4.3.3, was performed to investigate fracture surfaces following the B3B testing and to investigate a polished cross-section of the CMC. Finally, EDS analysis, as discussed in section 4.3.4, was performed to investigate the interaction of matrix and fibre in the CMC.

5 Results and Discussion

This section presents the results of the experimental methods outlined in section 4. Additionally, the results of the processing methods and characterisation are discussed.

5.1 Raw Materials

The analysis and discussion of the as-received ceramic powders are discussed in this section. The as-received h-BN and Ti_2AlC powders were analysed using secondary electron scanning electron microscopy (SE-SEM) and particle size analysis. The SEM was performed to confirm particle size analysis results and particle morphology. The sizes of the h-BN and Ti_2AlC powder, as indicated by the suppliers, led to two separate methods of particle size analysis. Dynamic light scattering (DLS) for the h-BN powder and laser diffraction for the Ti_2AlC powder. Both these methods are briefly discussed in section 4.3.1. Particle size and SEM analyses for both powders were conducted as explained in section 4.3.1 and section 4.3.3 respectively. Figure 18 shows SEM micrographs of (a) h-BN powder and (b) Ti_2AlC MAX phase powder.

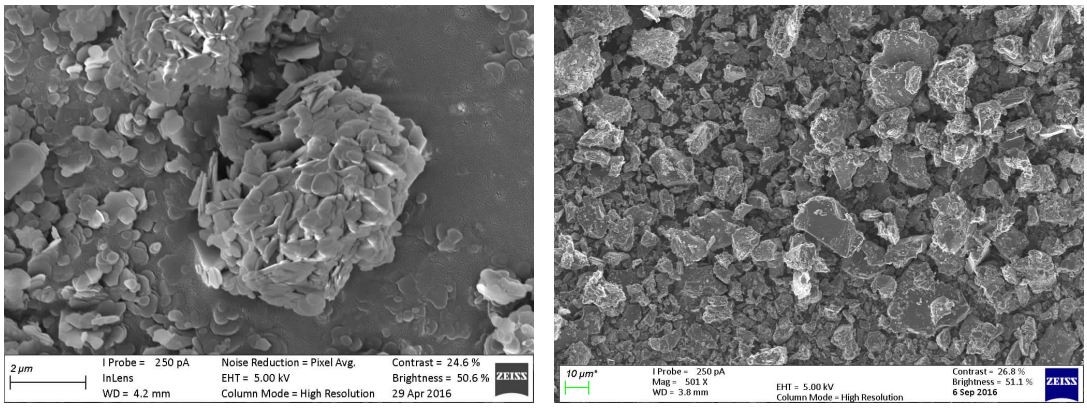

(a) (b)

Figure 18: SE-SEM micrograph of (a) h-BN powder and (b) as-received Ti_2AlC powder.

Figure 18a shows a large agglomerate, which can be expected due to the hygroscopic nature of the h-BN. This shows the importance of proper preparation of the powder to break up particle aggregates before electrophoretic deposition (EPD).

The powder particles have a typical plate-like shape as expected. The dynamic light scattering (DLS) particle size analysis indicated an average particle size of 1.16 μm. The particle size distribution is shown in Figure 19. This correlates with the SEM micrograph in Figure 18a.

Figure 18b shows a SEM micrograph of the Ti_2AlC powder. The Ti_2AlC is observed to have angular morphology due to the crushing of bulk material after synthesis. The laser diffraction particle size analysis is reported in Table 2 and the particle size distribution is shown in Figure 19. The D_{10}, D_{50}, and D_{90} particle sizes indicate the particle sizes for which 10 vol%, 50 vol%, and 90 vol% of the particles are smaller. The results correlate to the SEM micrograph in Figure 18b, indicating there is a normal distribution of particle sizes from around 5 to 35 μm.

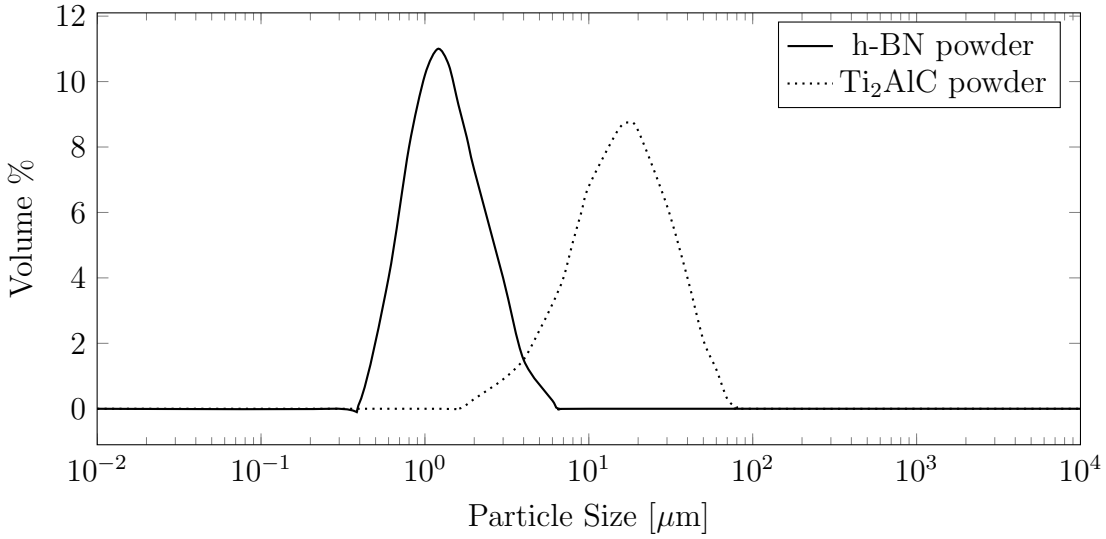

Figure 19: Particle size distribution of h-BN powder and Ti_2AlC powder as measured using DLS and laser diffraction, respectively.

Table 2: Particle size results for as-received Ti_2AlC powder.

D10 particle size [μm]	**D50 particle size [μm]**	**D90 particle size [μm]**
6.09	16.01	36.84

5.2 Phase 1: MAX Phase Powder Preparation

Ti_2AlC powder was milled in order to reduce particle size to enable infiltration of powder particles into a carbon fibre preform. The milling procedure is outlined in section 4.2.1. The techniques used to characterise the milled powder are discussed in section 4.4.1. Samples extracted at various milling intervals were analysed using SEM, energy dispersive spectroscopy (EDS), X-ray powder diffraction (XRD), and particle size analysis. The results of these analyses are discussed in this section.

5.2.1 Ti_2AlC Powder Characterisation

SEM micrographs for the as-received Ti_2AlC powder as well as the subsequently milled Ti_2AlC Powder are shown in Figure 20. The as-received powder is shown to have angular morphology. Figure 22 shows a high magnification SEM micrograph of the powder where the rounded particle morphology can be better observed. Very little particle agglomeration can be seen, even in the milled samples where surface energy is high due to the small particles.

Particle size analysis was conducted as discussed in section 4.3.1. Laser diffraction was used to analyse the particle size analysis of the as-received powder. Thereafter, due to the particle size reduction effect of the milling, dynamic light scattering (DLS) was used to measure the particle size distribution of the milled powder after 1, 2, 4, and 6 hours of milling. Figure 21 shows the evolution of particle size distribution during milling of the Ti_2AlC powder. Figure 23 shows the mean particle sizes for the as-received and milled powder. It is important to note that the mean particle size indicated from the laser diffraction analysis (as-received powder) is the D50 particle size, indicating the particle size for which 50 vol% of the particles are smaller. While the average particle sizes indicated for the DLS analysis (milled powder) is the Z-average particle size, which is the intensity weighted harmonic mean particle size. The Z-average is the preferred DLS size parameter as it is insensitive to noise. The D50 and Z-average sizes are normally close, but not equal.

The laser diffraction analysis of the as-received Ti_2AlC powder indicated a normal distribution with peak at 16 μm and width from 2 μm to 70 μm. This correlates well with the SEM analysis as shown in Figure 20a. After 1 hour of milling, the large particles have been crushed, moving the size distribution peak from 16 μm to 550 nm. The peak now spans from 300 nm to 900 nm. A secondary peak still remains in the region of 5 μm to 6 μm as can be seen from the SEM micrograph in Figure 20b and the DLS results in Figure 21.

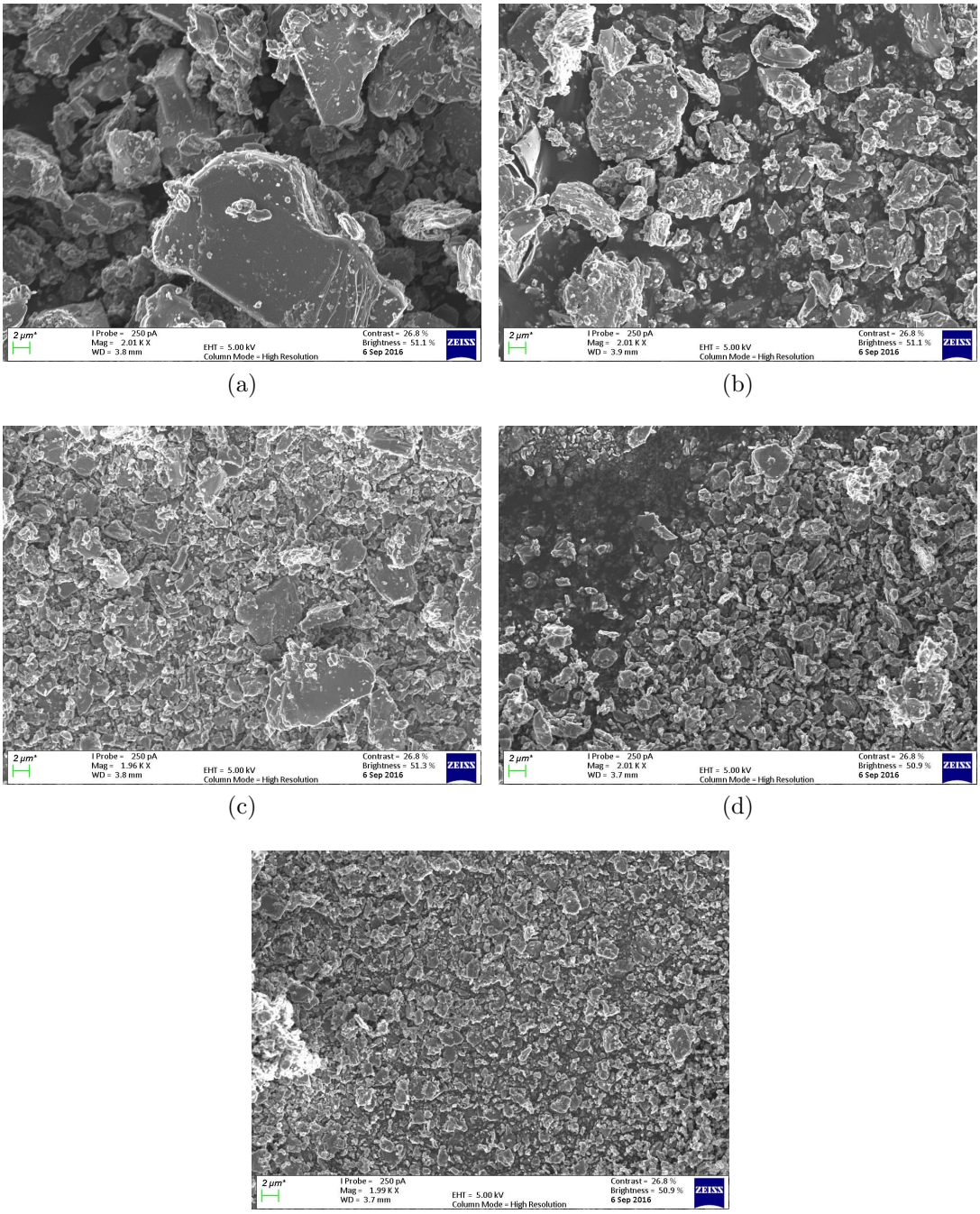

Figure 20: SE-SEM micrograph of Ti_2AlC powder: (a) as-received, (b) milled for 1 hour, (c) milled for 2 hours, (d) milled for 4 hours, (e) milled for 6 hours.

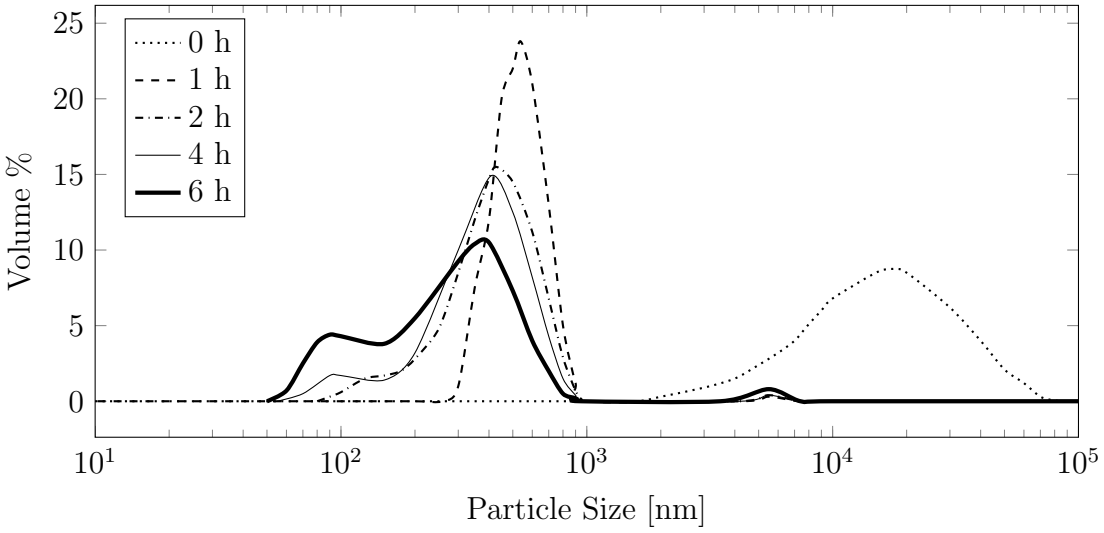

Figure 21: Particle size distribution.

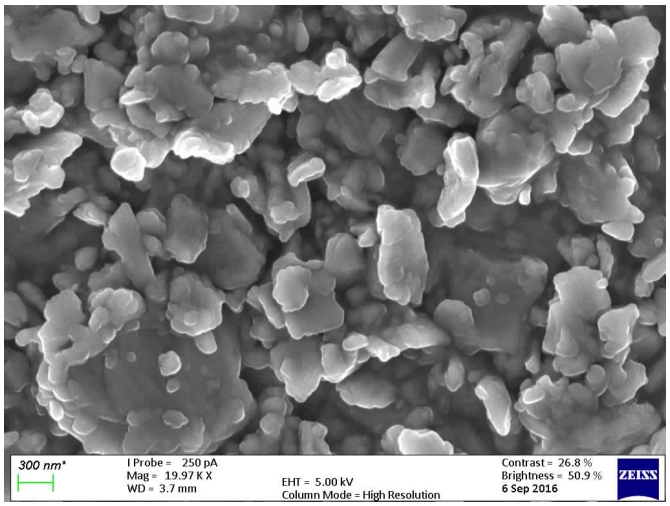

Figure 22: SE-SEM micrograph of Ti_2AlC powder, milled for 6 hours, at high magnification.

After 1 hour of milling, the large particles have been crushed, moving the size distribution peak from 16 μm to 550 nm. The peak now spans from 300 nm to 900 nm. A secondary peak still remains in the region of 5 μm to 6 μm as can be seen from the SEM micrograph in Figure 20b and the DLS results in Figure 21. After 2 hours of milling, the main peak has shifted to 450 nm and spans from 80 nm to 900 nm as shown in Figure 20c and Figure 21. After 4 hours

of milling, the main peak has shifted to 400 nm and spans from 60 nm to 900 nm as shown in Figure 20d and Figure 21. After 6 hours of milling, the main peak remains at 400 nm and spans from 50 nm to 900 nm as shown in Figure 20e and Figure 21.

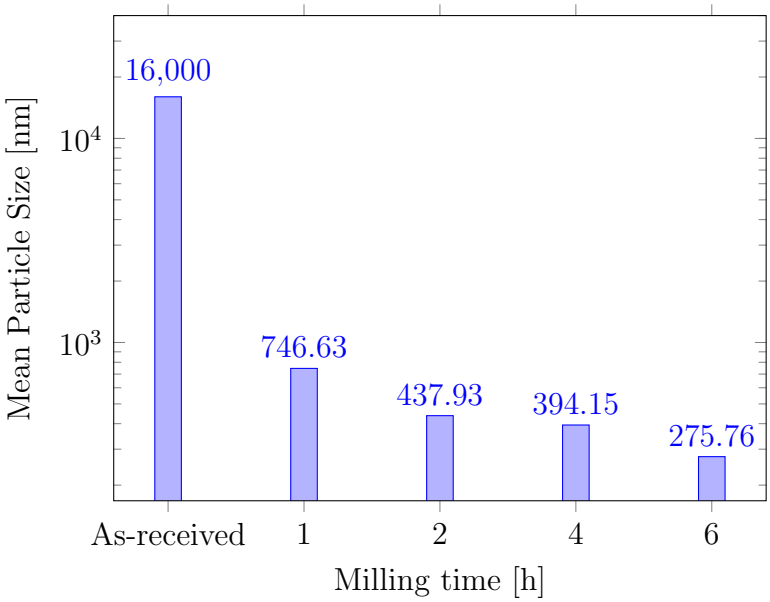

Figure 23: Evolution of mean particle size with milling time for as-received Ti_2AlC powder and powder milled for 1, 2, 4, and 6 hours.

The small secondary peak around 5 μm remains in the DLS results throughout the duration of the milling. As time progresses, the main peak in the particle size distribution widens and shifts to a bimodal distribution. It is possible that increasing the milling time further would eventually lead to a unimodal peak at a smaller particle size. No further milling was performed as the bimodal size distribution increases packing density. Packing density increases up to a particle size ratio of approximately 7:1 (German, 2005). After 6 hours of milling, the particle size ratio of the bimodal peak is approximately 5:1, which is deemed sufficient. Additionally, the particle morphology becomes more rounded as milling time progresses. This is shown in Figure 22.

5.2.2 Ti_2AlC Powder Elemental Analysis

EDS analysis was performed, as outlined in section 4.3.4, to determine the effect of the milling procedure on the Ti_2AlC powder. The main objective was to identify

contamination as caused by the alumina milling beads. Therefore the analysis focused only on oxygen, aluminium, and titanium. The analysis results are summarised in Figure 24. The increase in oxygen content can give some indication of the degree of contamination caused by the milling process. It should be noted that EDS is not a highly accurate chemical analysis technique, especially for low atomic number elements such as O and C, but for the purposes of establishing the increase of contamination during milling it is deemed sufficient. EDS can deliver results to ± 5 wt% when measuring major constituents (mass concentration larger than 0.1 (10 wt%)) (Newbury and Ritchie, 2014). Carbon analysis was omitted, due to the inaccuracy of low atomic number elements. This means that the values reported in Figure 24 can only be used for relative comparison and are not quantitatively accurate.

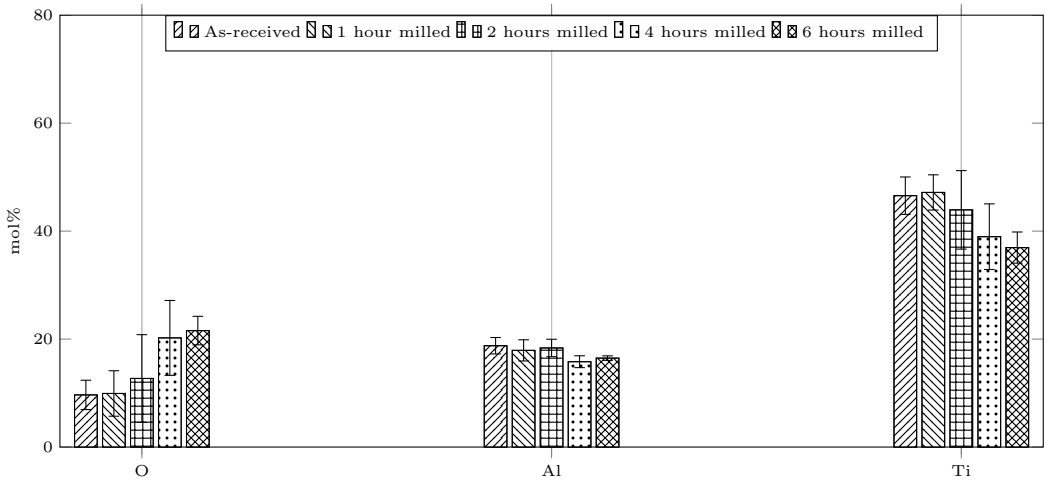

Figure 24: As-received and milled Ti_2AlC powder EDS analysis results.

The oxygen contamination appear to be minimal up to the duration of 2 hours. From there it increases more drastically with an increase in milling time. The results show a steady drop in the titanium content as milling time progresses. The aluminium content does not vary much, which makes sense as the composition of alumina is Al_2O_3.

The only likely contamination is that of the alumina milling beads. This then follows that the absolute O and Al content will increase and the absolute Ti will remain constant. Similarly, this means that the relative O and Al content will increase and the relative Ti content will decrease. The relative Al content will not increase as much as the relative O content seeing as the powder contains significant amounts of Al before milling and the relation between Al and O added

is 2:3.

Keeping this in mind, observing the relative drop in titanium content and rise in oxygen content with increased milling duration, indicates that there was a progressive contamination of the powder. This is probably due to contamination by the alumina milling beads. This is investigated further using XRD analysis.

Figure 25 shows the XRD patterns for the as-received and milled Ti_2AlC powder. The peaks of three phases were matched using open source MAUD software. The phases identified were Ti_2AlC, Al_2O_3, and TiC. The phases were present in all the samples. This was expected as the as-received powder specification indicated that the powder consists of those three phases (Carbon-Ukraine, 2015).

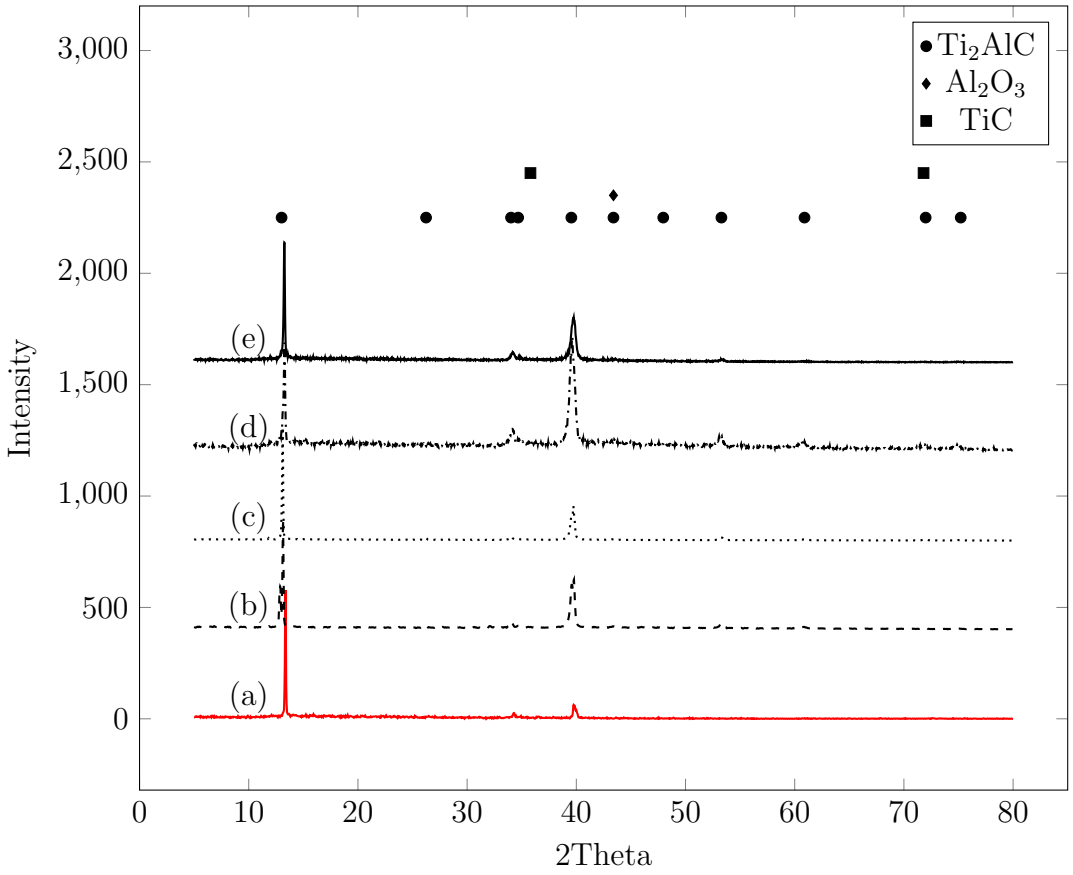

Figure 25: XRD patterns of (a) as-received, (b) 1 hour milled, (c) 2 hours milled, (d) 4 hours milled, and (e) 6 hours milled Ti_2AlC powder.

5.3 Phase 2: Prepreg Preparation

Carbon fibre weave samples were infiltrated with ceramic powder using EPD, vacuum infiltration, and pressure infiltration. The infiltration methods are discussed in section 4.2.2. This section gives the results of the infiltration experiments and the characterisation of the green CMC. The methods for characterising the CMC prepreg are discussed in section 4.4.2.

5.3.1 Electrophoretic Deposition

This section gives the results of the EPD experiments performed to determine the optimum amount of dispersant additive for h-BN and Ti_2AlC powder in suspension as well as the coating of carbon fibres.

Effect of dispersant on h-BN deposition
h-BN was deposited onto aluminium foil while varying the content of dispersant in the suspension. This was done to determine the optimum dispersant content in terms of deposition yield. The procedure for coating aluminium foil samples with h-BN using EPD is outlined in section 4.2.2. Figure 26 shows the relationship between the deposition yield and the amount of dispersant added to the dispersion. The deposition yield was calculated as:

$$yield_{EPD} = \frac{m_f - m_i}{2 \times \pi \times r^2} \tag{12}$$

where m_i is the mass of the sample before deposition, m_f is the mass of the sample after deposition, and r is the radius of the area of the sample exposed to the suspension. The samples were weighed on their own before deposition. After deposition, the samples were dried, removed from the clamp, and weighed on its own. No powder was observed to fall from the coated sample upon removal from the clamp.

Figure 26 shows the relationship between the deposition flux and the wt % Lubrizol 2155 in the dispersion. Each data point represents one sample. The addition of Dolapix leads to a sharp increase in deposition yield up to 2 wt % Dolapix. The deposition yield gradually decreases above 2 wt % Dolapix until a constant yield with respect to dispersant content is achieved. The addition of Lubrizol resulted in an increase in deposition flux across the entire tested range up to 37.5 wt % Lubrizol.

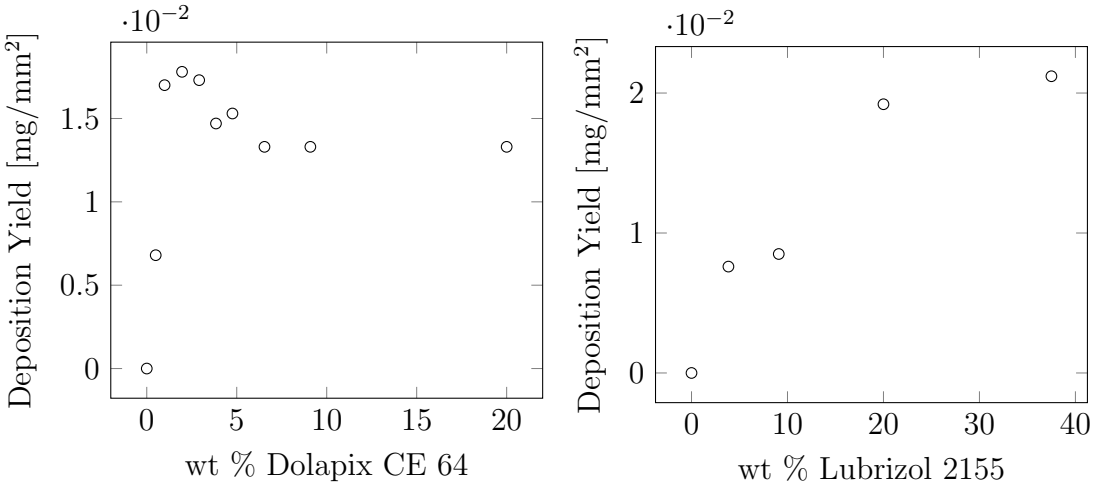

Figure 26: Relationship between h-BN deposition flux and the amount of dispersant added for: (a) Dolapix CE 64 and (b) Lubrizol 2155.

The coatings achieved with Dolapix as dispersant were smooth and even with no apparent defects when viewed under a stereoscope as seen in Figure 27a. Lubrizol did not deliver a uniform coating, as seen in Figure 27b, and therefore was not considered further.

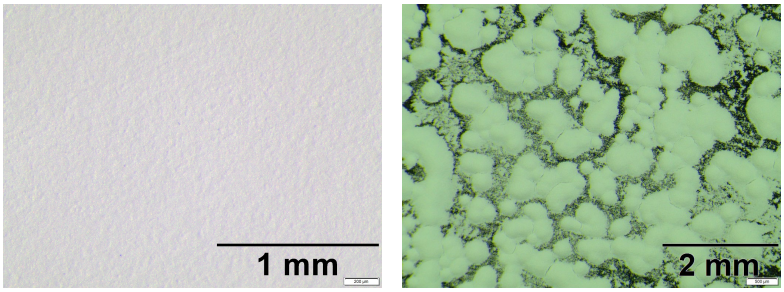

(a) (b)

Figure 27: h-BN coating achieved with dispersant; (a) Dolapix CE 64 and (b) Lubrizol 2155.

Effect of dispersant on Ti_2AlC deposition

Ti_2AlC was deposited onto aluminium foil while varying the content of dispersant in the suspension. Only Dolapix CE64 was considered as dispersant for the deposition of Ti_2AlC as Lubrizol 2155 resulted in uneven coatings for the h-BN

powder. Figure 28 shows the relationship between the deposition flux and the amount of Dolapix CE 64 added to the dispersion. The addition of Dolapix leads to a sharp increase in deposition yield up to 7.4 wt % Dolapix. The deposition yield gradually decreases when the dispersant content exceeds 7.4 wt % Dolapix. The coatings achieved with Dolapix as dispersant were smooth and even with no apparent defects.

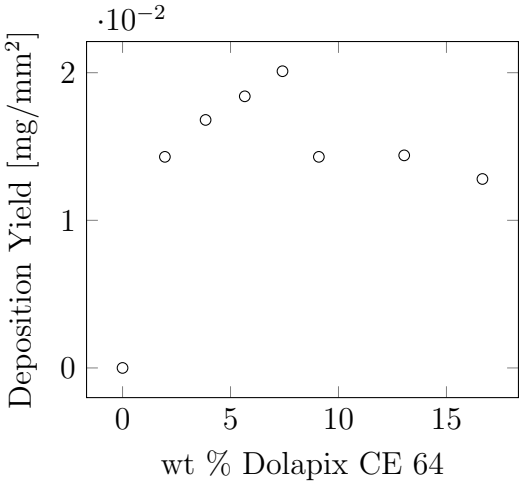

Figure 28: Relationship between Ti_2AlC deposition flux and the amount of dispersant added.

Effect of EPD parameters on h-BN deposition onto carbon fibres

The procedure used to coat carbon fibre samples with h-BN is discussed in section 4.2.2. The results from the dispersant trials were used to achieve the highest possible deposition yield. Dolapix CE 64 was used as dispersant at a 2 wt % addition for h-BN. Low voltages (2-5 V) were used to attempt to create the h-BN interphase on carbon fibres as a very thin coating was required. Figure 29 shows the deposition yield of h-BN, on carbon fibre samples, for different voltages and deposition times.

Figure 30 shows images of carbon fibre coated with h-BN using EPD at 5 V for 5 minutes. Figure 30a shows a stereoscope image of a single fibre bundle, after coating, that was removed from the weave. The regions showing no white h-BN powder are where fibre tows crossed to form the weave. This clearly shows that the h-BN particles are not able to infiltrate throughout the fibre weave during EPD. Figure 30b corroborates the findings of the stereoscope image. It shows a polished cross-sectional view of the coated carbon fibres. It shows a cloudy white region on the outside of the carbon fibre weave which is a layer of h-BN particles.

In addition, it shows that the plate-like h-BN particles could not penetrate beyond the first layer of carbon fibres.

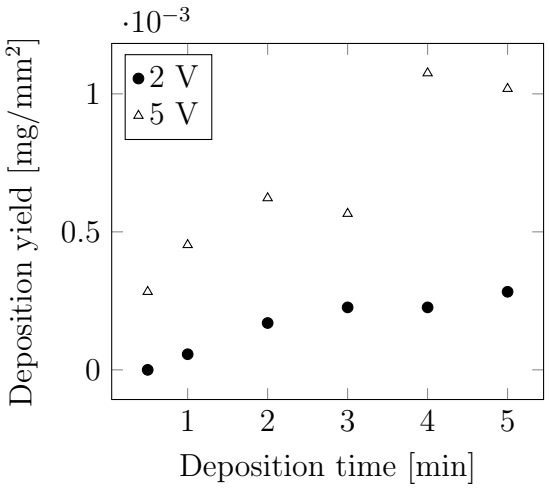

Figure 29: Deposition yield for h-BN powder interphase.

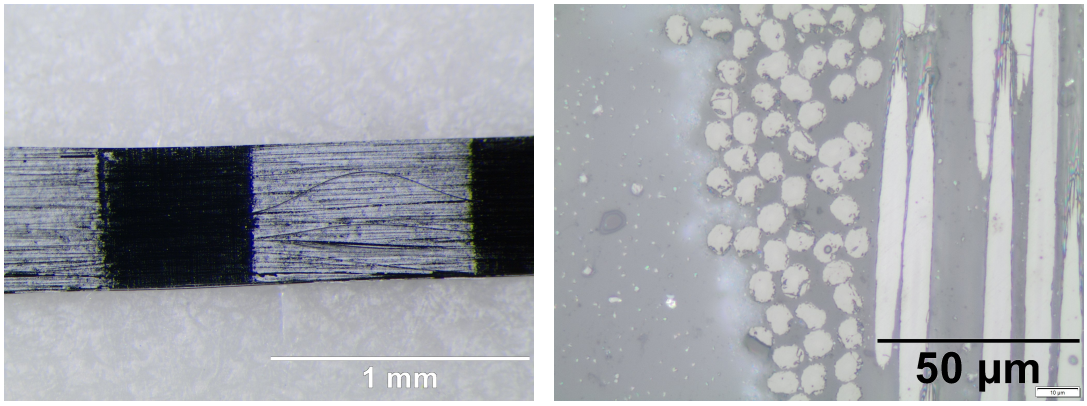

(a) (b)

Figure 30: Stereoscope image of h-BN coated carbon fibres showing (a) fibre tow overlap region and (b) optical micrograph of polished cross-section after EPD at 5 V for 5 minutes.

Effect of EPD parameters on Ti_2AlC deposition onto carbon fibres

The results from the dispersant trials were used to achieve the highest possible deposition yield. Dolapix CE 64 was used as dispersant at a 7.4 wt % addition for Ti_2AlC. Voltages between 20 V and 100 V were used to create the Ti_2AlC

matrix. Figure 31 shows the deposition yield of Ti_2AlC, on carbon fibre samples, for different voltages and deposition times.

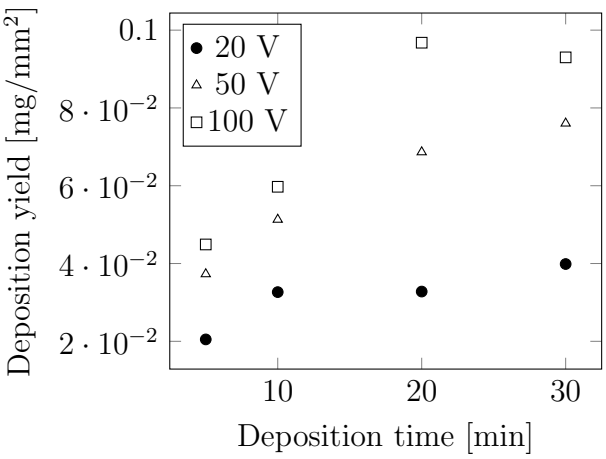

Figure 31: Deposition yield for Ti_2AlC powder matrix.

The surface of the Ti_2AlC coated carbon fibre samples, shown in Figure 32, look similar for the varying EPD voltages tested. The main differences can be seen when the coatings become too thick. The coatings are observed to crack upon drying when they reach a certain level of deposition yield. Figure 32 shows the surfaces of the Ti_2AlC coated samples at increasing levels of deposition yield, corresponding to EPD conditions of, (a) 50 V for 20 min, (b) 50 V for 30 min, (c) 100 V for 20 min, and (d) 100 V for 30 min. The respective deposition yields can be read off Figure 31. The sample coated at 50 V for 20 minutes, as seen in Figure 32a, looks uniform and with no visible defects. The sample coated at 50 V for 30 minutes, as seen in Figure 32b, shows some defects caused by the coating cracking upon drying. The following samples coated at 100 V for 20 and 30 minutes, as seen in Figure 32c and Figure 32d, show extensive damage to the coating. Therefore, the maximum deposition yield that can be achieved without cracking is at approximately 50 V for 20 minutes. Samples coated at lower voltages and shorter durations exhibit correspondingly lower deposition yield with continuous, even coatings.

Figure 33 shows micrographs of the polished cross-sections of a sample coated with Ti_2AlC powder using EPD at 50 V for 20 minutes with the aid of Dolapix CE64 as dispersant. The bright layers on both sides of the fibre sample are the deposited Ti_2AlC powder. The cross-section shows that no Ti_2AlC powder penetrated between individual fibres. The EPD process is therefore not suitable for creating a CMC with continuous fibres as reinforcement.

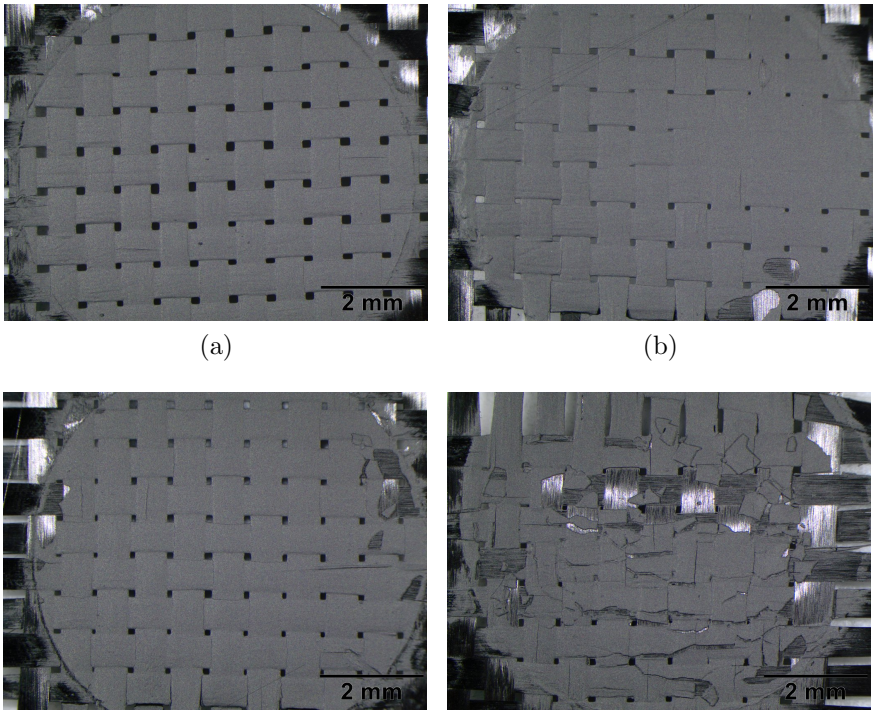

(a) (b)

(c) (d)

Figure 32: Stereoscope images of Ti_2AlC powder deposited on carbon fibres using EPD: (a) 50 V, 20 minutes, (b) 50 V, 30 minutes, (c) 100 V, 20 minutes, (d) 100 V, 30 minutes.

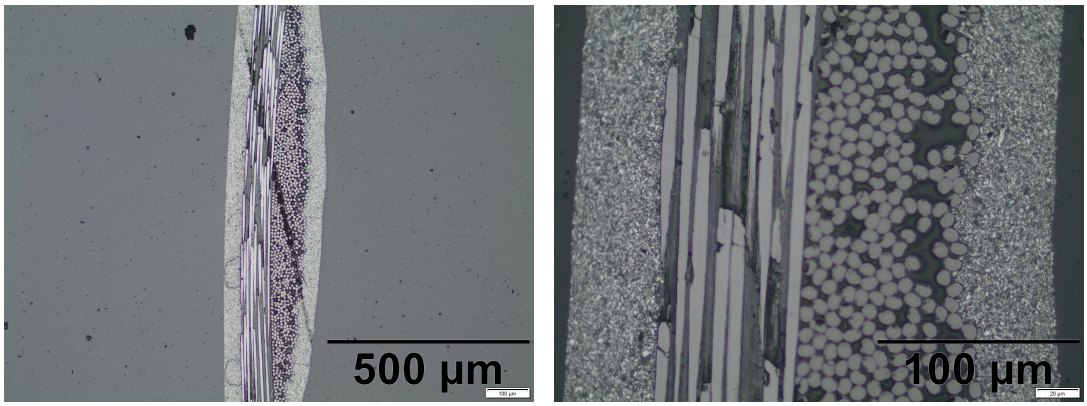

(a) (b)

Figure 33: Optical micrographs, at (a) low and (b) high magnification, showing polished cross-section of Ti_2AlC powder deposited on carbon fibres using EPD at 50 V for 20 minutes.

5.3.2 Vacuum Infiltration

Vacuum infiltration experiments were performed with h-BN powder, as interphase material, and Ti_2AlC powder as matrix material. Figure 34 shows polished cross-sections of carbon fibre samples infiltrated with h-BN powder. Interestingly, Figure 34a shows how the interphase was intended to act within the consolidated CMC, acting as a mechanical fuse to deflect cracks around carbon fibres. Unfortunately the infiltration was largely unsuccessful. The h-BN coating was sparse and irregular. Figure 34b shows a cloudy white region where h-BN particles gathered. Vacuum infiltration of a h-BN interphase has the same flaw as the EPD process. The plate-like h-BN particles have difficulty penetrating between carbon fibres.

Vacuum infiltration was performed with low solids loaded slurries of Ti_2AlC powder suspended in acetone. The infiltration was performed for multiple vacuum cycles. The infiltration yield, for 2.5 vol % and 5,vol % slurries, for multiple infiltration cycles are shown in Figure 35. The samples were weighed before infiltration, dried, and weighed after infiltration again. The yield was calculated as:

$$yield_{vac} = \frac{m_f - m_i}{m_i} \times 100\% \tag{13}$$

where m_i is the mass of the sample before infiltration and m_f is the mass of the sample after infiltration.

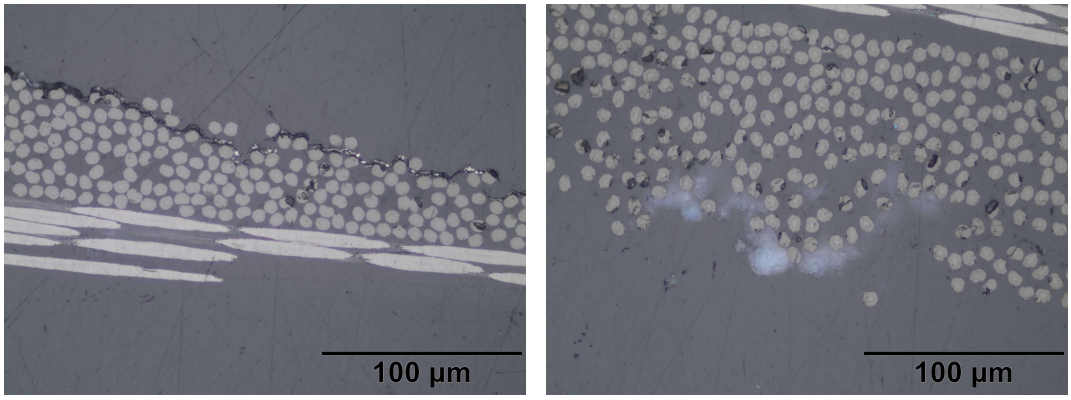

(a) (b)

Figure 34: Optical micrographs showing polished cross-section of a carbon fibre sample infiltrated with h-BN powder using vacuum infiltration with: (a) showing a crack between the epoxy resin of the metallographic mount and the fibre weave along the plane of the h-BN layer and (b) showing a cloudy white region on the periphery of the carbon fibre weave with little penetration into the fibre weave.

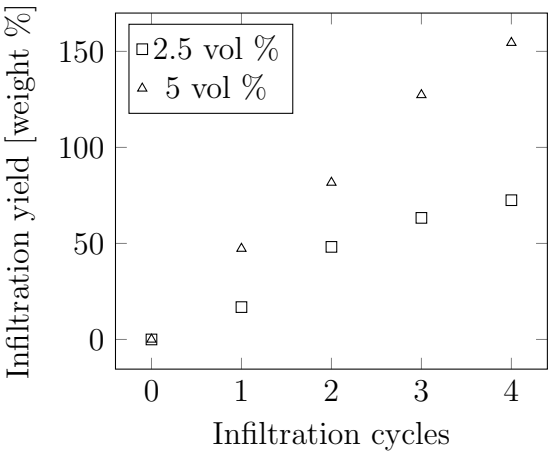

Figure 35: Infiltration yield for low solids loading vacuum infiltration of Ti_2AlC in acetone slurry.

Figure 36 shows a polished cross-section of a carbon fibre sample that underwent 4 vacuum infiltration cycles with a 5,vol % Ti_2AlC slurry in acetone. It shows an irregular coating on the outside of the sample and few particles within the fibre bundles. Observing that multiple vacuum cycles have not resulted in the MAX phase powder infiltrating deeper into the fibre bundles, and that the Ti_2AlC powder sits as a coating layer on the surfaces of the carbon fibre weave, leads to the conclusion that the linear increase in yield with infiltration cycles is due to particle sedimentation in the slurry.

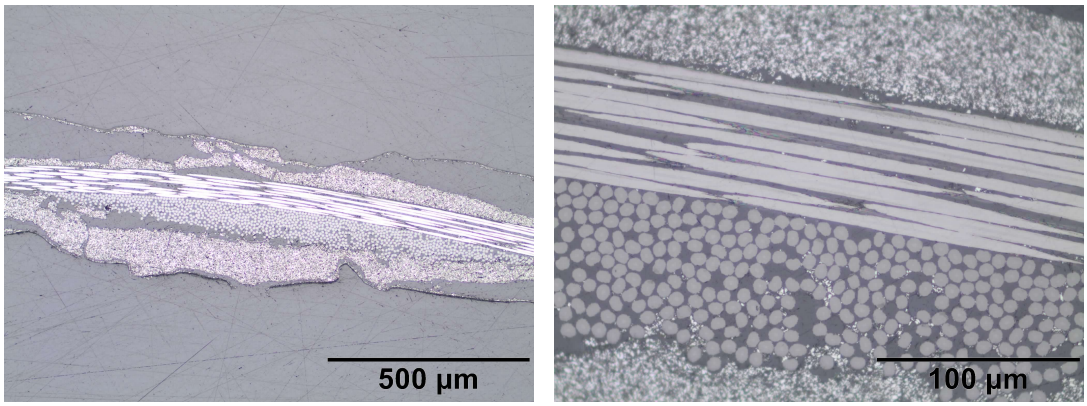

(a) (b)

Figure 36: Optical micrographs showing a polished cross-section of a carbon fibre sample after 4 vacuum infiltration cycles of 5 vol % solids loading Ti_2AlC in acetone slurry.

Figure 37 shows a polished cross-section of a carbon fibre sample that underwent 2 vacuum infiltration cycles with a 30 vol % Ti_2AlC slurry in distilled water. Where distilled water was used for the liquid medium, the fibre samples were not sonicated in acetone before processing as this proved to decrease the wettability of the fibres by distilled water. This was observed by viewing the sample through a stereoscope and introducing a drop of distilled water to the fibre sample. Only small discrete bright spots can be seen between the fibres where powder particles managed to infiltrate the weave. This degree of infiltration is insufficient for the purpose of creating a continuous matrix phase of Ti_2AlC.

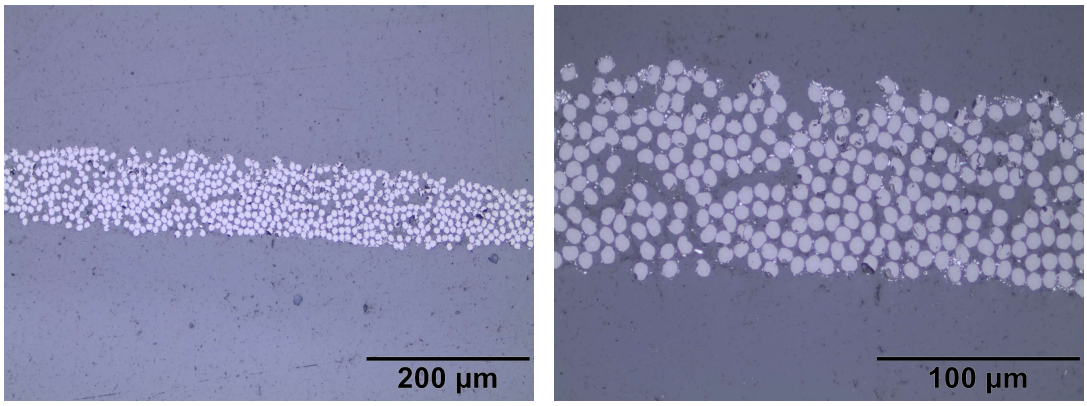

(a) (b)

Figure 37: Optical microscope images showing polished cross-section of a carbon fibre sample after 2 vacuum infiltration cycles with 30 vol % Ti_2AlC in distilled water slurry.

5.3.3 Pressure Infiltration

Pressure infiltration experiments were performed with h-BN powder, as interphase material, and Ti_2AlC powder as matrix material. The infiltration of h-BN powder yielded similar results to the other methods, namely, EPD and vacuum infiltration. The plate-like h-BN particles have difficulty infiltrating the fibre bundles in sufficient quantities to effectively create an interphase for the CMC. Additionally, it limits the effectiveness of infiltrating the Ti_2AlC powder in subsequent steps. The box and whisker plot in Figure 38, showing the infiltration yield for the Ti_2AlC powder, shows that the presence of the h-BN powder significantly reduces the effectiveness of the pressure infiltration. The box and whisker plots were generated using data from 25 samples without h-BN interphase and 14 samples with h-BN interphase.

Figure 39 shows polished cross-sections of a sample infiltrated with Ti_2AlC powder using pressure infiltration. The bright spots, being the infiltrated powder particles, can be seen throughout the fibre bundles. The cross section shows that significant amounts of Ti_2AlC powder penetrated between individual fibres while using only two pressure infiltration cycles. Processing was stopped after two cycles of pressure infiltration to limit the extent of the damage to the fibres caused by processing. Excessive handling of the fibre samples increases the risk of distorting the weave or damaging the fibres. Pressure infiltration was used as the infiltration method to create samples for SPS. The volume fractions for the CMC prepreg samples are calculated and compared to that of the consolidated CMC in section 5.4.2.

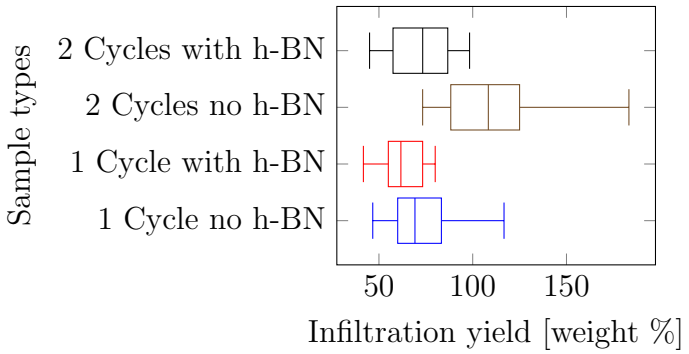

Figure 38: Box and whisker plot showing the Ti_2AlC powder infiltration yield for the samples with and without the previous infiltration of h-BN particles as interphase.

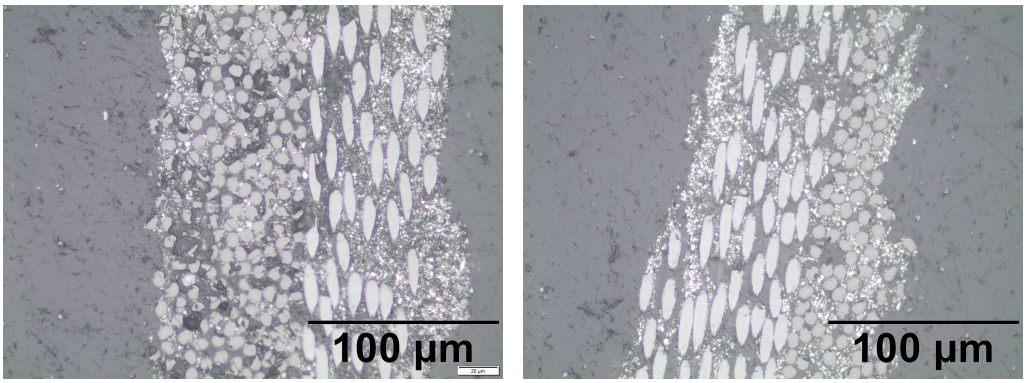

(a) (b)

Figure 39: Optical microscope images showing polished cross-section of a carbon fibre sample infiltrated with Ti_2AlC powder using two cycles of pressure infiltration.

5.4 Phase 3: CMC Consolidation by SPS

Following consolidation, the CMC discs were characterised by volume fraction calculations, density analysis, CT-scanning, ball on three balls (B3B) strength testing, optical microscopy, nano-CT, SEM, and EDS as outlined in section 4.4.3. The results of the consolidation process and the characterisation are presented herein.

5.4.1 Sintering

CMC prepreg samples were fabricated using two cycles of pressure infiltration, as discussed in section 4.2.2, to infiltrate Ti_2AlC powder into the fibre weave. Eight of these were combined in a 0°-90° configuration before sintering. The CMC prepreg discs were then sintered using SPS, as discussed in section 4.2.3, to form a single consolidated disc of 8 layers. Pure Ti_2AlC discs without any reinforcements were also sintered using SPS for strength comparisons.

Figure 40 and Figure 41 show the sintering parameters, with respect to time, for the sintering of the pure Ti_2AlC disc and the CMC disc, respectively. The temperature and force profiles are shown mainly so that their effect on the ram displacement profile can be explained. The different stages of the process are shown on the ram displacement curve.

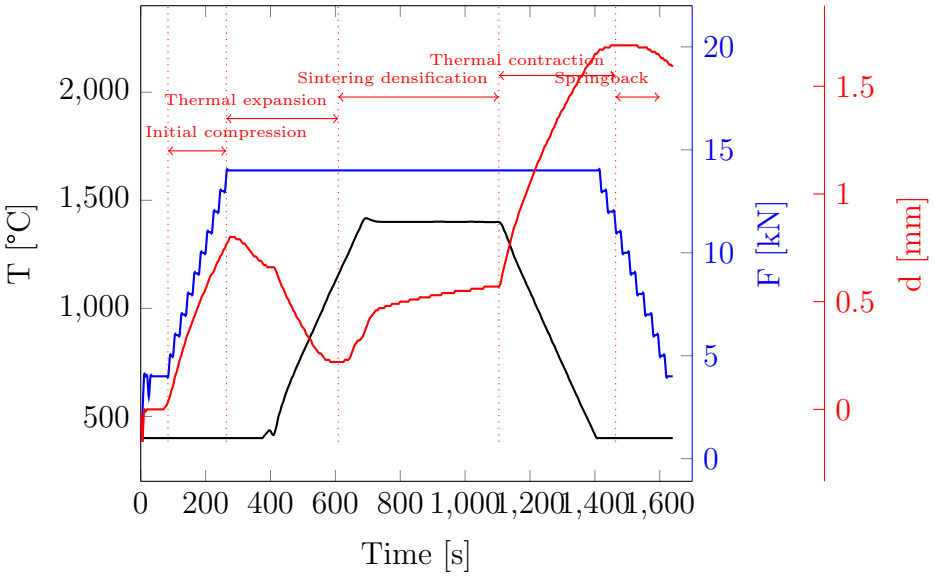

Figure 40: SPS parameters during sintering of the Ti_2AlC disc with T: temperature, F: force, and d: ram displacement.

Initial compression, beginning as the force is applied and ending as soon as the maximum load is reached, occurs as the Ti_2AlC powder is compressed by the ram. Throughout this process, the graphite die expands as it is heated. During initial compression, the densification of the sample by load application dominates over thermal expansion. Once the maximum required load is reached, corresponding to a pressure of 20 kN, further compression of the sample stops and the ram displacement is dominated by the thermal expansion of the Ti_2AlC disc as well as the graphite punches. The majority of the sintering is shown in the region between die expansion and contraction. At about 600 s, 1200 °C, the onset of sintering shrinkage occurs with the thermal expansion and sintering shrinkage initially balancing each other out (point of inflection on ram displacement curve). As the temperature increase further, the sintering rate increase with the sintering shrinkage dominating the behaviour, resulting in densification of the Ti_2AlC disc. Sintering densification of the MAX phase powder into a consolidated matrix continues at a reduced rate since the temperature is held constant at 1400 °C. After the 7 minute dwell time at 1400 °C, the temperature of the sample is gradually decreased. This results in thermal contraction of the sample that dominates over further sintering shrinkage. The rate of sintering shrinkage is continuously decreasing as the sample densifies and the temperature drops, resulting in the nonlinear contraction observed. Finally, as the load is removed from the sample starting at 1450 s, the elastic compression of the sample and graphite punches are recovering, resulting in a small degree of expansion. Elastic springback is observed in this final stage.

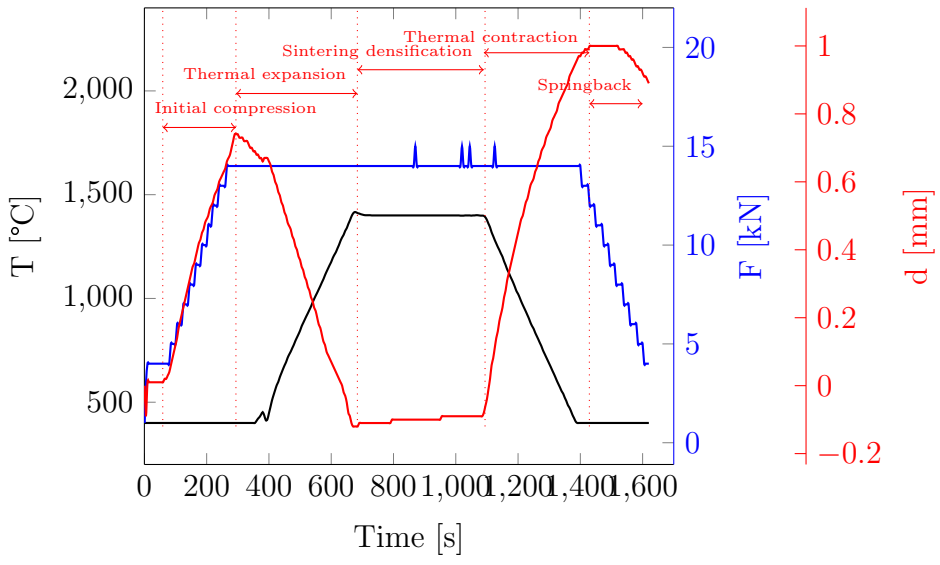

Figure 41: SPS parameters during sintering of the CMC disc with T: temperature, F: force, and d: ram displacement.

The sintering parameter curves for the CMC samples in Figure 41 looks similar to that of the solid Ti_2AlC disc, except that the increase in ram displacement in the sintering region is more subtle. This is due to the CMC samples being thinner and containing less Ti_2AlC powder than the solid discs.

Samples made with h-BN powder interphase could not be sintered as they fell apart after the debinding treatment. The consolidated CMC samples tested were all without the h-BN interphase.

5.4.2 Volume Fraction Calculations

The volume fractions for the CMC prepreg samples as well as the sintered CMC samples were calculated as described in section 4.3.9. This was done to estimate the reduction in pore volume fraction caused by sintering. The results of the volume fraction calculations for the CMC are shown in Table 3. These results are an average of 5 samples (one sample containing 8 layers).

Table 3: Average volume fraction of CMC components for prepreg and sintered samples.

	Fibre [%]	**Matrix** [%]	**Pore**[%]
CMC prepreg	38.2 ± 0.75	18.33 ± 2.3	43.5 ± 1.6
Sintered CMC	48.3 ± 2.1	22.9 ± 2.4	28.8 ± 1.1

5.4.3 Sintered Density

The densities of the pure Ti_2AlC and sintered CMC discs were measured using the Archimedes wet/dry method as discussed in section 4.3.7. The results are summarised in Table 4.

Table 4: Average density results, as measured using the Archimedes wet/dry method, for Ti_2AlC discs and CMC discs.

	Average apparent density [g/cm^3]	**Average open porosity**[%]
Sintered Ti_2AlC	3.96 ± 0.073	0.987 ± 0.66
Sintered CMC	2.04 ± 0.017	16.3 ± 1.4

The densification parameter, which is a measure of the change in porosity after sintering relative to the change in porosity needed to achieve full density, is ex-

pressed as (German, 1996):

$$\psi = \frac{\rho_s - \rho_g}{\rho_t - \rho_g} \tag{14}$$

where ρ_s is the sintered density, ρ_g is the green density, and ρ_t is the theoretical density. The densification parameter was calculated for the pure Ti_2AlC and the CMC discs to illustrate the constrained sintering effect of the carbon fibre reinforcement on the densification of the Ti_2AlC. The densification parameter for the pure Ti_2AlC and CMC was calculated as 0.94 and 0.57.

5.4.4 Microstructural Characterisation of Sintered CMC

CT scanning was performed to establish similarity between sintered samples. The reconstructed CT images show the more dense Ti_2AlC as a bright phase and the carbon fibres as a darker phase.

Figure 42 shows reconstructed CT images of two sintered CMC samples, produced using pressure infiltration and SPS. Figure 42a shows a typical defect-free samples, while Figure 42b shows a sample that was found to have a large abnormal defect. The defect is caused by a distortion of the weave pattern and most likely occurred during sample fabrication or subsequent sample handling. Of the 5 CMC samples scanned, a single sample showed such abnormal defects. Pores within samples are not deemed abnormal; they are a normal artefact of processing. Only large pores could be identified using CT as the resolution was relatively large (25 μm). Therefore the pores in interfibre spaces are too small to be identified using this method. However, the number and size of pores in the defective sample is significantly more than in the other samples, as shown in Figure 43.

The interpretation of CT data is subjective as the search parameters are adjusted by the user. This means that these results should not be used as a direct measure of porosity, but merely as a method of comparing samples. This can be illustrated by comparing the pores found using relaxed search parameters as shown in Figure 44. The image in Figure 44 can be used, however, to show that the lower density regions align with the fibre directions. Additionally, it can be difficult to distinguish between pores and fibre bundles due to the large density difference between matrix and fibres. The subsequent scanning of a single sample at a higher resolution did not give meaningful results.

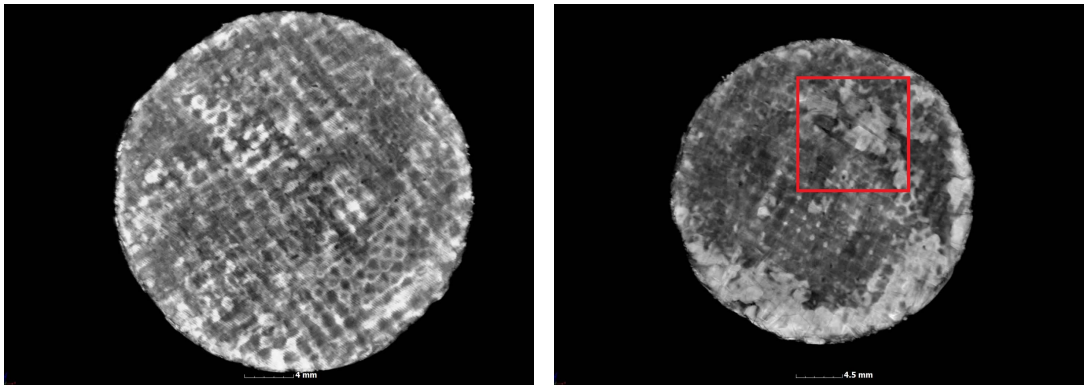

(a) (b)

Figure 42: Reconstructed CT images showing (a) regular abnormal defect-free sample and (b) defective sample with large defect.

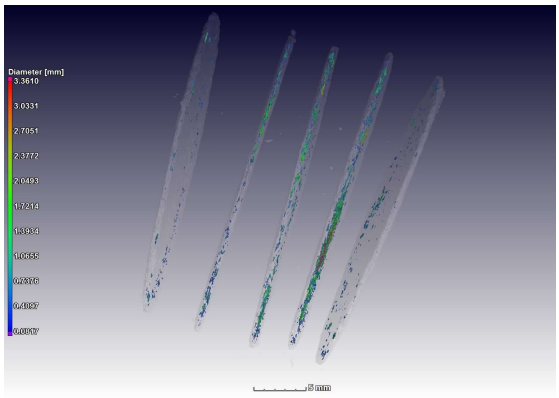

Figure 43: Reconstructed CT images showing large pore spaces (larger than 80 μm) with the defective sample (second from the right) showing significantly more porosity than the others.

A 2 mm sample was cut from a fractured CMC disc for nano-CT scanning. The resolution of the scan is directly related to the volume of the scanned object. Therefore it was important to use a small piece from the CMC disc. Figure 45 shows cross-sectional reconstructed images of the sample from the top and from the side. The nano-CT scanning revealed more detail about the sample volume than the low-resolution CT scanning discussed in section 5.4.4. However, due to the subjective nature of CT data interpretation, no quantitative results could be obtained. The nano-CT reconstruction correlates well with optical microscopy, showing layered regions with a high MAX phase content. The resolution of the

reconstruction was too low to accurately compare areas within fibre bundles to the microscopy results.

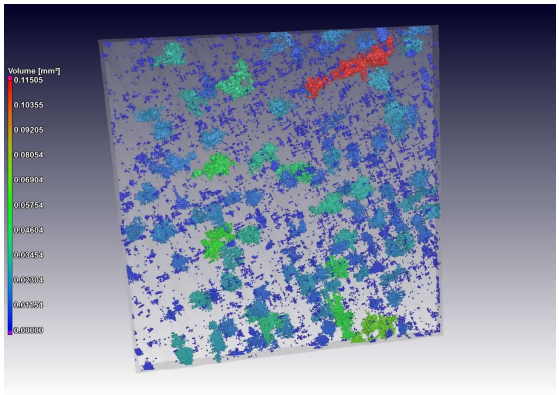

Figure 44: Reconstructed CT image showing the internal porosity, determined using relaxed search parameters, showing that low density regions align with the fibre directions.

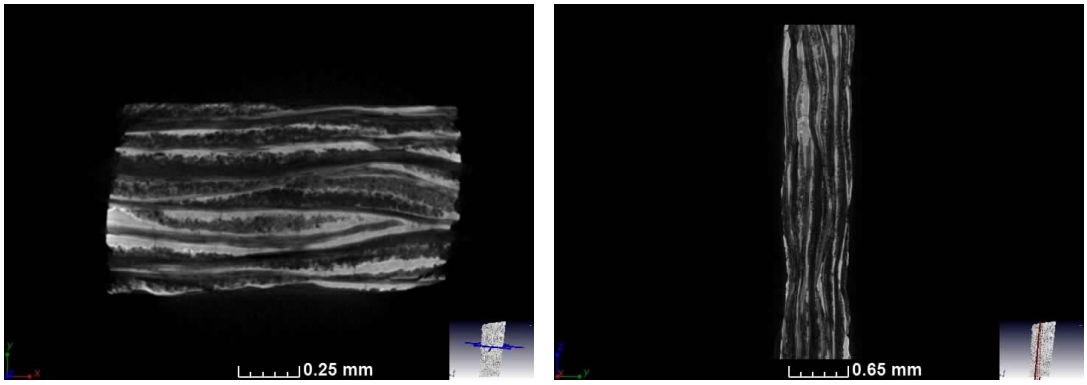

(a) (b)

Figure 45: Reconstructed nano-CT image showing: (a) cross-sectional top view of the sample, (b) cross-sectional side view of the sample.

After the sintered discs were fractured using the B3B test method, they were imaged using optical microscopy. The preparation of the samples for optical microscopy is discussed in section 4.3.2.

The fracture surface of a Ti_2AlC disc is shown in Figure 46a while the side of a fractured CMC disc is shown in Figure 46b. The side of the CMC disc is shown as the samples where still held together by some fibres that did not break during

testing. The optical microscope cannot achieve the magnification necessary to see the fibre/matrix interaction. Polished cross-sections could be imaged using an inverted metallurgical microscope to show more detail as shown in Figure 47. The MAX phase is not continuous throughout the cross-section of the sample. Additionally, many areas of porosity can be seen as well as cracks through the matrix and fibre bundles.

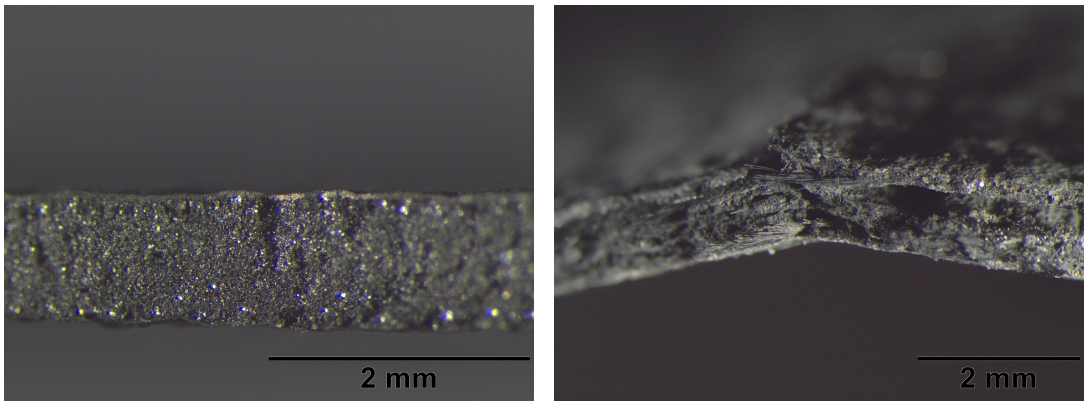

(a) (b)

Figure 46: Stereoscope images showing (a) the fracture surface of a sintered Ti_2AlC disc and (b) the fracture of a sintered CMC disc.

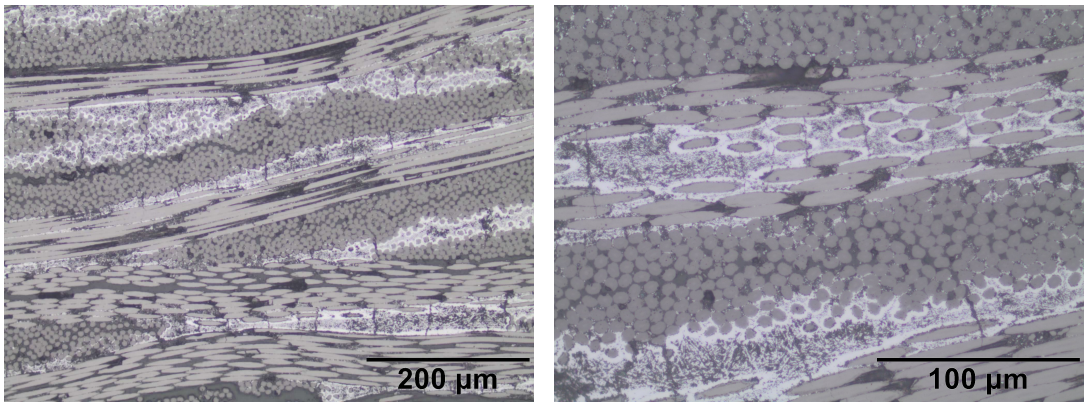

(a) (b)

Figure 47: Optical micrographs of polished cross-section of sintered CMC discs that have been fractured using the B3B test method.

SEM analysis, as discussed in section 4.3.3, was conducted on a polished cross section of the CMC disc after fracture as well as on the failure surface of the

CMC disc. Backscattered electron (BSE) analysis was used for the polished cross-section so that the composition of the CMC could be observed. BSE-SEM shows different phases present at a different brightness as heavier elements backscatter elements more strongly. This allows for the distinction between matrix and fibres on the cross-section. Secondary electron (SE) analysis was used for the fracture surface of the CMC disc so that the topography could be observed.

Figure 48a shows BSE-SEM micrographs of the polished cross-section in a region representative of the infiltrated fibre tows. The BSE-SEM micrographs show the matrix material clearer than the optical micrographs. Figure 48b shows a region in the CMC where cracks are deflected by the carbon fibres. This shows that the carbon fibre reinforcements perform as intended even though there was no interphase present. The B3B test did not necessarily cause the cracks as they were observed in samples that have not been fractured. The cracks most likely occurred during the constrained sintering. A few problems were observed in the CMC. Firstly, areas of the matrix was observed to not be fully densified as shown in Figure 49a. Additionally, Figure 49b shows an extreme case of fibre damage due to the sintering procedure. Elements from the matrix diffused into the carbon fibre causing noticeable change in the appearance of the fibre. This is investigated and discussed further in section 5.4.5.

The incomplete densification can be improved by increasing the sintering duration. This can, however, lead to the formation of excess TiC in the CMC leading to unintended material properties. The increase of sintering time will also increase the damage to the fibres caused by diffusion of elements from the matrix into the carbon fibres unless a suitable interphase is used. The h-BN powder interphase would not have solved this problem as it would not have covered the fibres completely and therefore there would still be damage to the fibres. In the tested samples it is possible that the amount of Ti_2AlC particles infiltrated into the carbon fibre reinforcement was too few to allow full densification for this specific constrained sintering problem. Therefore a better way to improve densification is by increasing the amount, and the uniformity, of Ti_2AlC particles infiltrated into the carbon fibre reinforcement.

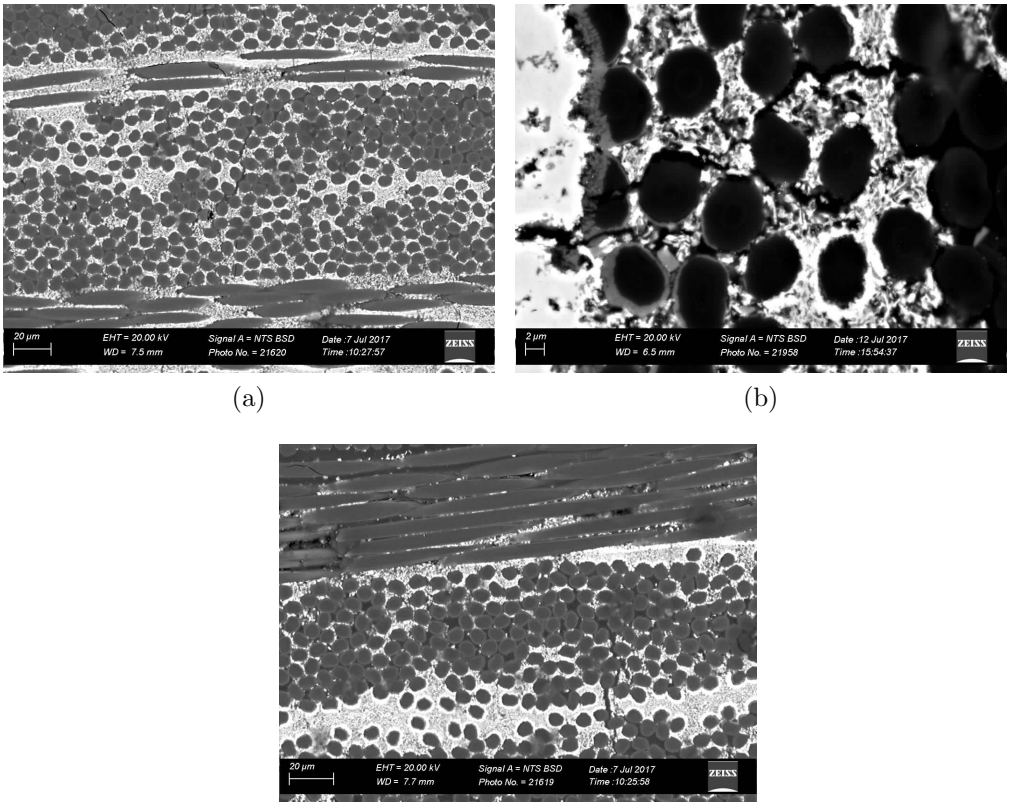

(a) (b)

(c)

Figure 48: BSE-SEM micrograph of the CMC after fracture showing: (a) consolidated matrix within fibre tow, (b) cracks deflected by fibres, and (c) absence of matrix material in regions of fibre bundle caused by improper infiltration.

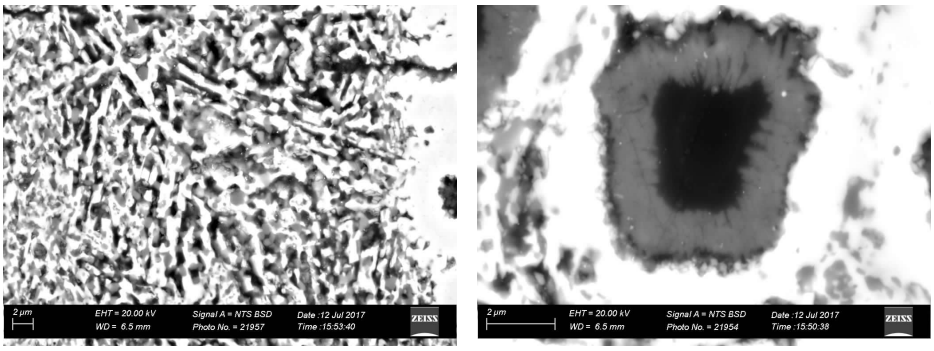

(a) (b)

Figure 49: BSE-SEM micrograph of the CMC after fracture showing: (a) matrix region not fully densified, (b) carbon fibre in matrix-rich area.

5.4.5 Elemental Analysis of Sintered CMC

EDS analysis was conducted on the polished cross-section of the CMC sample as outlined in section 4.3.4. The interaction of the matrix and the fibres during sintering was of particular importance. EDS mapping was used to identify the dominating elements in the various regions of the CMC. Following EDS mapping, a quantitative analysis was performed.

As discussed in section 5.4.4, regions could be identified in the CMC sample where the fibres and matrix clearly interacted during sintering. This could be seen in individual fibres where different areas of brightness, as seen by BSE-SEM, could be identified in a concentric pattern. Only a fraction of fibres showed a noticeable change after sintering. Figure 50 shows a BSE-SEM micrograph, of a region where no interaction between fibres and matrix could be seen, along with the associated EDS maps for Ti, Al, and C. The maps indicate that no titanium has diffused into the carbon fibres and that the carbon concentration is higher in the fibres than in the matrix as expected. Interestingly, it shows that some aluminium did diffuse into carbon fibres even though no noticeable physical changes could be observed to the fibres. The aluminium concentration in the matrix was shown to be higher than in the fibres as expected.

Figure 51 shows a BSE-SEM micrograph, of a region where noticeable interaction between fibres and matrix could be seen, along with the associated EDS maps for Ti, Al, and C. The majority of the matrix and the dark inside region of the carbon fibres remain largely unchanged. The bright region surrounding the affected fibres shows high titanium concentrations and low aluminium concentrations while the grey region on the outside edges of the affected fibres shows the opposite. This confirms that aluminium diffused into the carbon fibres during sintering.

The quantitative analysis confirmed the results of the EDS mapping. Figure 52 shows a BSE-SEM micrograph along with an EDS line scan of the affected regions. The line scan confirms high titanium concentration in the bright region surrounding affected fibres and high aluminium concentration in the grey region within the fibres. Figure 53 shows the results of single point scans performed at the different regions as indicated in Figure 52. The results shown for carbon are much too high in the regions outside of the fibre. It is difficult to detect accurate amounts of low level elements, especially carbon, using EDS. It does, however, indicate that the carbon content decreases steadily as the analysis site moves away from the fibre centre.

For areas within the CMC where diffusion occurred between the fibres and matrix, the combined results of the EDS mapping, line scan, and point scans confirm the following:

- The centre of the fibre consists mainly of C, showing some Al diffusion.
- The diffusion affected region within the fibre consists of C and Al, most likely forming aluminium carbide (Al_4C_3).
- The diffusion affected region in the matrix, surrounding the fibre, consists of Ti and C, most likely forming titanium carbide (TiC).
- The majority of the matrix remain unaffected .

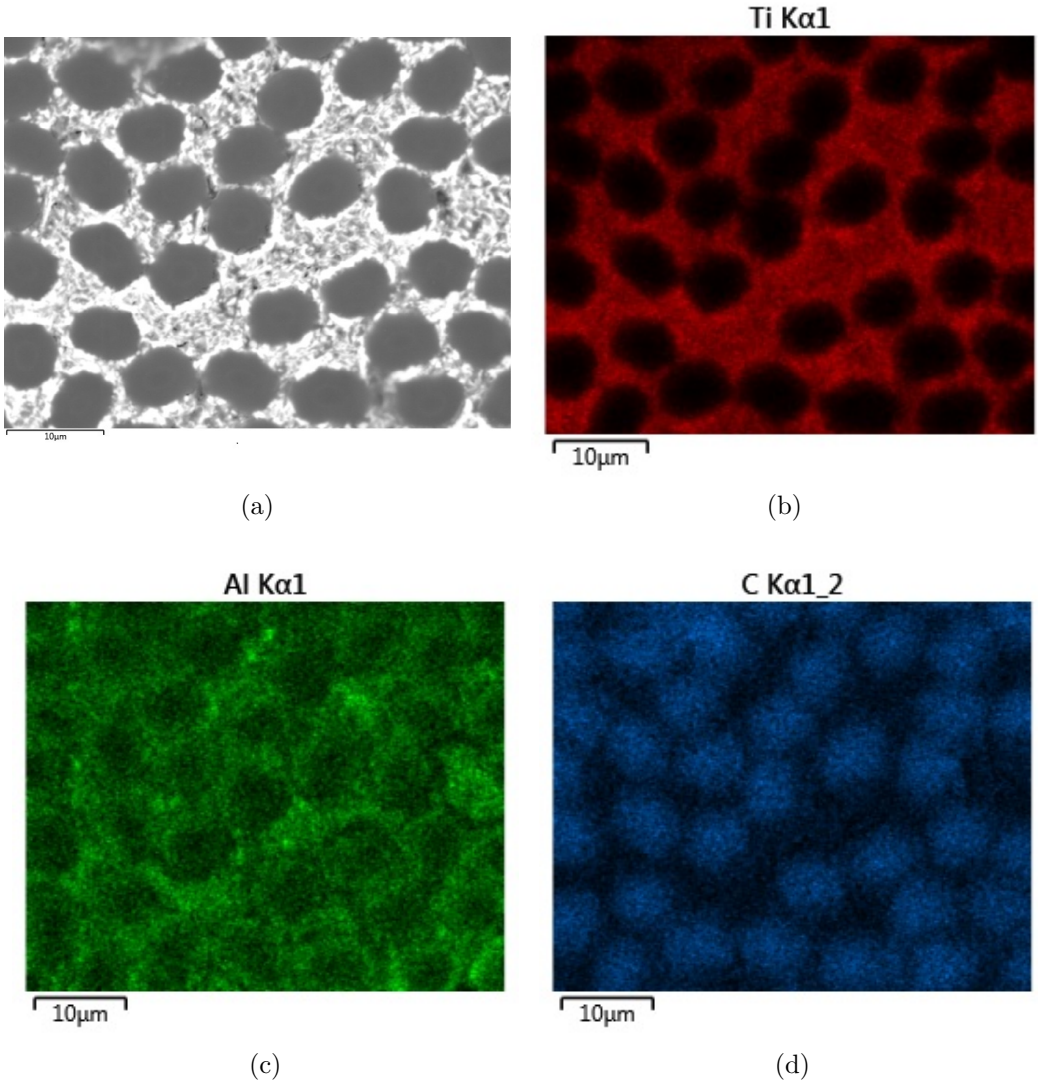

Figure 50: BSE-SEM micrograph (a) of the CMC, showing an area where there is very little diffusion between fibres and matrix, along with EDS maps for (b) Ti, (c) Al, and (d) C.

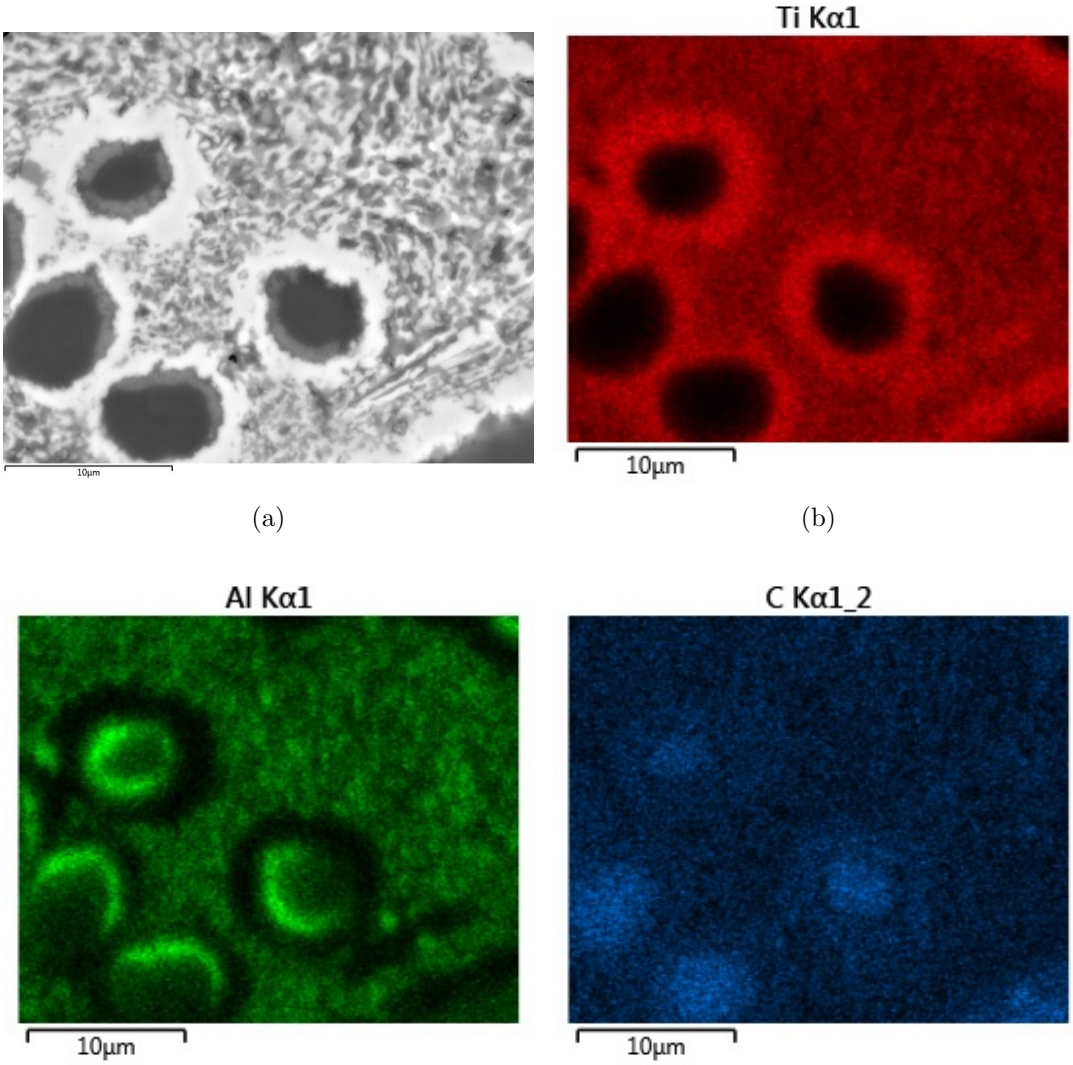

(a) (b)

(c) (d)

Figure 51: BSE-SEM micrograph (a) of the CMC, showing an area where there is significant diffusion between fibres and matrix, along with EDS maps for (b) Ti, (c) Al, and (d)C.

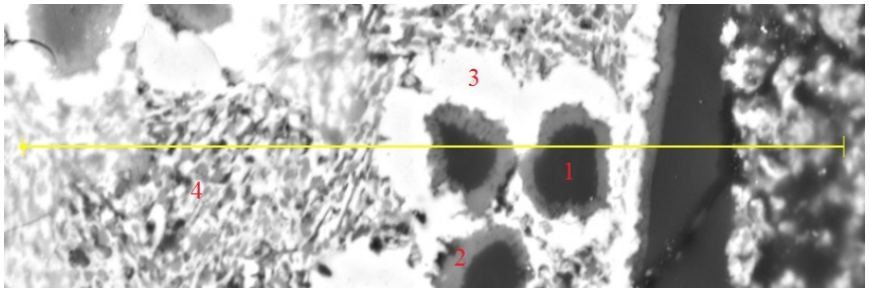

(a)

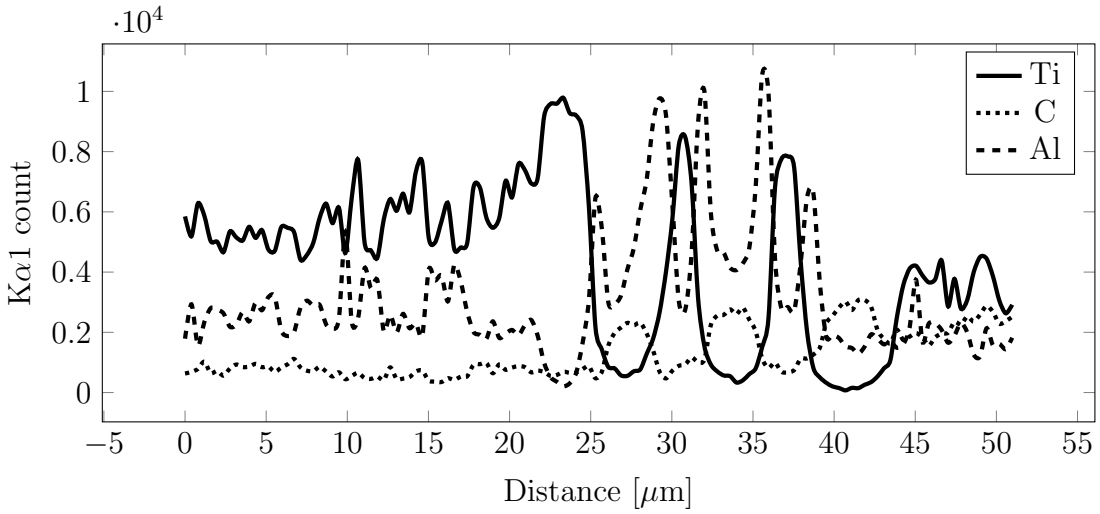

(b)

Figure 52: BSE-SEM micrograph of the CMC with EDS line scan and the locations of the sites for EDS point scans.

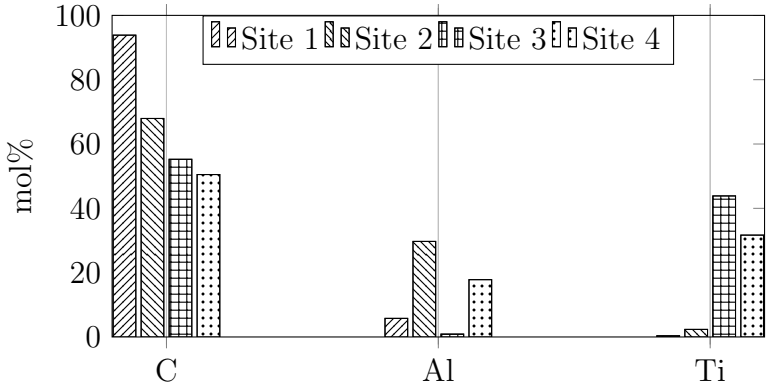

Figure 53: Quantitative results of EDS point scans at the different sites as indicated on the BSE-SEM image in Figure 52.

5.4.6 Mechanical Testing of Sintered CMC

The 30 mm diameter sintered CMC samples were fractured using the B3B test method discussed in section 4.3.8. The displacement of the centre loading ball and force was measured throughout the duration of the tests.

Figure 54 shows the fractured Ti_2AlC and CMC discs. Failure was initiated in the tensile surface plane opposite the loading ball. The majority of the samples broke into three pieces, but in some cases the samples broke in two. This largely corresponds with finite element analysis work done by Borger et al. (2002) that showed a threefold symmetrical tensile stress field with the B3B test configuration. Even the samples that broke into two pieces, fractured along the high tensile stress locations. More details on the samples are given in Appendix D.

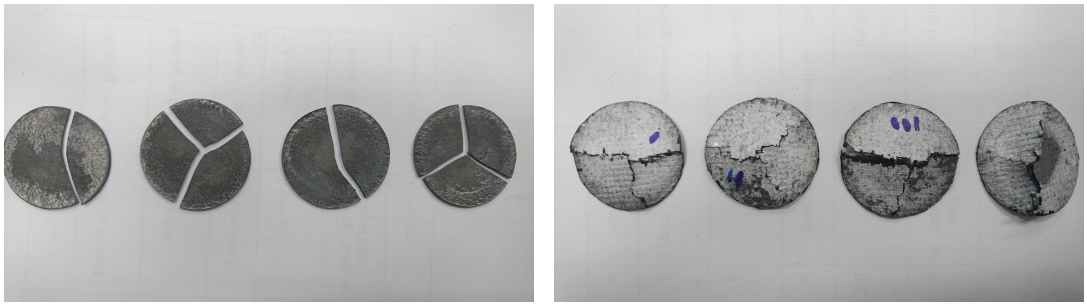

(a) (b)

Figure 54: Sintered discs fractured using the B3B test configuration (a) sintered pure Ti_2AlC discs and (b) sintered CMC discs.

The maximum tensile stress in the disc was calculated as a function of the applied load, according to equation 9. Figure 55 and Figure 56 show the corresponding stress-displacement curves for the pure Ti_2AlC and CMC discs, respectively. The stress-displacement curve for the pure Ti_2AlC discs shows the typical steep incline associated with monolithic ceramics. The fracture is sudden and without warning. Following fracture, the load immediately drops to zero (not shown in Figure 55). The curves for samples 2 and 3 show a brief drop in load followed by an increase in load. This shows some resistance to fracture on the part of the monolithic discs as this was most likely caused by the formation of a crack. It was interesting to note that Ti_2AlC sample number 1 had the lowest stiffness and fracture strength. This was due to a geometric flaw in the sample. The sample did not have a constant thickness throughout, which can be seen in the way the sample fractured in Figure 54a on the far left. Ignoring the sample with the geometric flaw, the

sintered Ti_2AlC discs fractured at stresses between 430 MPa and 500 MPa and at displacements between 0.155 mm and 0.185 mm.

The stress displacement curves for CMC samples 1, 3, and 4 show similar results. CMC sample number 2 shows significantly lower stiffness and strength values; sample number 2 was identified to have an abnormal defect using CT-scanning as shown in Figure 42 and Figure 43. This result indicates that internal defects have an effect on strength and stiffness.

The curves show multiple sharp peaks and sudden drops in load followed by an increase in load. The behaviour of the CMC tested resembles the typical behaviour as discussed in section 3.1 and shown in Figure 7. An example is when the load drops momentarily, due to a crack forming, and subsequently the load increases after the crack is arrested by the fibre reinforcement. However, the high porosity in the tested CMC discs led to many sites for cracks to originate from and therefore the load fluctuates more often in this case. The typical data for the the sintered CMC discs showed ultimate stresses between 112 MPa and 125 MPa. The data for the defective sample (sample 2) showed lower stiffness and ultimate stress (72 MPa). The tests were stopped after the displacements exceeded 2.6 mm as the supporting and loading balls began to touch at some point after this and the results thereafter would be useless.

The stress-displacement curve for one of the samples is shown alone in Figure 57 along with an indication of the three behavioural regions of the curve. The behaviour of a typical CMC is discussed in section 3.1. The first region is simply the linear elastic region where the load is shared by the matrix and the fibres. The second region is where cracking occurs in the matrix material. The stress in this region fluctuates as cracks form and are arrested by fibre reinforcements. The third region is where the CMC starts to fail by fibre pullout and delaminations, indicated by sharp drops in load.

The sintered CMC had lower stiffness and strength than the pure Ti_2AlC. The stiffness of the sintered CMC is approximately 20 times lower than the stiffness of the pure Ti_2AlC. Similarly, the ultimate strength of the sintered CMC is approximately 4 times lower than that of the pure Ti_2AlC. The high porosity in the sintered CMC and the fibre damage, caused by SPS, are to blame for the low stiffness and strength. The damage tolerant properties of the sintered samples is, however, evident.

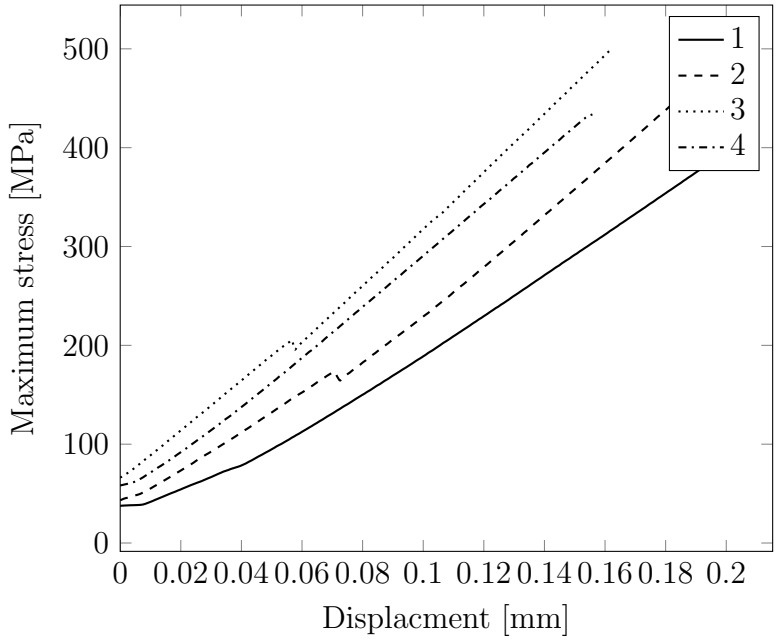

Figure 55: Stress-displacement curve of sintered Ti_2AlC discs fractured using the B3B test method.

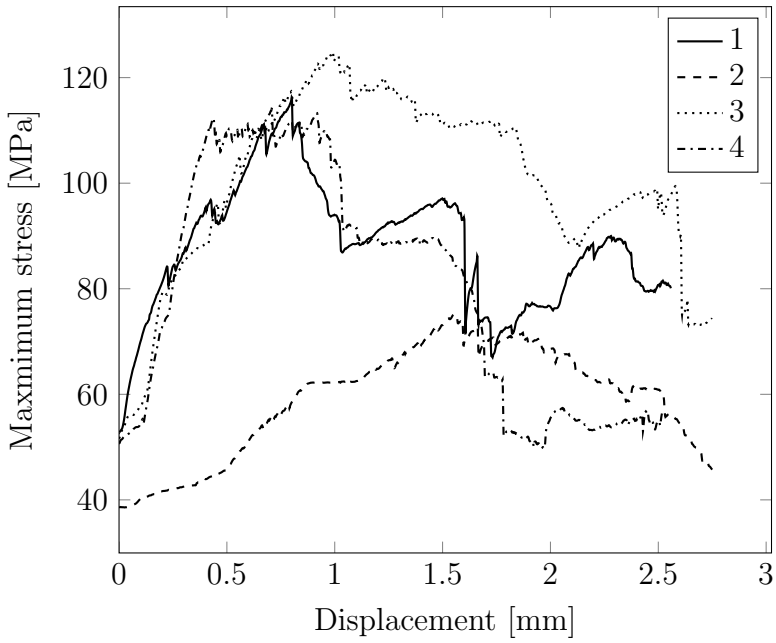

Figure 56: Stress-displacement curve of sintered CMC discs fractured using the B3B test method.

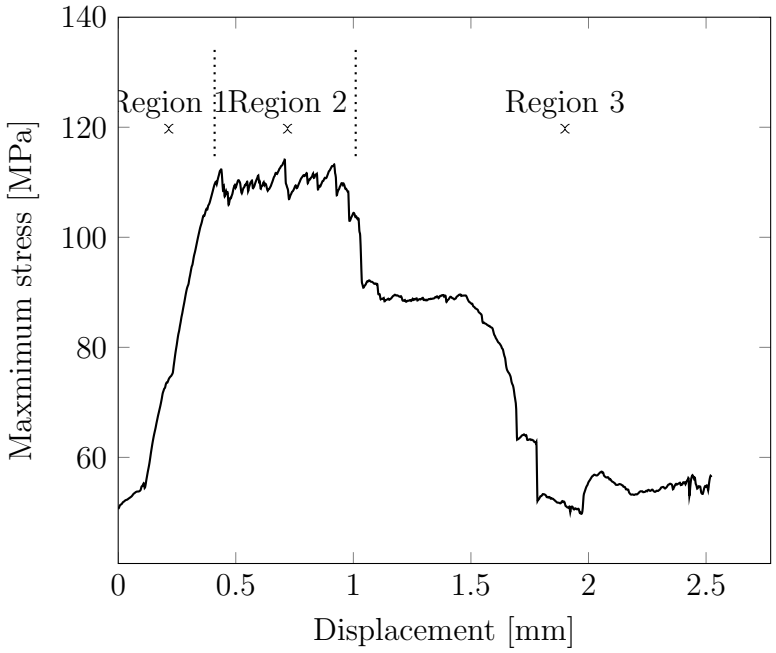

Figure 57: Stress-displacement curve of sintered CMC disc number 4 fractured using the B3B test method with three regions of CMC behaviour indicated.

5.4.7 Fracture Surface Analysis

Figure 58 shows the failure surface of a sintered CMC disc after fracturing using the B3B test method. The fibre pullout shown further illustrates that the fibre reinforcement performs as intended. The pullout of fibres dissipate energy during deformation leading to relatively graceful failure when compared to the abrupt brittle failure of monolithic ceramics. This along with the crack deflection, as illustrated in Figure 48b, leads to a tougher material. Figure 59 shows a fibre connected to a fragment of consolidated Ti_2AlC matrix that clearly shows pullout sites where fibres were before fracturing. This illustrates that multiple fibre pullout and single fibre pullout may be occurring concurrently during deformation. Fibres bonded too strongly to the matrix, caused by diffusion of matrix elements into the fibres as shown in Figure 49b, may not be able to deflect cracks or pullout from the matrix during deformation. Therefore it is important to limit these occurrences by carefully controlling the processing parameters and applying a suitable continuous interphase to the fibre reinforcements.

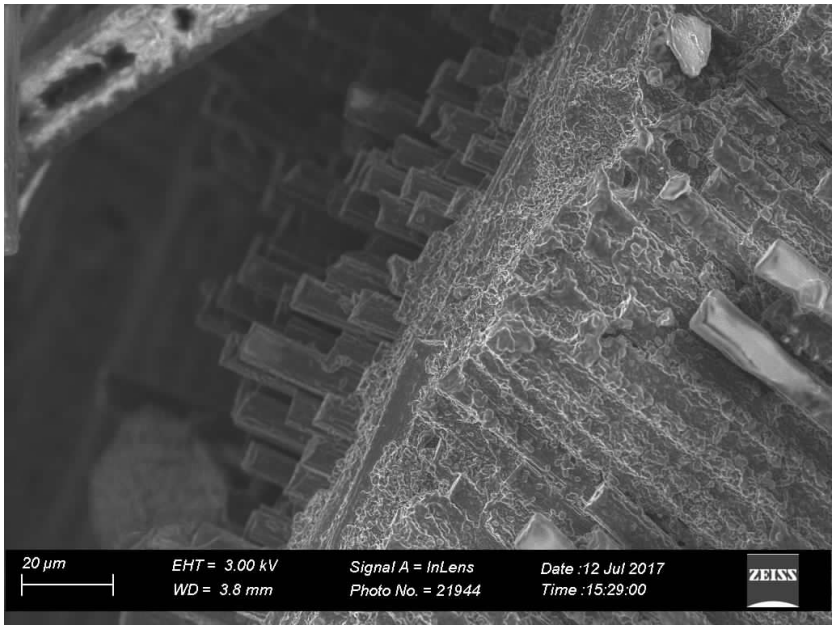

Figure 58: SE-SEM micrograph of the fracture surface of the CMC fractured by the B3B test method showing fibre pullout and fracture.

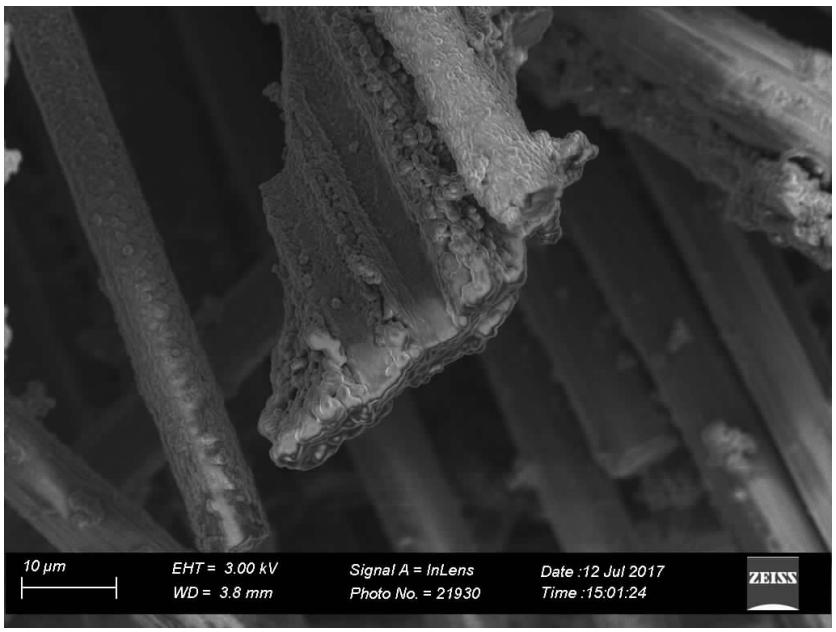

Figure 59: SE-SEM micrograph of the fracture surface of the CMC fractured by the B3B test method showing pullout sites where fibres used to be in the consolidated matrix.

6 Conclusions and Recommendations

A ceramic matrix composite (CMC), containing a MAX phase matrix, was designed and produced with the aim of being suitable for use in high temperature structural applications. Additionally, the CMC was produced in the form of a flexible, robust prepreg. The CMC prepreg layers were combined and sintered, using spark plasma sintering (SPS), to form a densified CMC part. The microstructure, elemental composition, and mechanical behaviour was evaluated. Characterisation of the refractory properties of the CMC was beyond the scope of this project.

The CMC prepreg was designed to be produced by using powder processing methods and avoiding expensive, time-consuming methods such as chemical vapour infiltration (CVI). The designed CMC makes use of carbon fibre reinforcement, Ti_2AlC as matrix, and h-BN powder as a discontinuous interphase to weaken the bond between fibres and matrix. Polymethyl methacrylate (PMMA) was used to coat the prepreg to ensure that it can be handled, cut, and shaped before sintering.

The particle size distribution of the as-received Ti_2AlC powder was altered by attrition milling in a liquid medium. The mean particle size reduced sufficiently to allow infiltration of the powder into carbon fibre bundles within a weave. Additionally, the attrition milling increased the packing density of the powder by altering the particle size distribution form unimodal. The attrition milling did not cause the formation of additional phases in the Ti_2AlC powder, however, it did lead to significant contamination caused by the Al_2O_3 milling beads.

Electrophoretic deposition (EPD), vacuum infiltration, and pressure infiltration were evaluated for producing the CMC prepreg. These methods were used for infiltrating h-BN powder and infiltrating milled Ti_2AlC powder into a carbon fibre weave to form a powder interphase and a powder matrix, respectively. None of the methods succeeded in infiltrating sufficient amounts of h-BN powder to form the powder interphase. The particle size of the h-BN particles and the plate-like shape meant that they could not penetrate the fibre bundles in sufficient amounts. Additionally, the infiltration of the h-BN powder decreased the efficiency of the subsequent Ti_2AlC powder infiltration. EPD of milled Ti_2AlC powder resulted in no infiltration. It did, however, succeed in depositing even coatings on the outside surfaces of the carbon fibre weave. Vacuum infiltration did not succeed in infiltrating sufficient amounts of milled Ti_2AlC powder into carbon fibre bundles to allow densification by SPS. Pressure infiltration was the only method to succeed in infiltrating significant amounts of milled Ti_2AlC powder into carbon fibre bundles.

CMC prepreg layers were combined and sintered, using SPS, to form a coherent CMC part. Microstructural characterisation of polished cross-sections of the sintered samples indicated incomplete infiltration in some regions as well as cracking in the matrix caused by the constrained sintering. Cracks were, however, deflected by the fibres, indicating that the bond between fibre and matrix were sufficiently weak even in the absence of an interphase.

Elemental analysis of the sintered CMC indicated that diffusion between carbon fibres and Ti_2AlC matrix did occur during SPS, severely damaging a fraction of the carbon fibre reinforcement. In affected regions, it was found that aluminium diffused from the Ti_2AlC matrix into carbon fibre, most likely leading to the formation of Al_4C_3 on the outside edges of fibre and TiC in the matrix surrounding the fibre.

The mechanical behaviour of the sintered CMC was compared to that of sintered Ti_2AlC. The stiffness and strength of the sintered CMC was low compared to that of the sintered Ti_2AlC. This was due to significant porosity within the sintered CMC as well as the fibre damage caused by diffusion of aluminium from the matrix into the carbon fibres during SPS. The damage tolerance of the sintered CMC was, however, evident in the mechanical behaviour.

Analysis of the fracture surfaces of the sintered CMC revealed that single fibre pullout as well as multiple fibre pullout occurs during fracture.

The work done in this project forms the starting point for producing a CMC, utilising a MAX phase for the matrix, in the form of a flexible, robust prepreg to be sintered using SPS for use in high temperature structural applications. Future work should focus on improving the mechanical properties of the sintered CMC. This can be achieved by decreasing porosity in the sintered CMC and limiting the fibre damage sustained during sintering. Therefore, the recommendations for future work are to improve the effectiveness of infiltrating ceramic particles into fibre bundles and to employ a continuous, inert interphase to avoid diffusion between fibres and matrix during sintering. Additionally, extending the scope to investigate the refractory properties of the sintered CMC would be beneficial as the ultimate aim of the material is to be used in high temperature applications. Further quantitative analyses are also recommended, specifically to determine oxygen contamination and phase composition of the MAX phase powder as well as the resulting sintered CMC.

7 References

Andersson, J. and Hulbert, D. M. (2009). A discussion on the absence of plasma in spark plasma sintering. *Scripta Materialia*, 60:835–838.

Atkinson, H. V. and Davies, S. (2000). Fundamental Aspects of Hot Isostatic Pressing : An Overview. *Metallurgical and Materials Transactions A*, 12(December):2981–3000.

Barsoum, M. (2004). Spherical Nanoindentations and Kink Bands in. *Journal of Materials Research*, 19(04):1139–1148.

Barsoum, M. W. and El-Raghy, T. (1996). Synthesis and Characterization of a Remarkable Ceramic: Ti3SiC2. *Journal of the American Ceramic Society*, 79(7):1953–1956.

Barsoum, M. W. and El-Raghy, T. (2001). The MAX Phases: Unique New Carbide and Nitride Materials. *American Scientist*, 89:334–343.

Barsoum, M. W. and Radovic, M. (2011). Elastic and Mechanical Properties of the MAX Phases. *Annual Review of Materials Research*, 41:195–227.

Barsoum, M. W., Zhen, T., Kalidindi, S. R., Radovic, M., and Murugaiah, A. (2003). Fully reversible, dislocation-based compressive deformation of Ti3SiC2 to 1 GPa. *Nature materials*, 2(2):107–111.

Basu, R. N., Randall, C. a., and Mayo, M. J. (2001). Fabrication of Dense Zirconia Electrolyte Films for Tubular Solid Oxide Fuel Cells by Electrophoretic Deposition. *Journal of the American Ceramic Society*, 84:33–40.

Besmann, T. M., McLaughlin, J. C., and Lin, H. T. (1995). Fabrication of ceramic composites: Forced CVI. *Journal of Nuclear Materials*, 219:31–35.

Besra, L. and Liu, M. (2007). A review on fundamentals and applications of electrophoretic deposition (EPD). *Progress in Materials Science*, 52:1–61.

Borger, A., Supancic, P., and Danzer, R. (2002). The ball on three balls test for strength testing of brittle discs: Stress distribution in the disc. *Journal of the European Ceramic Society*, 22:1425–1436.

Callister, W. D. and Rethwisch, D. G. (2011). *Materials Science and Engineering*. Wiley, Hoboken, NJ, 8th editio edition.

Carbon-Ukraine (2015). Ti2AlC Safety data sheet. Technical Report 4, Carbon Ukraine, Kiev, Ukraine.

Chen, L., Ye, H., and Gogotsi, Y. (2003). Carbothermal Synthesis of Boron Nitride

Coatings on Silicon Carbide. *Journal of American Ceramic Society*, 86(11):1830–1837.

Coble, R. (1970). Diffusion Models for Hot Pressing with Surface Energy and Pressure Effects as Driving Forces. *Journal of Applied Physics*, 41(12):4798–4807.

Danzer, R., Harrer, W., Supancic, P., Lube, T., Wang, Z., and Börger, A. (2007). The Ball on Three Balls Test - Strength and Failure Analysis of Different Materials. *Journal of the European Ceramic Society*, 27(January):1481–1485.

Das, M., Basu, a. K., Ghatak, S., and Joshi, A. G. (2009). Carbothermal synthesis of boron nitride coating on PAN carbon fiber. *Journal of the European Ceramic Society*, 29:2129–2134.

De Jonghe, L. C., Rahaman, M. N., and Hsueh, C. H. (1986). Transient stresses in bimodal during sintering compacts. *Acta Metallurgica*, 34(7):1467–1471.

Dong, S., Wang, Z., Zhou, H., Kan, Y.-M., Zhang, X., Ding, Y., Gao, L., Wu, B., and Hu, J. (2012). Research Progress in SiC-Based Ceramic Matrix Composites. *Journal of the Korean Ceramic Society*, 49(4):295–300.

du Plessis, A., le Roux, S. G., and Guelpa, A. (2016). The CT Scanner Facility at Stellenbosch University : An open access X-ray computed tomography laboratory. *Nuclear Inst. and Methods in Physics Research, B*, 384:42–49.

El-raghy, T., Barsoum, M. W., Zavaliangos, A., and Kalidindi, S. R. (1999). Processing and Mechanical Properties of Ti 3 SiC 2 : II , Effect of Grain Size and Deformation Temperature. *Journal of American Ceramic Society*, 60:2855–2860.

El-Raghy, T., Barsoum, M. W., Zavaliangos, A., and Kalidindi, S. R. (1999). Processing and mechanical properties of Ti<inf>3</inf>SiC<inf>2</inf>: II, Effect of grain size and deformation temperature. *Journal of the American Ceramic Society*, 82(10):2855–2860.

El-Raghy, T., Chakraborty, S., and Barsoum, M. W. (2000). Synthesis and characterization of Hf2PbC, Zr2PbC and M2SnC (M = Ti, Hf, Nb or Zr). *J. Eur. Ceram. Soc.*, 20:2619–2625.

El-Raghy, T., Zavaliangos, A., Barsoum, M. W., and Kalidindi, S. R. (1997). Damage mechanisms around hardness indentations in Ti<inf>3</inf>SiC<inf>2</inf>. *Journal of the American Ceramic Society*, 80(2):513–516.

Engineered Cramer Composites (2015). HT types C fabrics. Technical report, Engineered Cramer Composites, Heek, Germany.

Even, C., Arvieu, C., and Quenisset, J. M. (2008). Powder route processing of carbon fibres reinforced titanium matrix composites. *Composites Science and Technology*, 68:1273–1281.

Farber, L., Levin, I., and Barsoum, M. (1999). transmission electron microscopy study of a low-angle boundary in plastically deformed Ti3SiC2. *Philosophical Magazine Letters*, 79(December):163–170.

Ferrari, B. and Moreno, R. (1996). The conductivity of aqueous Al2O3 slips for electrophoretic deposition. *Materials Letters*, 28(October):353–355.

Fessler, H. and Fricker, D. (1984). Theoretical Analysis of the Ring-on-Ring Loading Disk Test. *Journal of the American Ceramic Society*, 67(9):582–588.

Gauthier, V., Cochepin, B., Dubois, S., and Vrel, D. (2006). Self-Propagating High-Temperature Synthesis of Ti3SiC2: Study of the Reaction Mechanisms by Time-Resolved X-Ray Diffraction and Infrared Thermography. *Journal of the American Ceramic Society*, 89(20975):2899–2907.

German, R. M. (1996). *Sintering Theory and Practice*, volume 1. Wiley.

German, R. M. (2005). *Powder Metallurgy & Particulate Materials Processing*. Metal Powder Industries Federation, New Jersey.

German, R. M. (2013). History of sintering: empirical phase. *Powder Metallurgy*, 56(2):117–123.

Godfrey, D. and John, S. (1986). Disc Flexure Testsfor the Evaluation of Ceramic Strength . In *Ceramic Materials and Components for Engines, Proceedings of the Second International Symposium*, number 1, pages 657–665.

Hamaker, H. C. (1940). Formation of a deposit by electrophoresis. *Trans. Faraday Soc.*, 35(0):279–287.

Hashimoto, H., Zhang, Z., and Sun, Z. (2002). Rapid synthesis of ternary carbide Ti (3) SiC (2) through pulse-discharge sintering technique from Ti/Si/TiC powders. *Metallurgical and Materials Transactions A*, 33(11):3321–3328.

Hyde, A. (1990). Ceramic matrix composites. *Materials & Design*, 11(1):30–36.

Kang, S.-J. L. (2005). Intermediate and Final Stage Sintering. In *Sintering*, chapter 5, pages 57–87. Elsevier.

Khoptiar, Y. and Gotman, I. (2002). Ti2AlC ternary carbide synthesized by thermal explosion. *Materials Letters*.

Kooi, B. J., Poppen, R. J., Carvalho, N. J. M., De Hosson, J. T. M., and Barsoum, M. W. (2003). Ti3SiC2: A damage tolerant ceramic studied with nano-

indentations and transmission electron microscopy. *Acta Materialia*, 51:2859–2872.

Krenkel, W. and Berndt, F. (2005). C/C-SiC composites for space applications and advanced friction systems. *Materials Science and Engineering A*, 412(July):177–181.

Lamouroux, F. and Camus, G. (1994). Oxidation Effects on the Mechanical Properties of 2D Woven C / SiC Composites. *In Situ*, 14:177–188.

Lange, F., Lam, D., Sudre, O., Flinn, B., Folsom, C., Velamakanni, B., Zok, F., and a.G. Evans (1991). Powder processing of ceramic matrix composites. *Materials Science and Engineering: A*, 144:143–152.

Leslie, C. J., Boakye, E. E., Keller, K. a., and Cinibulk, M. K. (2015). Development and characterization of continuous SiC fiber-reinforced HfB2-based UHTC matrix composites using polymer impregnation and slurry infiltration techniques. *International Journal of Applied Ceramic Technology*, 12:235–244.

Li, J.-f. (2003). Fabrication of highly dense Ti 3 SiC 2 ceramics by pressureless sintering of mechanically alloyed elemental powders. *Journal of Material Science*, 8:2661 – 2666.

Lofland, S. E., Hettinger, J. D., Harrell, K., Finkel, P., Gupta, S., Barsoum, M. W., and Hug, G. (2004). Elastic and electronic properties of select M2AX phases. *Appl. Phys. Lett.*, 84(2004):508–510.

Lubrizol Advanced Materials Inc (2015). Lubrizol 2155 Technical Data Sheet. Technical report, Lubrizol Advanced Materials Inc, Cleveland, OH.

Manoun, B., Saxena, S. K., El-Raghy, T., and Barsoum, M. W. (2006). High-pressure x-ray diffraction study of Ta[sub 4]AlC[sub 3]. *Applied Physics Letters*, 88(2006):201902.

Matthewson, M. and Field, J. (1980). An improved strength- measurement technique for britt I e materia Is. *Journal of Physics E: Scientific Instruments*, 13(3):355–359.

McCave, I. N., Bryant, R. J., Cook, H. F., and Coughanowr, C. A. (1986). Evaluation of a Laser-Diffraction-Size Analyzer for Use with Natural Sediments. *Journal of Sedimentary Research*, 56(4):561–564.

MInus, M. L. and Kumar, S. (2005). The processing, properties, and structure of carbon fibers. *JOM Journal of the Minerals, Metals and Materials Society*, 57:52–58.

Morgiel, J., Lis, J., and Pampuch, R. (1996). 8.Microstructure of Ti3SiC2 based ceramics. *Mater. Lett.*, 27(June):85–89.

Morrel, R., McCormick, N., Bevan, J., Lodeiro, M., and Margetson, J. (1999). Biaxial disc flexure - modulus and strength testing. *British Ceramic Transactions*, 98(5):234–240.

Müller, B. E., Dittrich, R., and Moritz, K. (2004). Studies on a Novel Route to C / SiC **. *Refractories*, (7):568–572.

Munro, R. (1997). Material Properties of a Sintered alpha-SiC. *Journal of Physical Chemistry Letters*, 26(5):1195–1203.

Naslain, R. (1992). Two-dimensional SiC/SiC composites processed according to the isobaric-isothermal chemical vapor infiltration gas phase route. *Journal of Alloys and Compounds*, 188:42–48.

Naslain, R. (2004). Design, preparation and properties of non-oxide CMCs for application in engines and nuclear reactors: An overview. *Composites Science and Technology*, 64(March 2003):155–170.

Naslain, R. R. (1998). The design of the fibre-matrix interfacial zone in ceramic matrix composites. *Composites Part A: Applied Science and Manufacturing*, 29:1145–1155.

Newbury, D. E. and Ritchie, N. W. M. (2014). Performing elemental microanalysis with high accuracy and high precision by scanning electron microscopy/silicon drift detector energy-dispersive X-ray spectrometry (SEM/SDD-EDS). *Journal of Materials Science*, 50(2):493–518.

Panigrahi, B., Chu, M.-C., Balakrishnan, a., and Cho, S.-J. (2009). Synthesis and pressureless sintering of Ti3SiC2 powder. *Journal of Materials Research*, 24(November 2008):487–492.

Peng, Z. and Liu, M. (2001). 1 . Preparation of dense platinum-yttria stabilized zirconia and yttria stabilized zirconia films. *Journal of American Ceramic Society*, 84(2):283–288.

Powers, R. (1975). 1 . Electrophoretic Forming of Beta-Alumina Ceramic . *Journal of the Electrochemical Society*, 122(4):490–500.

Pradere, C. and Sauder, C. (2008). Transverse and longitudinal coefficient of thermal expansion of carbon fibers at high temperatures (300-2500 K). *Carbon*, 46(14):1874–1884.

Radovic, M., Barsoum, M., El-Raghy, T., and Wiederhorn, S. (2001). Tensile

creep of fine grained (35 μm) Ti3SiC2 in the 10001200C temperature range. *Acta Materialia*, 49:4103–4112.

Radovic, M., Barsoum, M., El-Raghy, T., and Wiederhorn, S. (2003). Tensile creep of coarse-grained Ti3SiC2 in the 10001200C temperature range. *Journal of Alloys and Compounds*, 361:299–312.

Radovic, M., Barsoum, M. W., El-raghy, T., and Wiederhorn, S. M. (2002). Effect of temperature , strain rate and grain size on the mechanical response of Ti 3 SiC 2 in tension. *Acta Materialia*, 50:1297–1306.

Radovic, M., Barsoum, M. W., Ganguly, a., Zhen, T., Finkel, P., Kalidindi, S. R., and Lara-Curzio, E. (2006). On the elastic properties and mechanical damping of Ti3SiC2, Ti3GeC2, Ti3Si0.5Al0.5C2 and Ti2AlC in the 300-1573 K temperature range. *Acta Materialia*, 54:2757–2767.

Rampai, T., Lang, C. I., and Sigalas, I. (2013). Investigation of MAX phase/c-BN composites. *Ceramics International*, 39:4739–4748.

Rao, S. P., Tripathy, S. S., and Raichur, A. M. (2007). Dispersion studies of submicron zirconia using Dolapix CE 64. *Colloids and Surfaces A: Physicochemical and Engineering Aspects*, 302(March):553–558.

Rasche, S., Strobl, S., Kuna, M., Bermejo, R., and Lube, T. (2014). Determination of Strength and Fracture Toughness of Small Ceramic Discs Using the Small Punch Test and the Ball-on-three-balls Test. *Procedia Materials Science*, 3:961–966.

Sato, K., Mishra, M., Hirano, H., Hu, C., and Sakka, Y. (2014). Pressureless Sintering and Reaction Mechanisms of Ti 3 SiC 2 Ceramics. *Journal of the American Ceramic Society*, 97:1407–1412.

Sato, N., Kawachi, M., Noto, K., Yoshimoto, N., and Yoshizawa, M. (2001). Effect of particle size reduction on crack formation in electrophoretically deposited YBCO films. *Physica C: Superconductivity*, 357-360:1019–1022.

Shetty, D., Rosenfield, A., McGuire, P., Bansal, G., and Duckworth, W. (1980). Biaxial flexure test for ceramics. *Ceramic Bulletin*, 59(12):1193–1197.

Sigma-Aldrich (2015). h-BN Specification Sheet. Technical report, Sigma Aldrich, Darmstadt, Germany.

Sun, Z., Hashimoto, H., Tian, W., and Zou, Y. (2010). Synthesis of the MAX phases by pulse discharge sintering. *International Journal of Applied Ceramic Technology*, 7:704–718.

Sun, Z., Murugaiah, a., Zhen, T., Zhou, a., and Barsoum, M. (2005). Microstructure and mechanical properties of porous TiSiC. *Acta Materialia*, 53:4359–4366.

Sun, Z., Zhang, Z., Hashimoto, H., and Abe, T. (2002). Ternary Compound Ti3SiC2: Part I. Pulse Discharge Sintering Synthesis. *Materials Transactions*, 43(3):428–431.

Tang, K., Wang, C.-a., Huang, Y., Zan, Q., and Xu, X. (2002). A study on the reaction mechanism and growth of Ti 3 SiC 2 synthesized by hot-pressing. *Materials Science and Engineering A*, 328:206–212.

Tang, L., Li, L., Yi, X., and Pan, Z. (1997). Aqueous Powder Slurry Manufacture of Continuous Fiber Reinforced Polyethylene Composite. *Polymer composites*, 18(2):223–231.

Urban, C. and Schurtenberger, P. (1998). Characterization of Turbid Colloidal Suspensions Using Light Scattering Techniques Combined with Cross-Correlation Methods. *Journal of colloid and interface science*, 207(1):150–158.

Vandeperre, L., Van Der Biest, O., and Clegg, W. J. (1997). Silicon carbide laminates with carbon interlayers by electrophoretic deposition. *Key Engineering Materials*, 127-131(1):567–574.

Volkmann, E., Tushtev, K., Koch, D., Wilhelmi, C., Grathwohl, G., and Rezwan, K. (2014). Influence of fiber orientation and matrix processing on the tensile and creep performance of Nextel 610 reinforced polymer derived ceramic matrix composites. *Materials Science and Engineering A*, 614:171–179.

Wan, D. T., Meng, F. L., Zhou, Y. C., Bao, Y. W., and Chen, J. X. (2008). Effect of grain size, notch width, and testing temperature on the fracture toughness of Ti3Si(Al)C2 and Ti3AlC2 using the chevron-notched beam (CNB) method. *Journal of the European Ceramic Society*, 28:663–669.

Wang, P., chu Mei, B., lin Hong, X., and bing Zhou, W. (2007). Synthesis of Ti2AlC by hot pressing and its mechanical and electrical properties. *Transactions of Nonferrous Metals Society of China (English Edition)*.

Wang, Y.-C., Leu, I.-C., and Hon, M.-H. (2004). 1 . Kinetics of electrophoretic deposition for nanocrystalline zinc oxide coatings. *Journal of the American Ceramic Society*, 87(1):84–88.

Zarbov, M., Schuster, I., and Gal-Or, L. (2004). Methodology for selection of charging agents for electrophoretic deposition of ceramic particles. *Journal of Materials Science*, 39:813–817.

Zhang, Z. F., Sun, Z. M., Hashimoto, H., and Abe, T. (2001). A new synthesis reaction of Ti3SiC2 through pulse discharge sintering Ti/SiC/TiC powder. *Scripta Materialia*, 45:1461–1467.

Zhang, Z.-F., Sun, Z.-M., Hashimoto, H., and Abe, T. (2002). A new synthesis reaction of Ti 3 SiC 2 from Ti/TiSi 2 /TiC powder mixtures through pulse discharge sintering (PDS) technique. *Materials Research Innovations*, 5:185–189.

Zhang, Z. F., Sun, Z. M., Hashimoto, H., and Abe, T. (2003). Effects of sintering temperature and Si content on the purity of Ti3SiC2 synthesized from Ti/Si/TiC powders. *Journal of Alloys and Compounds*, 352:283–289.

Zhen, T., Barsoum, M., Kalidindi, S. R., Radovic, M., Sun, Z., and El-Raghy, T. (2005a). Compressive creep of fine and coarse-grained Ti3SiC2 in air in the 1100-1300C temperature range.pdf. *Acta Materialia*, 53:4963–4973.

Zhen, T., Barsoum, M. W., and Kalidindi, S. R. (2005b). Effects of temperature, strain rate and grain size on the compressive properties of Ti3SiC2. *Acta Materialia*, 53:4163–4171.

Zhu, J., Gao, J., Yang, J., Wang, F., and Niihara, K. (2008). Synthesis and microstructure of layered-ternary Ti2AlC ceramic by high energy milling and hot pressing. *Materials Science and Engineering A*.

Zschimmer & Schwarz (2016). Dolapix ce 64. Technical report, Zschimmer & Schwarz, Lahnstein, Germany.

Appendix A Technical Data Sheets for Raw Materials

Please note, material was not completely tested

Aluminium Titanium Carbide Ti_2AlC

1. Product and company identification

Manufacturer/Supplier:
Carbon-Ukraine ltd.
Stepanchenko st., 3, Kiev 03680, Ukraine
E-mail: sales@carbon.org.ua
www.carbon.org.ua
Fax: +380445024149
Tel: +380442332443

Trade name: Ti_2AlC
Aluminium Titanium Carbide

Product type: Ceramic powder

2. Composition/Information on ingredients

Compounds	Content wt%
Ti_2AlC	85-95
TiC	5-10
Al_2O_3	<5

3. Hazard identification

Human Health: Non Known

Environment: Non Bio Degradable

Physical and Chemical: Minimum ignition temperature 250°C in air.
Ignition may occur from flame or sparks.
Fine particles may be ignited by friction or static discharge.
Dust can form explosive mixture with air.
Burning when it catch fire.
Burning ternary carbides reacts explosively with water.
Ternary carbides may form explosive mixtures with oxidizing agents.

4. First aid measures

Skin contact: Wash skin using soap and water.

Eye contact: Wash eye with plenty of water for several minutes, with eyelids held open. If irritation persists seek medical attention.

Inhalation: If any symptom: Move to fresh air. If unconscious keep breathing passage open.

TECHNICAL DATASHEET

Article: **Style 469**
Setting (Thr/cm): **7,0/7,0**
Weave: **Plain**
Finish: **loomstate**

Construction:	Warp	Weft
Yarn material [1] :	Carbon 1K	Carbon 1K
Yarn number [1]:	67 tex	67 tex

Technical Data:		Unit	Target	+/-	Tolerance
Fibre density [1] [3]	Warp	g/cm³	n.G.	+/-	n.G.
	Weft	g/cm³	n.G.	+/-	n.G.
Linear density [1]	Warp	tex	67	+/-	4
	Weft	tex	67	+/-	4
Twist [1]	Warp	T/m		+/-	
	Weft	T/m		+/-	
Setting	Warp	Thr./cm	7,0	+/-	0,3
	Weft	Thr./cm	7,0	+/-	0,3
Weave			Plain		
Weight		g/m2	93	+/-	4
Dry weight		g/m2	93	+/-	4
Moisture content		%	0,5	+/-	max.
Thickness [2]		mm	0,13	+/-	
Width		cm	as ordered	+/-	1

[1] = n.G. = depending on order and yarn specification
[2] = approximate value, not for release
[3] = no measure, certified by supplier

Remarks:

Date	Q.A.	
18.05.94	Monika Kampen	This Datasheet does not include Revision Service.

Specification Sheet

SIGMA-ALDRICH

Product Name	Boron nitride, powder, ~1 µm, 98%
Product Number	255475
Product Brand	ALDRICH
CAS Number	10043-11-5
Molecular Weight	24.82

TEST	SPECIFICATION
APPEARANCE (COLOR)	White to Off White
APPEARANCE (FORM)	Powder
PARTICLE SIZE	CA. 1 MICRON AVERAGE PARTICLE SIZE
ICP ANALYSIS	CONFIRMS BORON COMPONENT
ASSAY (ICP)	42.5% - 44.6% B

Ceramics Keramik Cerámica

DOLAPIX CE 64

Dispersing agent / Deflocculant

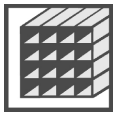

Chemical basis:

Carboxylic acid preparation

Characteristics:

Appearance:	yellowish liquid
Active matter:	approx. 65 %
Solubility:	water-miscible
Density (20 °C):	approx. 1.2 g/cm³
pH (original):	approx. 7
Residue on ignition:	max. 0.1 %

Shelf-life / Packaging:

12 months under proper conditions
drums of 30 and 150 kg, containers of 1100 kg

Application:

DOLAPIX CE 64 is an organic deflocculating agent, that is free from alkali. It does not foam.

DOLAPIX CE 64 makes it possible to produce slips with a high solids content and is, therefore, particularly suitable for deflocculation before spray drying.

Since the product is liquid and is thus completely dissociated, the deflocculation effect commences immediately after addition to the slip. Hence, it is possible to any time to adjust the viscosity of the slip by rapid, homogeneous incorporation into the slip.

DOLAPIX CE 64 can be employed in combination with the conventional temporary binders, such as polyvinyl alcohols, polymer dispersions, polysaccharides, cellulose derivatives and others (OPTAPIX types).

The deflocculation effect of DOLAPIX CE 64 is a result of interaction between the bivalent functional groups of the additive and the surface charge of the ceramic particles. The absorption onto the particles that is associated with this effects a decrease in the slip's viscosity.

The amount that must be added ranges between 0.1 an 0.5 % of the solids content of the slip.

ZSCHIMMER & SCHWARZ
GmbH & Co KG
CHEMISCHE FABRIKEN

Max - Schwarz - Straße 3 - 5
56112 LAHNSTEIN/GERMANY
Tel.: +49 (0) 2621 / 12 485
Fax: +49 (0) 2621 / 12 403
www.zschimmer-schwarz.com

LUBRIZOL® 2155

Succinimide Dispersant

Lubrizol

TECHNICAL DATA SHEET

Performance

Lubrizol 2155 is a succinimide dispersant for use in solventborne and oil-based liquid/paste colorant systems (inks, flushes, color concentrates, etc.). It is particularly effective for dispersing carbon blacks and phthalocyanine blues.

Lubrizol 2155 provides the following benefits:

- Enhances color development or organic colors
- Improves jetness of carbon black
- Decreases grind time

Typical Applications

Lubrizol 2155 is useful for a variety of pigments, especially carbon black.

Lubrizol 2155 is highly effective in:

- Carbon black concentrates
- Color concentrates
- Hydrocarbon resin-based inks
- Phenolic resin-based inks
- Rosin ester-based inks
- Toluene-based inks
- PVC-based screen printing inks

Incorporation

Lubrizol 2155 should be incorporated during the grind stage of manufacturing to maximize adsorption of the dispersant.

Addition Levels

The recommended addition level of Lubrizol 2155 is: weight

- For carbon black dispersions in hydrocarbon media, 0.5-5% by weight to maximize pigment loading
- For coatings and inks, 2-4% based on total formulation weight (added to the grind with the resin or vehicle before pigment addition)
- Plastisols, 0.5-2 phr
- Lubrizol 2155 is not recommended where the mineral oil carrier may adversely affect coating performance.

June 4, 2007

Lubrizol Advanced Materials, Inc.
9911 Brecksville Road
Cleveland, OH 44141-3247
800-380-5397
www.lubrizolcoatings.com

Typical Properties

Appearance	Amber Liquid
Chemical Type	Succinimide
Density (g/cc) @ 15.6°C (60°F)	0.90-0.93
Density (lb/gal) @ 15.6°C (60°F)	7.58-7.83
NVM (% wt)	100
Water (% wt)	0.30 max
Carrier	Mineral Oil
Flash Point °C (°F)	160 (320)
Viscosity* (cP) @ 25°C (77°F)	13,000-23,000

**Measured on a Brookfield RVF Viscometer, #3 spindle, 2 rpm @25°C (77°F).*

Packaging and Storage

Lubrizol 2155 is available in 200-liter (55-gallon) drums and 20 liter (5-gallon) pails. Store in original unopened containers. Shelf life: 2 years. After this, the product should be tested prior to use.

Appendix B Infiltration Yield Measurements

Table 5: Weight measurements for EPD experiments performed with a 7.4 wt% Dolapix addition.

Sample	**Weight before coating [g]**	**Weight after coating [g]**	**Deposition Yield [g]**	**Yield [mg/mmˆ2]**	**EPD Voltage [V]**	**EPD Time [min]**
MAX_EPD1	0.03102	0.03826	0.00724	0.02049	20	5
MAX_EPD2	0.03381	0.04535	0.01154	0.03265	20	10
MAX_EPD3	0.03067	0.04226	0.01159	0.03279	20	20
MAX_EPD4	0.03114	0.04523	0.01409	0.03987	20	30
MAX_EPD5	0.03608	0.04926	0.01318	0.03729	50	5
MAX_EPD6	0.03779	0.05592	0.01813	0.05130	50	10
MAX_EPD7	0.03768	0.06194	0.02426	0.06864	50	20
MAX_EPD8	0.03491	0.06178	0.02687	0.07603	50	30
MAX_EPD9	0.04138	0.05725	0.01587	0.04490	100	5
MAX_EPD10	0.03854	0.05965	0.02111	0.05973	100	10
MAX_EPD11	0.03553	0.06973	0.0342	0.09677	100	20
MAX_EPD12	0.03185	0.06472	0.03287	0.09300	100	30

Table 6: Yield for vacuum infiltration of low solids content Ti_2AlC slurry

	Weight [g]	**Cycle**	**Combined Yield**
2.5 vol %	0.04023	0	0
	0.04701	1	0.00678
	0.05962	2	0.01939
	0.0657	3	0.02547
	0.0694	4	0.02917
5 vol %	0.03682	0	0
	0.05424	1	0.01742
	0.0669	2	0.03008
	0.0837	3	0.04688
	0.0937	4	0.05688

Table 7: Measured weights for individual laminates, without the prior infiltration of a h-BN powder interphase, infiltrated using pressure infiltration.

Sample	**Weight (1 cycle) [g]**	**Weight (2 cycles) [g]**
1	0.09402	0.12512
2	0.09613	0.1105
3	0.08764	0.11611
4	0.097	0.10774
5	0.0944	0.11917
6	0.09564	0.16964
7	0.09866	0.12877
8	0.09822	0.12456
9	0.09175	0.1325
10	0.0978	0.13405
11	0.09948	0.14431
12	0.0936	0.12892
13	0.0936	0.10388
14	0.11776	0.10489
15	0.1038	0.13916
16	0.10928	0.11629
17	0.12319	0.1127
18	0.10458	0.11305
19	0.11843	0.13028
20	0.12982	0.13152
21	0.11502	0.14458
22	0.10547	0.11959
23	0.10991	0.15528
24	0.10716	0.13647
25	0.0939	0.11352
Average	0.1030504	0.126504
Standard deviation	0.010651086	0.015725604

Table 8: Measured weights for individual laminates, with the prior infiltration of a h-BN powder interphase, infiltrated using pressure infiltration.

Sample	**Weight (1 cycle) [g]**	**Weight (2 cycles) [g]**
1	0.09479	0.09193
2	0.10105	0.11415
3	0.08537	0.10815
4	0.09637	0.10628
5	0.09445	0.08709
6	0.0873	0.10299
7	0.09333	0.09678
8	0.09712	0.10712
9	0.10393	0.11585
10	0.10762	0.11189
11	0.09795	0.10156
12	0.1038	0.10044
13	0.0945	0.09168
14	0.0925	0.10363
Average	0.096434286	0.102824286
Standard deviation	0.005982042	0.008340213

Appendix C Volume Fraction Calculations for Prepreg and Sintered CMC

This appendix presents the volume fraction calculations for the prepreg and sintered CMC. Table 9 and Table 10 show the weight and dimensional measurements for the prepreg samples and the sintered samples, respectively. Each of the samples reported on consists of 8 laminate layers infiltrated using pressure infiltration.

The volume fractions, fibre ν_f, matrix ν_m, and pore ν_p, were calculated as follows:

$$\nu_f = V_f/V_T \tag{15}$$

,

$$\nu_m = V_m/V_T \tag{16}$$

, and

$$\nu_p = (V_T - V_m - V_f)/V_T \tag{17}$$

where V_T is the total volume of the specimen, V_m is the volume of the matrix, and V_f is the volume of the fibre reinforcement. The volumes of the fibres and the matrix are calculated as

$$V_f = m_f/\rho_f \tag{18}$$

and

$$V_m = m_f/\rho_m \tag{19}$$

where m_f is the mass of the fibres, ρ_f is the density of the fibres, m_m is the mass of the matrix material, and ρ_m is the theoretical density of the matrix material.

Table 9: Weight and dimensional measurements for prepreg samples consisting of 8 layers.

Sample	**Weight of fibres [g]**	**Thickness of fibres [mm]**	**Weight after infiltration [g]**	**Thickness of layers [mm]**
A1	0.496	0.96	1.02434	1.05
A2	0.496	0.96	1.22331	1.09
A3	0.496	0.96	1.0051	1.04
A4	0.496	0.96	1.03035	1.04
A5	0.496	0.96	0.99959	1.03
Average	0.496	0.96	1.056538	1.05
Standard deviation	-	-	0.084172	0.020976

Table 10: Weight and dimensional measurements for sintered samples consisting of 8 layers.

Sample	**Weight of fibres [g]**	**Thickness of fibres [mm]**	**Weight after infiltration [g]**	**Thickness of layers [mm]**
A1	0.496	0.96	1.02059	0.834
A2	0.496	0.96	1.23857	0.906
A3	0.496	0.96	1.00187	0.796
A4	0.496	0.96	1.04215	0.84
A5	0.496	0.96	0.99638	0.818
Average	0.496	0.96	1.059912	0.8388
Standard deviation	-	-	0.09075856	0.0368912

Table 11: Volume fraction results for unsintered CMC prepreg samples.

Sample	**Fibre volume fraction**	**Matrix volume fraction**	**Pore volume fraction**
1	0.381875625	0.173200834	0.444923541
2	0.36786184	0.229677709	0.40246045
3	0.385547506	0.168498308	0.445954186
4	0.385547506	0.176855374	0.43759712
5	0.389290685	0.168292848	0.442416467
Average	0.382024632	0.183305015	0.434670353
Standard deviation	0.00745954	0.023403943	0.016361533

Table 12: Volume fraction results for sintered CMC samples.

Sample	**Fibre volume fraction**	**Matrix volume fraction**	**Pore volume fraction**
1	0.484655911	0.218058605	0.297285484
2	0.44614021	0.276323072	0.277536718
3	0.507792751	0.220148544	0.272058705
4	0.481194083	0.218963797	0.29984212
5	0.494135734	0.211909087	0.293955179
Average	0.482783738	0.229080621	0.288135641
Standard deviation	0.020509016	0.023792132	0.011184215

Appendix D Density Measurements for Sintered CMC and Pure Ti_2AlC

Table 13: Archimedes measurements for sintered CMC.

Sample	**Dry mass [g]**	**Wet mass [g]**	**Suspended mass [g]**	**Density [g/cm^3]**	**% Open porosity**
1	1.0202	1.09615	0.59545	2.0354	15.16876373
2	1.2382	1.34775	0.74605	2.055667	18.20674755
3	1.0001	1.0715	0.5866	2.060313	14.7246855
4	1.0418	1.133	0.6226	2.038993	17.86833856
5	0.9946	1.07185	0.5781	2.012257	15.64556962
Average	1.05898	1.14405	0.62576	2.040526	16.32282099
Standard deviation	0.091138	0.104294	0.061973135	0.017021	1.434040337

Table 14: Archimedes measurements for sintered pure sintered Ti_2AlC.

Sample	**Dry mass [g]**	**Wet mass [g]**	**Suspended mass [g]**	**Density [g/cm^3]**	**% Open porosity**
1	2.8189	2.83385	2.102233333	3.848912973	2.043419824
2	2.8981	2.8984	2.1885	4.078103117	0.042259473
3	2.8713	2.876925	2.1557	3.976947069	0.779923048
4	2.859	2.868075	2.1442	3.945414076	1.253669487
5	2.8623	2.868175	2.1485	3.973019955	0.816340709
Average	2.86192	2.869085	2.147826667	3.964479438	0.987122508
Standard deviation	0.02552	0.020804751	0.02759952	0.073290952	0.655999315

Appendix E Densification Parameter

The densification parameter is calculated as:

$$\psi = \frac{\rho_s - \rho_g}{\rho_t - \rho_g} \tag{20}$$

where ρ_s is the sintered density, ρ_g is the green density, and ρ_t is the theoretical density. The sintered density, ρ_s, as measured using the Archimedes method is 2.04. The green density, ρ_g, is calculated as:

$$\rho_g = \nu_f \times \rho_f + \nu_m \times \rho_m \tag{21}$$

where ν_f is the fibre volume fraction, ρ_f is the density of the fibres, ν_m is the matrix volume fraction, and ρ_m is the density of the matrix. The theoretical density, ρ_t, is calculated as:

$$\rho_t = \nu_{f,t} \times \rho_f + \nu_{m,t} \times \rho_m \tag{22}$$

where $\nu_{f,t}$ is the theoretical fibre volume fraction and $\nu_{m,t}$ is the theoretical matrix volume fraction. The theoretical volume fractions are calculated using the measured mass of the constituents and assuming that there is zero porosity present.